5-2010

COUPLED DEM-FEM FOR DYNAMIC ANALYSIS OF GRANULAR SYSTEMS IN BENDING

Kitti Rattanadit
University of Nebraska - Lincoln, kitti_crma39@hotmail.com

COUPLED DEM-FEM FOR DYNAMIC ANALYSIS OF GRANULAR SYSTEMS IN BENDING

by

Kitti Rattanadit

A DISSERTATION

Presented to the Faculty of

The Graduate College at the University of Nebraska

In Partial Fulfillment of Requirements

For the Degree of Doctor of Philosophy

Major: Engineering
(Engineering Mechanics)

Under the Supervision of Professor Florin Bobaru

Lincoln, Nebraska

May, 2010

COUPLED DEM-FEM FOR DYNAMIC ANALYSIS OF GRANULAR SYSTEMS IN BENDING

Kitti Rattanadit, Ph.D.

University of Nebraska, 2010

Advisor: Florin Bobaru

Characterizing the dynamic behavior of granular materials is one of the great challenges in the mechanics of granular matter. Methods for evaluating the mechanical properties of granular matter have applications in a variety of industries, mining and geotechnical activities, defense and military operations. A coupled 2D Discrete Element Method-Finite Element Method (DEM-FEM) code, called "BobKit", is developed and implemented for analyzing the behavior of a 2D granular layer on top of an elastic beam under deforming (quasi-static) or vibrating (dynamic) of the beam. The explicit time-integration dynamic code is used to simulate quasi-static and dynamic bending of the granular layer for close-packed monodispersed and random-packed polydispersed particles. In the DEM model of the granular particles we use and compare the results between two different contact force models: the linear spring-dashpot (Hookean contact) model, and the nonlinear spring-dashpot (Hertzian contact) model. In addition, the effect of the presence or absence of rolling resistance, due to rolling friction, is analyzed. Based on the contact force models used in the analyses, we propose a new way of computing the dissipative parameter in the Hertz model: we calibrate this parameter via a simple test of a dropped particle onto a rigid floor.

In quasi-static analysis, the structural changes of the force chains and the resonant behavior of granular layers in a 2D container with an elastic bottom are studied. The changes taking place in the structure of the force chains observed for both contact force models are qualitatively similar. The force chains generated during bending deformation form regions that can lead to enhance convection cells for more effective mixing and segregation in combined shaking/bending-vibrated granular media. We perform validation of the BobKit code by comparing the particle-size dependence of the bending stiffness of the granular-elastic beam system with analytical values from a quasi-static well-bonded model. In particular, when rolling resistance is included in the simulation, the results match very well the analytical model for the particle-size dependence for both contact force models. A dynamic analysis investigating the behavior of the granular layer/elastic beam system under resonant bending vibrations is also performed. Most computational studies of granular materials have been performed in rigid containers. The work in this dissertation is the first to investigate the evolution of the structural changes of the force chains under quasi-static bending deformation of a granular layer and dynamic-resonance of granular layers in a container with an elastic bottom. The code developed as part of this effort can be setup for varieties of particle simulations and easily extended to 3D analysis.

Acknowledgements

I would like to thank the Royal Thai Army for giving me a scholarship to proceed my doctoral degree at USA. I wish to thank my advisor, who has been helping me throughout my academic years, Professor Florin Bobaru. He always give me valuable guidance and constant support for many years at the University of Nebraska-Lincoln (UNL). Since I have been Dr. Bobaru's student at the UNL, I have a better perspective not to "give up" doing my research. Other than that he always concerns for my family. I admire the way he treats his students since we first met at his office in the Department of Engineering Mechanics. Also, I am grateful to my committee members, Dr. Joseph A. Turner, Dr. Mehrdad Negahban and Dr. Steve Cohn, for careful evaluation and valuable suggestion on my dissertation. Without them, I could not have completed this dissertation. Last but not least, I would like to thank all my friends and others who help me success in my academic career.

Most importantly, I would like to thank my lovely family, particularly my wife Supaporn Rattanadit, for taking care and always supporting me with endless love. I would like to dedicate my work to my family, father and mother.

Table of Contents

List of Figures

List of Tables

Chapter 1

Introduction

1.1 Background and Motivation

Methods for evaluating the mechanical properties of granular matter have applications in a variety of industries like food and agricultural products processing, pharmaceutical industries, mining and geotechnical activities, defense and military operations, etc. Hence, understanding the static and dynamic behavior of granular matter is a topic that interested researchers for decades. An "effective medium theory" (EMT), based on Hertz-Mindlin contact force, is available for predicting the elastic behavior of the granular materials under static pressure, but this has not been successful (see Makse et al. [67]). The EMT (see e.g., Digby [22] and Walton [102]) predicts that the bulk modulus K and shear modulus μ of a granular assembly of elastic spheres increase with pressure p where both moduli vary as $p^{1/3}$ and the ratio of K/μ is constant. However, from the experiments (see e.g., Domenico [23], Makse

et al. [67]), the bulk and shear moduli increase more rapidly than $p^{1/3}$, and the ratio of K/μ is significantly larger than the EMT prediction. The discrepancy of the EMT and the experimental results was explained by Makse et al. [67].

Another discrepancy of the EMT and the dynamic experimental results was also reported by Kang [46] and Kang et al. [47] in studying acoustic land mine detection. Acoustic methods for land mine detection have been recently studied because of their advantages compared to other methods in reducing the rate of false positives (see e.g., Donskoy [24], Donskoy et al. [25], [26], Lee et al. [61], Sabatier et al. [88], Scott et al. [92], Xiang et al. [103], Zagrai et al. [108]). In this method, sound waves excite resonant modes in the top plate of the mine which induces vibrations of the sand on top of the mine that differ from vibrations of sand around the mine. The sand response can then be processed and detection can take place. The interaction between the sand particles and the vibrating plate is expected to influence the resonant frequency of the plate. In Kang [46] and Kang et al. [47], a plate-granular layer (PGL) system is used to study the effects of the particle size on the resonance of the PGL system. The experimental results reveal $\sigma \sim R^{1/3}$ with R and σ being the particle radii and slope of the resonance-mass ratio curve whereas the dependence of $\sigma \sim R^{1/6}$ is obtained from the EMT prediction by Digby [22]. The discrepancy between the analytical and the observed values has never been explained. Also, it should be addressed that the continuum-based model in Kang et al. [47] where the thick plate is used for the

granular layer is not predictive since it uses the experimental frequencies for obtaining the "equivalent" Young's modulus of the granular layer. As a result, a computational approach called "particle-based method" (PBM) like the discrete element method (DEM) has been developed and used to predict the behavior of the granular materials under static and dynamic loads.

1.2 Objectives

In order to analyze the behavior of granular materials in the dynamic regime and explain the discrepancy between the analytical models and experiments mentioned in the previous section, a coupled 2D Discrete Element Method-Finite Element Method (DEM-FEM) code, called "BobKit", is developed and implemented for studying the quasi-static and dynamic behavior of granular materials on a deforming and vibrating elastic support. Results from two different contact force models: the linear spring-dashpot or Hookean contact model, which is used in the original discrete element formulation on Cundall and Strack [19], and the newer nonlinear spring-dashpot or Hertzian contact model on Gerl and Zippelius [32] are compared. In addition, the effect of the presence or absence of rolling resistance, due to rolling friction, is investigated as well as the effect of particle packing: monodispersed versus polydispersed systems. Due to difficulty in evaluating the damping parameter for the nonlinear

model, which - at least in principle - could be obtained from carefully conducted experiments, a new approach, that calibrates it with the restitution coefficient in a dropped-particle test, is proposed here for evaluating this parameter. A new derivation of the analytical particle-size dependence of the bending stiffness is obtained for a 2D granular aggregate.

The objective to have a predictive computational model is achieved since the coupled DEM-FEM simulation of the quasi-static bending deformation of a granular material recovers the analytical solution for the particle-size dependence. The BobKit code is also used to analyze the evolution of the force chains taking place under bending deformation of the granular layer on an elastic beam. The results here show potential for enhancing mixing and/or segregation if one is to combine a rigid-body shaking of the container containing the granular material with bending vibrations of the bottom of the container. The last objective is to use the coupled DEM-FEM code to discover the source of the large discrepancy between the analytical values obtained for well-bonded hypothesis of the particle-size dependence on the resonance of the granular layer and the experimental results shown in Kang [46] and Kang et al. [47].

1.3 Organization of Dissertation

In the introductory chapter 1, the background material and brief literature review of contact force models used in particle simulations and of the coupled DEM-FEM simulations are provided. An existing nonlinear contact force based on Hertzian theory for an elastic disk is reviewed in detail in chapter 2. In chapter 3, the linear and nonlinear spring-dashpot contact models are reviewed and a new and simple way of calibrating the damping parameter for the nonlinear model is given. An efficient particle-pair in contact algorithm which is used to determine contacts is provided as well. The equations of motion for the DEM and the FEM are also described in this chapter. Rolling resistance is considered as well. In chapter 4, the elastic moduli of granular assembly of 2D particles (disks) under hydrostatic pressure are derived and the extension for the methods for obtaining the particle-size dependence from the disks is given. In chapter 5, the structural changes in the force chains and the resonant behavior of a composite beam equivalent to the 2D granular-layer/elastic-beam (GLEB) system under bending deformations are studied as a quasi-static analysis. Validation of the BobKit code is achieved by comparing the analytical model for disks in chapter 4 with the computational quasi-static analysis. The dynamic resonant behavior of the GLEB system is studied in chapter 6. In this chapter, the influence of parameters such as the particle's Young's modulus, the

friction coefficients, rolling resistance on the resonant behavior is investigated. In addition, the differences between the contact force models (linear/nonlinear) in the resonance are explored as well. Comparisons with the experimental results for the 3D plate-granular layer (PGL) system conducted by Kang [46] and Kang et al. [47] are discussed in chapter 5 and 6.

1.4 Literature Review

The discrete element method (DEM) has become a very popular tool for studying the micro-macro mechanical behavior of granular materials since first proposed by Cundall and Strack in 1979 [19]. Applications of the DEM for modelling granular flow, and mixing and segregation, are now covering diverse fields such as powder technology, pharmaceutical industries, food industry and agriculture, geotechnical processes and civil engineering, mining, etc (see e.g., Antony [3], Campbell [13], [14], Cleary [17], Kudrolli [54], Lewis et al. [62], Onate and Rojek [78], Sebastian and Luis [93], Tijskens et al. [100], Yamane [105]). The DEM is known as a "soft particle" method because the contacting particles are allowed to slightly deform (virtual overlap). The contacting point between particles is taken approximately at the center of the overlap region. In the DEM, the motion of an individual particle in the system is computed as follows: the particles' positions determine the overlap, which results in

interaction forces (repulsive and/or attracting based on a particular mechanical model of interaction) that are integrated using the linear and angular momentum balance equations to compute the velocities of the particles. The new particles' positions are then updated using a particular integration scheme.

Early versions of the DEM used simplified contact models, such as linear spring-dashpot (Cundall and Strack [19]). More recently, other contact force models based on contact mechanics equations developed by, for example, Hertz [39] for normal forces and Mindlin and Deresiewicz [72] (where the compliance of elastic bodies in contact was first derived by Mindlin [71]) for tangential forces, have been used (see also Johnson [45]). The choice for the contact force model depends very much on the particle geometries, material properties, and the granular flow characteristics. Among the simplified models, the contact force represented by the linear spring-dashpot model is widely used (for some recent applications with this model see e.g., Cleary and Sawley [18], Haff and Werner [35], Kuo et al. [55], Schäfer et al. [89], Taguchi [95], Thompson and Grest [96], Zhang and Whiten [109]). Advantages of this model are that it can be easily developed and applied for various particle geometries such as spheres, disks, ellipsoids, and the contact parameters (i.e., stiffness and damping coefficients) can be computed from the constant normal restitution coefficient and collision time (time in contact) (see e.g., Kruggel et al. [52], Quiniou and Rioual [82], Schäfer et al. [89]). However, Renzo and Maio [87] pointed out that the normal and

tangential spring constants (K_n, K_t) for the linear spring-dashpot model are related to the material parameters to give reasonable results in simulations of granular flow. In addition, the normal restitution coefficient observed from the experiments reveals that it strongly depends on the impact velocity (see e.g., Kuwabara and Kono [56], Labous et al. [58], Sondergaard et al. [94]). These issues led to efforts to develop more sophisticated and accurate nonlinear contact models (see e.g., Gerl and Zippelius [32], Mishra [73], Ramírez [83], Schwager [90], Thornton and Randall [98]).

Among the nonlinear contact force models, Hertz theory [39] is extensively used to compute normal forces while the Mindlin-Deresiewicz theory [72] is used for tangential forces. Based on Hertzian-type contact, the contact forces are derived based on the material parameters such as density, Young's modulus, Poisson's ratio, etc. Many DEM simulations have been done for 3D particles (see e.g., Renzo and Maio [87], Thornton and Randall [98]), Thornton and Yin [99], Yang et al. [107], Zhou et al. [110]). The extension of Hertzian contact for 2D particles is given in e.g., Gerl and Zippelius [32], Johnson [45], Poritsky [80]. The nonlinear contact models have been used in, for example, modelling granular flow in a hopper (see e.g., Langston et al. [60], Langston and Tuzun [59]), heap formation (see Baxter et al. [6]), shot peening processes (see Han et al. [36], [37]), contact of a granular particle system to quantify inter-particle forces, velocity, and contact stresses (see Thornton and Randall [98]), impact of spherical particles with and without adhesion (see Thornton and

Yin [99]). Reviews and comparisons between using a contact-based model and a simplified model in modelling the mechanics of granular matter are reported in e.g., Bell et al. [8], Ji and Shen [44], Kruggel et al. [52], Mishra [73], Renzo and Maio [87], Schäfer et al. [89].

The combined Discrete Element Method-Finite Element Method (DEM-FEM) was first proposed for the study of the shot peening process by Petrinic in 1996 [79] in his doctorate work. Han et al. [36] give results for a 2D simulations of shot peening and they explain in detail the treatment of possible contacts between a disk and the line segments of the finite elements. The shot is modelled by a discrete element while the impacted surface is modelled with finite elements. A review and equivalencies between various contact force models for small deformations is included. An extension of the model to 3D for shoot-peening applications appeared in Han et al. [37]. The combined DEM-FEM in 2D dynamic analysis of geomechanical problems is studied in Onate and Rojek [78]. This study involves fracture in cohesive granular material and plastic flow and wear in a cutting tool. Several examples are shown simulating rock cutting and tool wear, strip punch test and soil, and pipe interaction leading to pipe ovalization. The cutting tool is modelled by finite elements first, to simulate the plastic deformation, and then by discrete elements to model the wearing process. The soil or rock samples are modelled using discrete elements. Other versions of coupling

between FEM and DEM are used in applications for reduced models of concrete structures in impact problems (see Frangin et al. [30]), introducing deformability in DEM particles for impact problems (Komodromos and Williams [50], Komodromos [49]) and flow and compaction of irregular, randomly packed, particles to form a tabletted product (see Gethin et al. [33])

Chapter 2

Hertzian Contact of an Elastic Disk

2.1 Introduction

In this chapter, the stresses and deformations of an elastic disk in contact based on Hertz theory are reviewed. The context "disk" means the disk of finite thickness. The contact of the disk is then considered as the "line loading" where the loaded strip is in the direction of the disk axis. For the derivation of stresses and deformations of an elastic disk, small deformation is assumed so that linear elasticity of the plane problem is applicable. The stresses due to Hertzian contact are highly concentrated close to the contact region and decrease rapidly with distance from the point of contact. In this chapter, the linear elasticity of plane stress problems in absence of body forces is first summarized. Then, the stresses due to concentrated and distributed normal loads on an elastic half-space are reviewed. Finally, the stresses and deformations of an elastic disk on a rigid supporting plane are provided.

2.2 Linear Elasticity of Plane Stress Problems

In this section, the equations for plane stress problems of an elastically isotropic material in absence of body forces in rectangular and polar coordinate systems are summarized. In rectangular coordinates (x, y), the equilibrium equations for plane stress throughout an elastic solid with no body forces are (see e.g., Johnson [45], Malvern [68])

$$\frac{\partial \sigma_{xx}}{\partial x} + \frac{\partial \sigma_{xy}}{\partial y} = 0, \qquad \frac{\partial \sigma_{xy}}{\partial x} + \frac{\partial \sigma_{yy}}{\partial y} = 0, \tag{2.1}$$

where σ_{xx}, σ_{yy} and σ_{xy} are the stress components on the plane. The corresponding strains $\epsilon_{xx}, \epsilon_{yy}$ and ϵ_{xy} relate to the small displacements u_x and u_y by

$$\epsilon_{xx} = \frac{\partial u_x}{\partial x}, \qquad \epsilon_{yy} = \frac{\partial u_y}{\partial y}, \qquad \epsilon_{xy} = \frac{1}{2}\left(\frac{\partial u_y}{\partial x} + \frac{\partial u_x}{\partial y}\right). \tag{2.2}$$

The compatibility equation satisfying all strain components yields

$$\frac{\partial^2 \epsilon_{xx}}{\partial y^2} + \frac{\partial^2 \epsilon_{yy}}{\partial x^2} = 2\frac{\partial^2 \epsilon_{xy}}{\partial x \partial y}. \tag{2.3}$$

For an isotropic material, the Hooke's law that relates the stresses and strains for plane stress reduces to

$$\epsilon_{xx} = \frac{1}{E}\left(\sigma_{xx} - \nu\sigma_{yy}\right), \quad \epsilon_{yy} = \frac{1}{E}\left(\sigma_{yy} - \nu\sigma_{xx}\right), \quad \epsilon_{xy} = \frac{1}{2G}\sigma_{xy} = \frac{(1+\nu)}{E}\sigma_{xy}, \tag{2.4}$$

where G is the shear modulus (modulus of rigidity), E is the Young's modulus, ν is the Poisson's ratio. The form of Hooke's law for plane strain is similar to that for plane

stress, and is given by replacing $E \longrightarrow E/(1-\nu^2)$ and $\nu \longrightarrow \nu/(1-\nu)$. The plane stress problem describes the situation for thin plates where the only applied loads are in-plane loads. The equilibrium equations (Eqs. (2.1)) are identically satisfied if the stresses are related to a scalar function $\phi(x, y)$ by (see e.g., Johnson [45], Malvern [68])

$$\sigma_{xx} = \frac{\partial^2 \phi}{\partial y^2}, \qquad \sigma_{yy} = \frac{\partial^2 \phi}{\partial x^2}, \qquad \sigma_{xy} = -\frac{\partial^2 \phi}{\partial x \partial y}, \tag{2.5}$$

where $\phi = \phi(x, y)$ is the unknown function, called Airy's stress function, to be determined from the boundary condition. The compatibility equation in terms of stresses satisfying the equations of equilibrium (Eqs. (2.1)), compatibility for strain (Eq. (2.3)) and Hooke's law (Eqs. (2.4)) becomes

$$\nabla^2 (\sigma_{xx} + \sigma_{yy}) = 0, \qquad \nabla^2 = \frac{\partial^2}{\partial x^2} + \frac{\partial^2}{\partial y^2}, \tag{2.6}$$

where ∇^2 is the Laplacian operator. Note that this compatibility equation is obtained by substituting equations of Hooke's law (Eqs. (2.4)) and equilibrium (Eqs. (2.1)), by eliminating the shear stress σ_{xy}, into the equation of strain compatibility (Eq. (2.3)).

In some circumstances, it is convenient to use the polar coordinates (r, θ) to solve for two-dimensional (2D) problems. The equations of equilibrium for plane stress in polar coordinates in absence of body forces are (see e.g., Johnson [45], Malvern [68])

$$\frac{\partial \sigma_{rr}}{\partial r} + \frac{1}{r}\frac{\partial \sigma_{r\theta}}{\partial \theta} + \frac{1}{r}(\sigma_{rr} - \sigma_{\theta\theta}) = 0, \qquad \frac{\partial \sigma_{r\theta}}{\partial r} + \frac{1}{r}\frac{\partial \sigma_{\theta\theta}}{\partial \theta} + \frac{2}{r}\sigma_{r\theta} = 0, \tag{2.7}$$

where $\sigma_{rr}, \sigma_{\theta\theta}$ are the radial and circumferential stresses, $\sigma_{r\theta}$ is the shear stress in the polar coordinates. The corresponding strains $\epsilon_{rr}, \epsilon_{\theta\theta}$ and $\epsilon_{r\theta}$ relate to the small

displacement in radial u_r and circumferential u_θ components as

$$\epsilon_{rr} = \frac{\partial u_r}{\partial r}, \qquad \epsilon_{\theta\theta} = \frac{u_r}{r} + \frac{1}{r}\frac{\partial u_\theta}{\partial \theta}, \qquad \epsilon_{r\theta} = \frac{1}{2}\left(\frac{1}{r}\frac{\partial u_r}{\partial \theta} + \frac{\partial u_\theta}{\partial r} - \frac{u_\theta}{r}\right). \tag{2.8}$$

For plane stress, the stress-strain relationships for an isotropic Hooke's law yield

$$\epsilon_{rr} = \frac{1}{E}\left(\sigma_{rr} - \nu\sigma_{\theta\theta}\right), \quad \epsilon_{\theta\theta} = \frac{1}{E}\left(\sigma_{\theta\theta} - \nu\sigma_{rr}\right), \quad \epsilon_{r\theta} = \frac{1}{2G}\sigma_{r\theta} = \frac{(1+\nu)}{E}\sigma_{r\theta}. \tag{2.9}$$

Note that the equations for isotropic Hooke's law in rectangular and polar coordinate systems remain the same with x and y replaced by r and θ. With no body force, the stresses are defined in term of the scalar stress function $\phi = \phi(r, \theta)$ as (see e.g., Johnson [45], Malvern [68])

$$\sigma_{rr} = \frac{1}{r}\frac{\partial \phi}{\partial r} + \frac{1}{r^2}\frac{\partial^2 \phi}{\partial \theta^2}, \qquad \sigma_{\theta\theta} = \frac{\partial^2 \phi}{\partial r^2}, \qquad \sigma_{r\theta} = -\frac{\partial \phi}{\partial r}\left(\frac{1}{r}\frac{\partial \phi}{\partial \theta}\right). \tag{2.10}$$

Then, the corresponding compatibility equation for stresses becomes

$$\nabla^2\left(\sigma_{rr} + \sigma_{\theta\theta}\right) = 0, \qquad \nabla^2 = \frac{\partial^2}{\partial r^2} + \frac{1}{r}\frac{\partial}{\partial r} + \frac{1}{r^2}\frac{\partial^2}{\partial \theta^2}. \tag{2.11}$$

2.3 Stresses due to Normal Loads on an Elastic Half-Space

In this section, the stresses due to a concentrated normal and distributed normal loads acting on an elastic half-space are reviewed. The stresses due to a concentrated

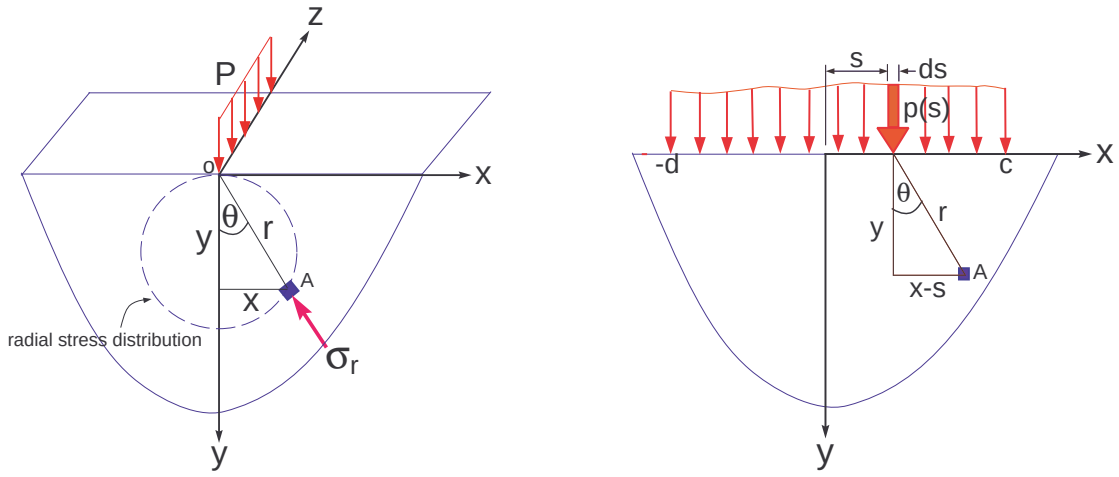

(a) (b)

Figure 2.1: (a) Stresses at point A on an elastic half-space (semi-infinite plane surface) produced by a concentrated normal load P per unit length distributed along the z-axis (or line load). (b) Stresses (not shown) at point A on an elastic half-space produced by a distributed normal load $p(s)$ per unit length along the z-axis (not shown) over the load region $-d \leq x \leq c$.

normal load P per unit length distributed along the z-axis on an elastic half-space (see Fig. 2.1a) was first solved by Flamant in 1892. An elastic half-space is a semi-infinite elastic solid bounded by a plane surface. The solution to this problem in polar coordinates (r, θ) takes the form (see e.g., Johnson [45], Malvern [68])

$$\phi(r, \theta) = Cr\theta \sin\theta, \tag{2.12}$$

where C is an arbitrary constant. Substituting Eq. (2.12) into Eqs. (2.10) yields

$$\sigma_{rr} = \frac{2C}{r} \cos\theta, \qquad \sigma_{\theta\theta} = \sigma_{r\theta} = 0. \tag{2.13}$$

The constant C is determined from the boundary condition at point O (see Fig. 2.1a)

$$-P = \int_{-\pi/2}^{\pi/2} \sigma_{rr} \cos\theta r d\theta = 4C \int_{0}^{\pi/2} \cos^2\theta d\theta = C\pi, \tag{2.14}$$

so that $C = -P/\pi$ with P being the normal point force distributed along the z-axis. Hence, the stresses in Eqs. (2.13) at a point on the elastic half-space (i.e., at point A) due to the normal point load P become

$$\sigma_{rr}(r,\theta) = -\frac{2P}{\pi}\frac{\cos\theta}{r}, \qquad \sigma_{\theta\theta}(r,\theta) = \sigma_{r\theta}(r,\theta) = 0. \tag{2.15}$$

Also, the corresponding scalar stress function (Eq. (2.12)) reads

$$\phi(r,\theta) = -\frac{P}{\pi} r\theta \sin\theta. \tag{2.16}$$

In Eqs. (2.15), the radial stress σ_{rr} increases with decreasing in r. Theoretically, the radial stress due to the normal point load is infinite ($\sigma_{rr} \to \infty$) at the point of application ($r \to 0$). Transformation of the stresses from polar coordinates to rectangular coordinates can be accomplished by using the relation

$$\sigma_{ij} = a_i^m a_j^n \sigma_{mn}, \tag{2.17}$$

where $a_i^m = cos(x_i, x_m)$ represents the direction cosine, the indices are defined as follows: $i, j = 1, 2$ (1 for x and 2 for y), and $m, n = 1', 2'$ ($1'$ for r and $2'$ for θ), respectively. By applying Eqs. (2.15) to Eq. (2.17), the stresses due to the normal point load P per unit length acting on elastic half-space in rectangular coordinates

(see Fig. 2.1a) yield (see e.g., Gerl and Zippelius [32], Johnson [45])

$$\begin{aligned}
\sigma_{xx}(x,y) &= \sigma_{rr}(r,\theta)\sin^2\theta = -\frac{2P}{\pi}\frac{x^2 y}{\left(x^2+y^2\right)^2},\\
\sigma_{yy}(x,y) &= \sigma_{rr}(r,\theta)\cos^2\theta = -\frac{2P}{\pi}\frac{y^3}{\left(x^2+y^2\right)^2},\\
\sigma_{xy}(x,y) &= \sigma_{rr}(r,\theta)\sin\theta\cos\theta = -\frac{2P}{\pi}\frac{xy^2}{\left(x^2+y^2\right)^2}.
\end{aligned} \tag{2.18}$$

The stresses due to the normal distributed load can then be obtained by superimposing the stresses produced by the concentrated normal force P over region $-d \le x \le c$. Here, the concentrated normal force P is replaced by $p(s)ds$, where $p(s)$ is the normal traction acting on an elemental area of width ds, and x replaced by $(x-s)$ as shown in Fig. 2.1b. Hence, the stresses due to the distributed normal load per unit length along z-axis on the elastic half-space become

$$\begin{aligned}
\sigma_{xx}(x,y) &= -\frac{2y}{\pi}\int_{-d}^{c}\frac{p(s)(x-s)^2}{\left[(x-s)^2+y^2\right]^2}ds,\\
\sigma_{yy}(x,y) &= -\frac{2y^3}{\pi}\int_{-d}^{c}\frac{p(s)}{\left[(x-s)^2+y^2\right]^2}ds,\\
\sigma_{xy}(x,y) &= -\frac{2y^2}{\pi}\int_{-d}^{c}\frac{p(s)(x-s)}{\left[(x-s)^2+y^2\right]^2}ds.
\end{aligned} \tag{2.19}$$

Here, if the pressure distribution $p(s)$ is known then the stresses can be evaluated. Note that the stresses can also be determined from the scalar stress function obtained from the Flamant solution (see Eq. (2.16)). In Fig. 2.1b, for small scalar function, we have

$$d\phi = -\frac{1}{\pi}p(s)(x-s)\arctan\left(\frac{x-s}{y}\right)ds, \tag{2.20}$$

with $P = p(s)d(s)$, $\theta = \arctan((x-s)/y)$ and $\sin\theta = (x-s)/r$, so that

$$\phi(x,y) = -\frac{1}{\pi}\int_{-d}^{c} p(s)(x-s)\arctan\left(\frac{x-s}{y}\right)ds. \tag{2.21}$$

Then, the stress components can be obtained by substituting the scalar stress function in Eq. (2.21) into Eqs. (2.5). At this point, the stresses due to concentrated and distributed normal loads on an elastic half-space (semi-infinite elastic plane) are reviewed. These stress components are, in fact, the solution to the equilibrium equations (Eqs. (2.1)) and its compatibility equation (Eq. (2.6)) in absence of body forces.

2.4 Stresses and Deformations of an Elastic Disk on a Rigid Supporting Plane

The heavy disk's problem was first solved by Michell [70] in 1900 for the stresses in the disk which includes the body force at its center. Later, Gerl and Zippelius [32] revised the heavy disk's problem, and provided the analytical solution of stresses and deformations of the disk on the supporting rigid wall. From the heavy disk's problem (see Fig. 2.2), we need to solve:

$$\frac{\partial\sigma_{xx}}{\partial x} + \frac{\partial\sigma_{xy}}{\partial y} = 0, \qquad \frac{\partial\sigma_{xy}}{\partial x} + \frac{\partial\sigma_{yy}}{\partial y} = \rho g, \qquad \nabla^2\left(\sigma_{xx} + \sigma_{yy}\right) = 0, \tag{2.22}$$

where ρg is the body force per unit area with ρ and g denoting the mass density and gravitational acceleration, respectively. Since equations of equilibrium of the disk

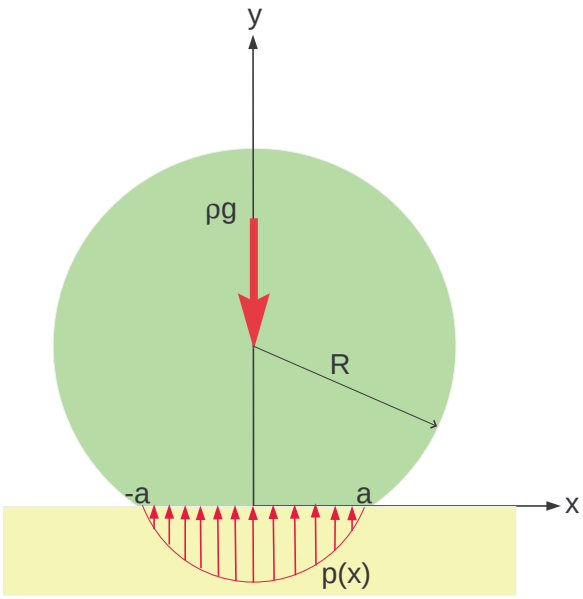

Figure 2.2: Normal loads on an elastic heavy disk sitting on a rigid plane: ρg is the body force of the disk per unit area, $p(x)$ is the compressive contact pressure over region $-a \leq x \leq a$ with ρ and g being the mass density of the disk and gravitational acceleration, respectively.

that includes the body force are non-homogeneous differential equation, the solution (total stresses) consists of two parts: $\sigma = \sigma^H + \sigma^P$ with H and P denoting the short notation for homogeneous solution and particular solution, respectively.

We first find the solution to the homogeneous differential equations where the term on the right side of the second equation in Eqs. (2.22) is dropped out. This is, in fact, the equilibrium equations in absence of body force. Recall that the solution (σ^H) to the homogeneous differential equations (Eqs. (2.22) for $\rho g = 0$) is given in Eqs. (2.19). Hence, this solution is due to the Hertzian contact pressure where the normal pressure $p(x)$ distributed inside the contact region $-a \leq x \leq a$ of disk is given

by (see e.g., Gerl and Zippelius [32], Johnson [45])

$$p(x) = \frac{2P}{\pi a^2}\left(a^2 - x^2\right)^{1/2}, \tag{2.23}$$

where a is the semi-contact width, P is the compressive force per unit length (thickness of the disk) and given by (see e.g., Gerl and Zippelius [32])

$$a = \left(\frac{4PR}{\pi E}\right)^{1/2}, \qquad P = mg = \pi R^2 \rho g, \tag{2.24}$$

with m, R, E being the mass, radius and Young's modulus of the disk, respectively. Hence, σ^H, the stresses due to the distributed normal pressure $p(x)$ over the contact region $-a \leq x \leq a$, can be evaluated by substituting Eq. (2.23) into Eq. (2.19)

$$\begin{aligned}
\sigma^H_{xx}(x,y) &= -\frac{4Py}{\pi^2 a^2}\int_{-a}^{a} \frac{(a^2-s^2)^{1/2}(x-s)^2}{\left[(x-s)^2+y^2\right]^2} ds, \\
\sigma^H_{yy}(x,y) &= -\frac{4Py^3}{\pi^2 a^2}\int_{-a}^{a} \frac{(a^2-s^2)^{1/2}}{\left[(x-s)^2+y^2\right]^2} ds, \\
\sigma^H_{xy}(x,y) &= -\frac{4Py^2}{\pi^2 a^2}\int_{-a}^{a} \frac{(a^2-s^2)^{1/2}(x-s)}{\left[(x-s)^2+y^2\right]^2} ds.
\end{aligned} \tag{2.25}$$

Obviously, it is complex to integrate the equations to get the stresses even through the distributed pressure is given. However, the stresses are possible to be evaluated along the axis of symmetry ($x = 0$), and we get (see also Gerl and Zippelius [32])

$$\begin{aligned}
\sigma^H_{xx}(0,y) &= -\frac{2P}{\pi a^2}\left[\frac{a^2+2y^2}{(a^2+y^2)^{1/2}} - 2y\right], \\
\sigma^H_{yy}(0,y) &= -\frac{2P}{\pi}(a^2+y^2)^{-1/2}, \\
\sigma^H_{xy}(0,y) &= 0.
\end{aligned} \tag{2.26}$$

Next, the particular solution σ^P to the non-homogeneous equations (equilibrium equations in presence of body force, Eqs. (2.22)) is considered. This solution was first

solved by Michell [70]. From his work the stress components of the disk due to the body force ρg per unit area are given by

$$\begin{aligned}
\sigma^P_{xx}(x,y) &= -\frac{1}{2}\rho g(y-R) + \frac{1}{2}\rho g R = -\frac{1}{2}\rho g(y-2R), \\
\sigma^P_{yy}(x,y) &= \frac{1}{2}\rho g(y-R) + \frac{1}{2}\rho g R = \frac{1}{2}\rho g y, \\
\sigma^P_{xy}(x,y) &= \frac{1}{2}\rho g x.
\end{aligned} \tag{2.27}$$

Note that stresses due to gravitation to the coordinate system whose the origin lies in the contact point between the disk and rigid plane (see page 51 from Michell [70]) contribute to the first terms of Eqs. (2.27). The second term of σ^P_{xx} and σ^P_{yy} is due to the uniform vertical upward force over the boundary (uniform biaxial tension stress: $\sigma^P_{xx} = \sigma^P_{yy} = \rho g R/2$). Also, the stresses σ^P satisfy the equilibrium equations (Eqs. (2.22)). Then, the stresses σ^P along the axis of symmetry ($x = 0$) can be evaluated by using Eqs. (2.24) as

$$\begin{aligned}
\sigma^P_{xx}(0,y) &= -\frac{P}{2\pi R^2}(y-2R), \\
\sigma^P_{yy}(0,y) &= \frac{P}{2\pi R^2} y, \\
\sigma^P_{xy}(0,y) &= 0.
\end{aligned} \tag{2.28}$$

As a result, the total stresses (complete solution) on the disk along the axis of symmetry ($x = 0$) can be obtained by superimposing the stresses in absence of body force (homogeneous solution σ^H in Eqs. (2.26)) and stresses in presence of body force

(particular solution σ^P in Eqs. (2.28)): (see also Gerl and Zippelius [32])

$$\begin{aligned}
\sigma_{xx}(0,y) &= -\frac{P}{\pi}\left[\frac{2(a^2+2y^2)}{a^2(a^2+y^2)^{1/2}} - \frac{4y}{a^2} + \frac{(y-2R)}{2R^2}\right], \\
\sigma_{yy}(0,y) &= -\frac{P}{\pi}\left[\frac{2}{(a^2+y^2)^{1/2}} - \frac{y}{2R^2}\right], \\
\sigma_{xz}(0,y) &= 0.
\end{aligned} \tag{2.29}$$

The total deformation (compression) of the elastic disk along the axis of symmetry (y-axis in Fig. 2.2) can then be calculated from the total stresses (Eqs. (2.29)). Under assumption of plane stress, the total compression ξ of the disk corresponding to the normal strain ϵ_{yy} (Eqs. (2.4)), together with using stresses (Eqs. (2.29)), is computed by integrating ϵ_{yy} from $y = 0$ to $y = 2R$ for small deformation ($a \ll R$)

$$\xi = -\int_0^{2R} \epsilon_{yy} dy = \frac{P}{\pi E}\left[2\ln\left(\frac{4R}{a}\right) - 1 - \nu\right]. \tag{2.30}$$

By substituting the semi-contact width a in Eqs. (2.24), the normal deformation (total compression) of the disk contact to rigid plane becomes (see also Gerl and Zippelius [32])

$$\xi = \frac{P}{\pi E}\left[\ln\left(\frac{4\pi RE}{P}\right) - 1 - \nu\right]. \tag{2.31}$$

The equation of normal deformation of the disk above will be used in the following chapter for the Hertzian-type force for the disk (2D particle).

Chapter 3

Mathematical Models and Algorithms

3.1 Introduction

This chapter contains the mathematical models and algorithms to be used in the coupled Discrete Element Method-Finite Element Method (DEM-FEM) code. A new approach to determine the dissipative or damping parameter for the nonlinear (Hertzian-type) contact force model for 2D disks is discussed in detail. The detailed description of the algorithms for the 2D coupled DEM-FEM model is also presented. The contents in this chapter are outlined as followed: review of an efficient of the particle-pair contact detection used in the code; the contact kinematics for a coupled DEM-FEM model followed by the contact force models including linear and nonlinear spring-dashpot models; the rolling resistance model used; a new approach for evaluating the damping parameters for the nonlinear contact force model is introduced

and calibrated in a simple way from the dropping particle test; the equations of motion of the discrete particle and finite element beam are reviewed; the explicit time integration for the DEM and FEM; and the algorithm for the 2D coupled DEM-FEM.

3.2 Particle-Pair Contact Detection

For simulation with discrete element method (DEM) or molecular dynamics (MD), a significant part of the computational effort is used in particle-pair contact detection. At every time step, the contact detection algorithm needs to detect the family of particles in contact with each particle. The contact detection algorithm consists of two processes: "spatial sorting" and "spatial resolution". The spatial sorting constructs the list of interaction pairs of particles, called a "list of contact candidates", by checking every particle against every other particle within the searched region. This is the most time consuming task in the calculation. Then, the actual contact of the particles in the list of contact candidates is checked. In the simple approach, the spatial sorting requires the computational time proportional to N_p^2, where N_p is the number of particles. Algorithms have been developed for fast particle-pair detection in particle simulations, for example, grid search (see Buchholtz and Pöschel [12]), linked-cell (see Cundall and Hart [20]), boxing (see Iwai et al. [41]) and screening contact detection (see Munjiza [75]) methods. Such algorithms reduce the complexity

to $O(N_p)$. In our "BobKit" code we combine the screening contact detection and boxing algorithms to implement and use for all simulations in this dissertation due to simplicity and efficiency.

Similar to other particle-pair detection methods, the computational domain in the "BobKit" code is first divided into rectangular boxes (cells) for particle mapping. Here, the screening contact detection (see Munjiza [75]) method is used and implemented by mapping each particle to one and only one cell. At this stage a two-dimensional array called "screening array" and one-dimensional array called "singly connected list" are constructed. In a cell, the first particle called "head" is constructed in the screening array while other particles within the same cell are associated by the singly connected list. For example, a mapping of 9 particles onto cells is shown in Fig. 3.1a. According to our "BobKit" code, the corresponding screening array C and the singly connected list E become

$$C = \begin{bmatrix} 0 & 0 & 0 & 0 & 0 & 0 & 0 & 0 & 0 \\ 0 & 0 & 0 & 0 & 0 & 0 & 9 & 0 & 0 \\ 0 & 0 & 0 & 0 & 0 & 0 & 0 & 0 & 0 \\ 0 & 0 & 0 & 0 & 0 & 0 & 0 & 0 & 0 \\ 0 & 0 & 0 & 0 & 0 & 6 & 4 & 0 & 0 \\ 0 & 0 & 0 & 0 & 0 & 8 & 0 & 0 & 0 \\ 0 & 0 & 0 & 0 & 0 & 0 & 0 & 0 & 0 \end{bmatrix}, \quad E = \begin{bmatrix} 0 & 1 & 0 & 2 & 3 & 0 & 5 & 0 & 7 \end{bmatrix}. \tag{3.1}$$

Here, two arrays of $E = E(N_p)$ and $C = C(NC_X, NC_Y)$ where N_p is the number of particles and NC_X represents the number of cells in X-axis are constructed. Note

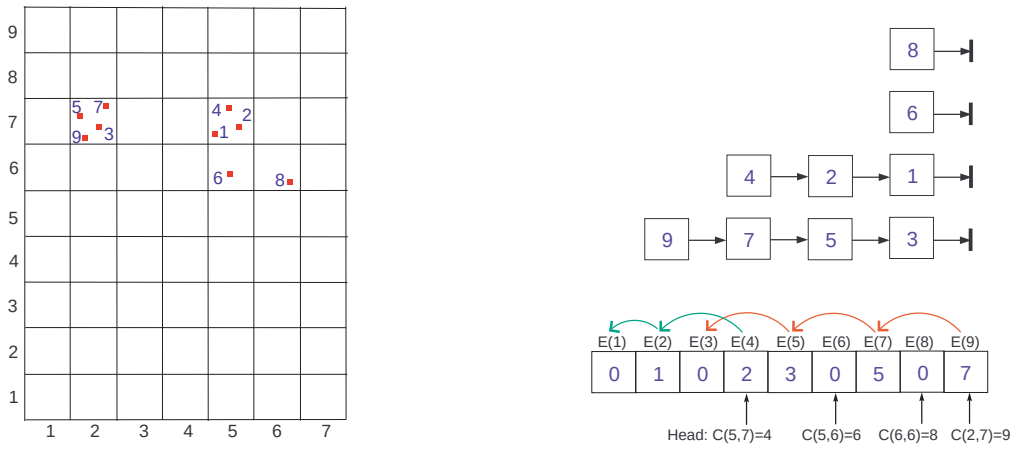

(a) (b)

Figure 3.1: (a) Mapping of particles onto the cells for the screening contact detection method. (b) The corresponding singly connected list E of size N_p with N_p being the total number of particles. The first particle in the connected list (head of the list) is extracted from the screening array C, while the rest of the list is represented by the singly connected list E.

that the number of "0" is used for representing the empty cells (no particle in the cells) in the screening array C, and for indicating the end of the singly connected list E (see Eq. (3.1)). This process is provided in Algorithm 1 from line 4-11. One can see that the method of screening contact detection is quite simple and very easy to implement.

At the next stage the boxing (see Iwai et al. [41]) method is used and implemented. For this method the overlap of particles is checked only for the candidate particles within the search region where a candidate particle may collide with the target particle. A schematic view for searching of the candidate particles within the search region for particle i (target particle) is shown in Fig. 3.2. Based on the boxing

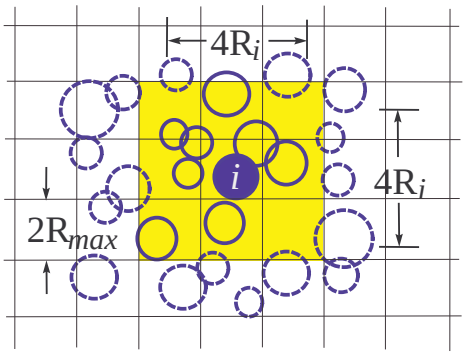

Figure 3.2: Schematic view of the boxing method for particle i (target particle). The candidate particles are drawn by by solid lines and the search region for the target particle is shaded by the (yellow) rectangular area.

method, the search region for the particle i can be expressed as

$$SR = SR(x + L_i, y + L_i), \quad -S \leq L_i \leq S, \tag{3.2}$$

where $x = \lfloor X_i/D \rfloor + 1$ denotes the non-zero cell index with X_i representing the particle position in X-axis, $S = \lceil 2R_i/D \rceil$ is the search range, $D = 2R_{max}$ is the cell size, and $R_{max} = \texttt{max}R_i, i = 1, 2, ..., N_p$ is the maximum radius of all particles with R is the particle radius. Here, the rounds to the nearest integer for $\lfloor \cdot \rfloor$ (floor) and $\lceil \cdot \rceil$ (ceil) are used. Two important steps are required for the boxing method: "extracting all particles in a candidate cell" and "checking overlap of particles". Procedure to extract all particles in the candidate cell constructed from the screening contact detection method are as follows: (see Fig. 3.1b)

1. The first particle (head) is the value of the screening array C corresponding to the particle position.

Algorithm 1 Program code of contact detection (for particle-particle in contact) implemented in our "BobKit" code with N_p and N_c being the number of particles and number of contacts of each particle. $D = 2R_{max}$ defines the cell size where $R_{max} \equiv \texttt{max}R_i, i = 1, 2, ..., N_p$ is the maximum radius of the particles. $NC_X = (X_{max} - X_{min})/D$ represents the number of cells in X-axis. Note that $\vec{r}_i$ represents the position of particle i.

```
1: list = 0 {initialize the "contact list" list = list(N_p, N_c)}
2: C = 0 {initialize the "screening array" C = C(NC_X, NC_Y) and "singly connected list" E = E(N_p)}
3: E = 0
4: for all i = 1 to N_p do
5:     x = ⌊X_i/D⌋ + 1 {compute cell index (x, y) corresponding to the position (X_i, Y_i) of particle i}
6:     y = ⌊Y_i/D⌋ + 1
7:     if C(x, y) ≠ 0 then
8:         E(i) = C(x, y) {update singly connected list E}
9:     end if
10:    C(x, y) = i {update screening array C}
11: end for
12: for all i = 1 to N_p do
13:    counter = 0 {initialize contacting components for particle i}
14:    S = ⌈2R_i/D⌉ {compute search range S for particle i}
15:    for all m = −S to S do
16:        for all n = −S to S do
17:            r = x + m {update cell index (r, s) occupied by the candidate particles within the search region}
18:            s = y + n
19:            if ((r ≥ 1) & (r ≤ NC_X)) & ((s ≥ 1) & (s ≤ NC_Y)) then
20:                if C(r, s) ≠ 0 then
21:                    j = C(r, s) {set candidate particle j within the search cell from the screening array C(r, s)}
22:                    if (i < j) then
23:                        if R_i + R_j − ‖r⃗_i − r⃗_j‖ > 0 then
24:                            counter = counter + 1 {count the overlapping particle j within the search region}
25:                            list(i, counter) = j {update contact list for particle i for only larger particle index j}
26:                        end if
27:                    end if
28:                    while E_j ≠ 0 do
29:                        j = E(j) {set candidate particle j within search cell from the singly connected list E(j)}
30:                        if (i < j) then
31:                            if R_i + R_j − ‖r⃗_i − r⃗_j‖ > 0 then
32:                                counter = counter + 1 {count the overlapping particle j within the search region}
33:                                list(i, counter) = j {update contact list for particle i for only larger particle index j}
34:                            end if
35:                        end if
36:                    end while
37:                end if
38:            end if
39:        end for
40:    end for
41: end for
```

2. The second particle is the value of the singly connected list E whose its index is the same as the head, stop if the second particle is 0 (there is only one particle in the cell).

3. The next particle is the value of the connected list E whose its index is the same as the index of the preceding particle.

4. Repeat step 3 until the value of the connected list E is 0 (there is no more particle in the cell).

The particle overlap is checked by using Eqs. (3.3). In addition, the boxing method introduces Newton's 3^{rd} law so that only one particle from the contact pair is needed for overlap checking. This reduces the computational effort. The process for checking of particle overlap based on the boxing method is given in Algorithm 1 from line 12-41. A program code of contact detection for particle-particle in contact implemented in our coupled DEM-FEM code is given in Algorithm 1. The "BobKit" code confirms that the CPU time is linear with the number of particles in the systems.

3.3 Contact Kinematics

A general contact between particle-particle and particle-beam element in a 2D coupled DEM-FEM simulation in this dissertation is depicted in Fig. 3.3. In the

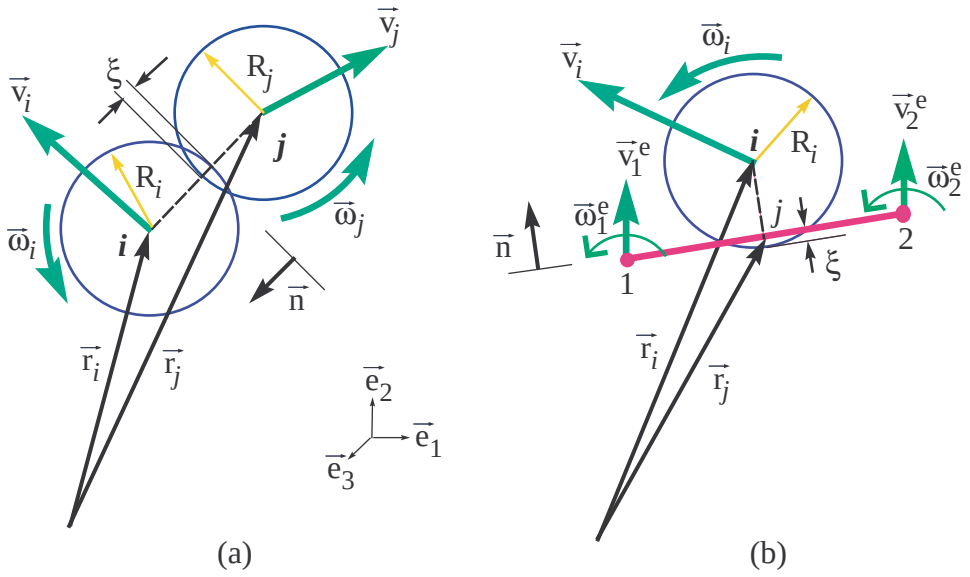

Figure 3.3: Contact kinematics: (a) particle-particle, (b) particle-beam element.

figure, the mutual compression (normal deformation) of the particles i and j for contact of 2D particles is computed as

$$\xi = \begin{cases} R_i + R_j - \|\vec{r}_i - \vec{r}_j\| > 0, & \text{pp contact;} \\ R_i - \|\vec{r}_i - \vec{r}_j\| > 0, & \text{pb (or pw) contact,} \end{cases} \tag{3.3}$$

where "pp", "pb", and "pw" contacts are the short notation for particle-particle, particle-beam, and particle-wall, respectively. Note that the thickness of all particles is the same as that of the bottom beam and walls. The unit normal vector of the contacting pair (i, j) is used to decompose the contact force into normal direction, and defined as

$$\vec{n} = \frac{\vec{r}_i - \vec{r}_j}{\|\vec{r}_i - \vec{r}_j\|}. \tag{3.4}$$

The corresponding unit tangential vector is assigned from the vector product as

$$\vec{t} = -\vec{e}_3 \times \vec{n}, \tag{3.5}$$

with $\vec{e}_3$ being the unit vector normal to the plane (out of plane) where the basis of the unit vectors is defined as $\vec{e}_3 = \vec{e}_1 \times \vec{e}_2$. The contact velocity of the contacting pair (i, j) is computed as

$$\vec{v}_{ij}^{c} = \begin{cases} (\vec{v}_i + \vec{\omega}_i \times \vec{R}_i^c) - (\vec{v}_j + \vec{\omega}_j \times \vec{R}_j^c), & \text{pp contact;} \\ (\vec{v}_i + \vec{\omega}_i \times \vec{R}_i^c) - [(v_1^e H_1^e + v_2^e H_3^e)\vec{e}_2 + (\omega_1^e H_2^e + \omega_2^e H_4^e)\vec{e}_3], & \text{pb contact;} \\ (\vec{v}_i + \vec{\omega}_i \times \vec{R}_i^c) - (\vec{v}_w + \vec{\omega}_w \times \vec{R}_w^c), & \text{pw contact,} \end{cases} \tag{3.6}$$

where $\vec{v}_i$ and $\vec{v}_j$ are the translational velocity vectors of the center of particle i and j, $\vec{\omega}_i$ and $\vec{\omega}_j$ are the angular velocity vectors of particle i and j, and $\vec{R}_i^c$ and $\vec{R}_j^c$ are the vectors pointing from the center of particle i and j to the contact point of the contacting pair (i, j) with its magnitude equal to the particle radius R_i and R_j, respectively. The expression of $(v_1^e H_1^e + v_2^e H_3^e)\vec{e}_2 + (\omega_1^e H_2^e + \omega_2^e H_4^e)\vec{e}_3$ represents the velocity of the linear beam element e contacting to a particle (see e.g., Kwon and Bang [57], Reddy [86]). v_i^e and ω_i^e $(i = 1, 2)$ are the magnitudes of translational and angular velocities of the local node i of the linear beam element e. H_i^e $(i = 1, 2, 3, 4)$ is the corresponding Hermite shape function of the beam element e. $\vec{v}_w$ is the translational velocity vector of a node to form a wall, and $\vec{R}_w^c$ is the vector pointing from the node to the contact point. It should be noted that the formulation of contact velocity between particle (DEM) and beam element (FEM) is similar to Onate and

Rojek [78] except that in their model they do not include the contributions from the angular velocity because they used linear triangular (2D) elements to discretize the finite element part for 2D simulations.

3.4 Contact Forces

By use of the normal and tangential vectors in the preceding section, the contact force is decomposed into normal and tangential forces. In this section, the force models for linear and nonlinear contacts are discussed. For the normal force component, the linear spring-dashpot model proposed by Cundall and Strack [19] is used as the linear contact model, while the normal force model by Gerl and Zippelius [32] for disks as given in Eq. (2.31) is used as the nonlinear contact model. The tangential force model by Cundall and Strack [19] is used. In addition, the rolling resistant model to compute the resisting moment due to rolling friction is given. The normal force $\vec{F}_{ij}^{n}$ of the contacting pair (i, j) as shown in Fig. 3.4 for viscoelastic particles is decomposed into elastic $\vec{F}_{ij}^{ne}$ and damping (dissipative) $\vec{F}_{ij}^{nd}$ parts:

$$\vec{F}_{ij}^{n} = \vec{F}_{ij}^{ne} + \vec{F}_{ij}^{nd} = F^{n}\vec{n} = \left(F^{ne} + F^{nd}\right)\vec{n}. \tag{3.7}$$

The tangential force against the Coulomb friction between contact interface with no dissipative component is given by Cundall and Strack [19]

$$\vec{F}_{ij}^{t} = F^{t}\vec{t}, \tag{3.8}$$

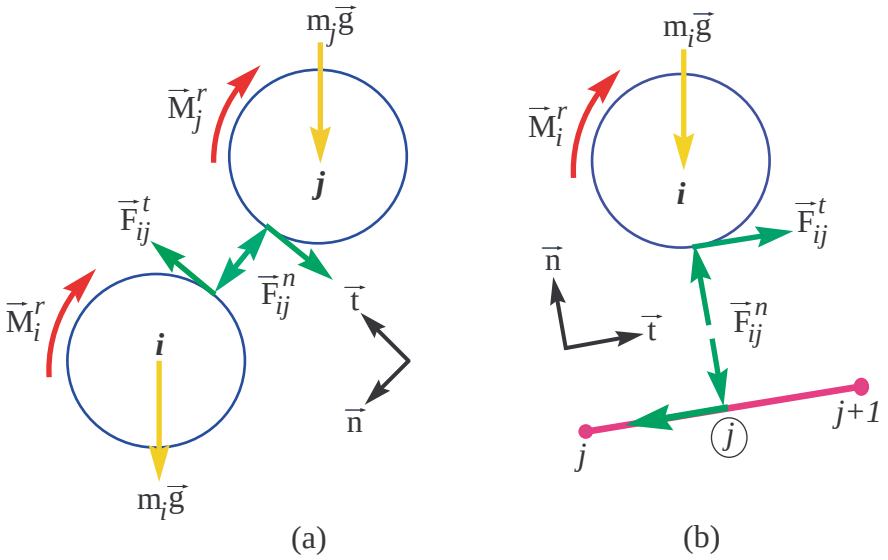

Figure 3.4: Model of contact forces: (a) particle-particle, (b) particle-beam element.

where

$$F^t = -\min\left(K_t|\zeta|, \mu_s|F^n|\right) \cdot \text{sign}(\zeta), \tag{3.9}$$

with μ_s being the coefficient of sliding friction, ζ denoting the total (accumulated) tangential displacement, and K_t being the tangential stiffness coefficient. The total tangential displacement is computed from the tangential contact velocity as

$$\zeta(t) = \int_{t_0}^{t} v_t(\tilde{t}) d\tilde{t}, \tag{3.10}$$

where $v_t(\tilde{t})$ is the magnitude of tangential velocity at the contact point, t_0 is the time as the first contact established. Here, the superscripts representing contact pair (i, j) are dropped out for simplification. From the contact forces in Eq. (3.7) and (3.8), it can be seen that the energy is dissipated via the normal contact force in presence

of inelastic contact where the damping force F^{nd} is computed from the product of the normal damping coefficient and the normal velocity at the contact point. As a particle in contact (DEM simulation), the computational time step $\Delta t^{\texttt{DEM}}$ for both linear and nonlinear force models is the same and relates to the Rayleigh time t_R (see e.g., Ji and Shen [44])

$$t_R = \frac{\pi R}{0.16\nu + 0.88}\sqrt{\frac{\rho}{G}}, \tag{3.11}$$

where R is the particle radius, ρ is the particle density, ν is the Poisson's ratio and $G = E/[2(1+\nu)]$ is the shear modulus with E being the Young's modulus. The Rayleigh time t_R is the time required for the Rayleigh waves travel through the contact particle. As a result, the Rayleigh time t_R must be larger than the time step of the contact particle $\Delta t^{\texttt{DEM}}$ for computational stability. In our BobKit code the time step of the contact particle is a fraction of the Rayleigh time where $\Delta t^{\texttt{DEM}} = \tau t_R, 0 < \tau < 1$ with τ being the time step fraction. Note that the Rayleigh time t_R given in Eq. (3.11) explicitly depends on radius and material properties of an elastic particle. The contact forces for both linear and nonlinear spring-dashpot models are discussed in the following sections.

3.4.1 Linear Spring-Dashpot (Hookean Contact) Model

In the linear spring-dashpot model, the normal force is given by

$$F^n = \max\left(0, K_n\xi - C_n\vec{v}_{ij}^{\,c}\cdot\vec{n}\right), \tag{3.12}$$

where ξ is the normal deformation (Eq. (3.3)), $\vec{n}$ is the normal unit vector (Eq. (3.4)), $\vec{v}_{ij}^{c}$ is the contact velocity of the contacting pair (i, j) (Eq. (3.6)), K_n and C_n are the normal stiffness and damping coefficients. It should be noted that the normal force in Eq. (3.12) represents a repulsive force. No attractive force is included. The coefficients (K_n, C_n) are related to the coefficient of normal restitution ϵ_n and collision time (time in contact) t_c by (see e.g., Schafer et al. [89])

$$\begin{aligned} \epsilon_n &= \exp\left(-\frac{C_n t_c}{2m^*}\right), \\ t_c &= \pi\left[\frac{K_n}{m^*} - \left(\frac{C_n}{2m^*}\right)^2\right]^{-1/2}, \end{aligned} \tag{3.13}$$

where m^* is the reduced mass which is computed as

$$\frac{1}{m^*} = \frac{1}{m_1} + \frac{1}{m_2}, \tag{3.14}$$

with m_i $(i = 1, 2)$ being the mass of the contact pair. The tangential stiffness K_t in Eq. (3.9) for the linear spring-dashpot model can be calculated from

$$K_t = \begin{cases} \frac{m^*}{(1+mR^2/I)}\left(\frac{\pi}{t_c}\right)^2, \\ \kappa K_n, \end{cases} \tag{3.15}$$

where κ is the stiffness ratio, I is the mass moment of inertia of the particle. Substituting the collision time t_c in Eqs. (3.13) into the tangential stiffness K_t in Eq. (3.15) leads to $K_t \simeq K_n/3$ for the thin disk where $I = mR^2/2$. However, the tangential force implemented in this dissertation for the linear spring-dashpot model is based on the stiffness ratio κ, where the contact parameters (K_n, K_t) are related to the material

parameters as pointed out by Renzo and Maio [87], is given by (see e.g., Johnson [45], Renzo and Maio [87])

$$\kappa = \left(\frac{1-\nu_1}{G_1} + \frac{1-\nu_2}{G_2} \right) \left(\frac{1-\nu_1/2}{G_1} + \frac{1-\nu_2/2}{G_2} \right)^{-1}. \tag{3.16}$$

The linear spring-dashpot model is a simple model used to represent the real contact behavior of particles by means of the constant normal restitution coefficient ϵ_n and collision time t_c as given in Eqs. (3.13). Thus, precise evaluation of the two parameters corresponding to the contact behavior is required. Since the implementation of the model is straightforward and gives reasonable results in simulations of granular flow, the model has been used by many researchers (see e.g., Cleary and Sawley [18], Haff and Werner [35], Kuo et al. [55], Schäfer et al. [89], Taguchi [95], Thompson and Grest [96], Zhang and Whiten [109]).

3.4.2 Nonlinear Spring-Dashpot (Hertzian Contact) Model

The normal force for the nonlinear spring-dashpot model based on Hertzian contact implemented in this dissertation for a disk is given in Eq. (2.31). The equation implies that the compression ξ a disk is simply computed from a given normal load P per unit thickness and material properties of the disk. In DEM one first computes the compression of a particle, and from there, using a particular contact model, the normal forces are obtained. For contacting of a 2D particle (disk of finite thickness)

and rigid wall, the normal force ($F^{ne} = P$) per unit thickness of the particle can be obtained by solving Eq. (2.31) as (see Gerl and Zippelius [32], Schwager [90])

$$F^{ne} = -\frac{\pi E\xi}{\mathrm{W}_0\left[-\xi \exp\left(1+\nu\right)/(4R)\right]} \simeq -\frac{\pi E\xi}{\ln\left[-\xi \exp\left(1+\nu\right)/(4R)\right]}, \tag{3.17}$$

Note that the function $\mathrm{W}_0(x)$ is the zeroth Lambert W function of small negative value x and can be approximated as (see Schwager [90])

$$\mathrm{W}_0(x) \simeq -\ln\left(-\frac{1}{x}\right) - \ln\left(\ln\left(-\frac{1}{x}\right)\right). \tag{3.18}$$

In our coupled DEM-FEM code the damping force F^{nd} for viscoelastic particle is included in the normal force model to dissipate the restoring (elastic) force F^{ne}. For small impact velocity (quasi-static regime) the damping force in the normal direction becomes (see Schwager [90])

$$F^{nd} = A\dot{\xi}\frac{\partial F^{ne}}{\partial \xi} \simeq -\frac{\pi AE\dot{\xi}}{1+\ln\left[-\xi \exp\left(1+\nu\right)/(4R)\right]}, \tag{3.19}$$

where A is the damping parameter relating to the material properties and geometry such as the radius of particle, $\dot{\xi}$ is the normal contact velocity. Thus, the total normal force per unit length (thickness) for the nonlinear spring-dashpot model based on the Hertzian contact can be expressed as

$$F^n = \max\left(0, K_n\xi - C_n\vec{v}_{ij}^{\,c}\cdot\vec{n}\right), \tag{3.20}$$

where

$$K_n = \frac{\pi E}{\ln\left[4R/\xi \exp\left(1+\nu\right)\right]}, \tag{3.21}$$

$$C_n = \frac{\pi AE}{\ln\left[4R/\xi \exp\left(1+\nu\right)\right] - 1}, \tag{3.22}$$

with K_n and C_n denoting the normal stiffness and damping coefficients. It can be seen that the coefficients (K_n, C_n) are nonlinear in compression ξ. The tangential stiffness K_t used in Cundall and Strack [19] in Eq. (3.9) is based on Mindlin and Deresiewicz [72] for no slip condition, and given by

$$K_t = 8G^* a, \tag{3.23}$$

where a is the contact width given in Eqs. (2.24), G^* is the reduced shear modulus and can be computed from the relation

$$\frac{1}{G^*} = \frac{2-\nu_1}{G_1} + \frac{2-\nu_2}{G_2}. \tag{3.24}$$

One advantage of the nonlinear spring-dashpot (Hertzian contact) model over the linear model is that the contact force for the nonlinear model is based on the material properties of particles. Hence, simulation of a system of particles based on Hertzian-type force agrees better with experimental results (see e.g., Falcon et al. [29], Zhang and Whiten [109]). However, selecting an appropriate damping parameter for the desired dynamic simulation system is still in question, especially for the 2D disks. The evaluation of the damping parameter is discussed in section section 3.5.

3.4.3 Rolling Resistance Model

The rolling resistance is defined as the resisting moment that slows down the particle's rotation (see Johnson [45]). It has been reported in the published literature (see e.g., Iwashita and Oda [42], Zhou et al. [110], Zhu and Yu [112]) that rolling resistance helps improve numerical stability and gives results that are more physical. The resisting moment vector $\vec{M}_i^r$ due to rolling friction acting on particle i is

$$\vec{M}_i^r = -M_i^r \frac{\vec{\omega}_i}{\|\vec{\omega}_i\|}, \tag{3.25}$$

where M_i^r is the magnitude of the resisting moment acting on particle i, $\vec{\omega}_i$ is the angular velocity vector of particle i, and $\|\cdot\|$ denotes the magnitude of a vector. A simple model for computing the resisting moment M_i^r can be found from mechanics textbooks or published literature (see e.g., Beer and Johnston [7], Brilliantov and Pöschel [10], Johnson [45]). Three models that are generally used to compute the resisting moment in DEM simulations are:

$$M_i^r = \begin{cases} \mu_r^{BJ} F^n, & \text{Beer-Johnston model;} \\ \mu_r^J R_i F^n, & \text{Johnson model;} \\ \mu_r^{BP} V_\omega F^n, & \text{Brilliantov and Pöschel model,} \end{cases} \tag{3.26}$$

where μ_r^{BJ}, μ_r^J and μ_r^{BP} are the rolling friction coefficients. F^n is the normal force. V_ω is the magnitude of contact tangential velocity contributed from the angular velocity of the contact pair $V_\omega = \|\vec{\omega}_i \times \vec{R}_i^c - \vec{\omega}_j \times \vec{R}_j^c\|$. It should be noted that the units of the coefficients of rolling friction are meter in Beer-Johnston model, non-dimensional

in Johnson's model, and second in Brilliantov and Pöschel model. However, Zhou et al. [110] concluded that the rolling resistance model independent on angular velocity, like Beer-Johnston and Johnson models, gave preferable results of the sandpile formation simulations. In this dissertation, the rolling resistance model according to Johnson where the rolling friction coefficient μ_r^J is a non-dimensional coefficient is implemented.

3.5 Damping Parameter for Hertzian-Type Force

In this section, evaluation of the damping parameter for Hertzian-type force is described. Based on Hertzian contact the existing damping parameter for (3D) spherical particles is first reviewed. Then, a new approach of evaluating the damping parameter for (2D) disk particles is proposed and used in our coupled DEM-FEM model.

3.5.1 Existing Formula of Damping Parameter for (3D) Spherical Particles

From Brilliantov et al. [11], the damping parameter A for spherical particles in contact was derived in term of material parameters as

$$A = \frac{1}{3}\frac{(3\eta_2 - \eta_1)^2}{(3\eta_2 + 2\eta_1)}\frac{(1-\nu^2)(1-2\nu)}{E\nu^2}. \tag{3.27}$$

Here, η_1, η_2 are the material viscosity, E and ν are Young's modulus and Poisson's ratio of the spherical particle, respectively. Schawger and Pöschel [91] solved the differential equation of motion for colliding viscoelastic spheres and showed that the coefficient of normal restitution depends on the impact velocity g_n as,

$$\epsilon_n = 1 - 1.15344A\left(K_n/m^*\right)^{2/5} g_n^{1/5} + 0.79826A^2\left(K_n/m^*\right)^{4/5} g_n^{2/5} + ..., \qquad (3.28)$$

with $K_n = \frac{4}{3}E^*\sqrt{R^*}$ being the normal stiffness of spherical contact. For quasi-static impact (small impact velocity), the Eq. (3.28) becomes $1 - \epsilon_n \propto g_n^{1/5}$ and implies that ϵ_n decreases as the impact velocity increases. A similar relation is also obtained by Brilliantov et al. [11], Kuwabara and Kono [56], Morgado and Oppenheim [74], Ramírez et al. [83]. The theoretical result between impact velocity and coefficient of restitution agrees with the experiment conducted by Kuwabara and Kono [56], Labous et al. [58], Sondergaard et al. [94].

Brilliantov and Pöschel [10] proposed the rolling resistant model as given in Eq. (3.26) and noted that the rolling friction coefficient μ_r^{BP} coincides with the damping parameter A; that is $A = \mu_r^{BP}$ where both units are in second. This implies that the coefficient of rolling friction can be calculated from the normal restitution coefficient of the same material. For example, from Eq. (3.28), $1 - \epsilon_n \simeq 1.15344A\left(K_n/m^*\right)^{2/5} g_n^{1/5}$, for a particle of mass $m = 10^{-2}$ kg with impact velocity $g_n = 1$ m/s and $\left(K_n/m^*\right)^{2/5} \simeq 10^5$ $(\mathrm{kg}^2/\mathrm{ms}^4)^{1/5}$, the coefficient of restitution, which is the same as the coefficient of

rolling friction, is approximated as $A = \mu_r^{BP} \simeq 10^{-6}$ s.

3.5.2 New Approach to Evaluate Damping Parameter for (2D) Disk Particles

As pointed out in the preceding section, the damping parameter A for the Hertzian-type contact model depends on material properties such as elastic modulus, Poisson's ratio and viscosity. For spherical particles, computing the damping parameter from analytical formula as given in Eq. (3.27) requires the evaluation of the material viscosity (η_1 and η_2). To obtain the viscous constants an experiment is required because these quantities are difficult to find in tables of material properties. Hence, evaluating the damping parameter using simulations seems more appropriate. A simple and direct way for evaluating the damping parameter is to calibrate it, using numerical simulation, so that the coefficient of restitution obtained from the impact of a particle with a rigid wall is matched to a preset value. The same can be done for the linear model, so that the two models can be compared, in their performance, for the "same material", meaning materials with the same restitution coefficient. The comparison will be performed using the velocity after the impact with the rigid wall in order to produce a material with a restitution coefficient of 0.6 and 0.9. Using this for both the linear and the nonlinear models we ensure that, at least to a first-order degree, the same amount of energy is dissipated by the two contact force models during impact.

From a dropping particle test where a disk particle is dropped onto a rigid wall, the impact is described by the normal restitution coefficient ϵ_n as

$$\epsilon_n = -\frac{v_n^f}{v_n^i} \in [0, 1], \tag{3.29}$$

where v_n is the impact velocity with the superscript i for pre-collision (initial) and f for post-collision (final), respectively. Note that the negative sign indicates the opposite motion of initial and final velocities.

The purpose of the test is to find the damping parameter A of the nonlinear force model corresponding to the normal restitution coefficient of 0.90 and 0.60. The parameters for the disk particles to be used in the test are as follows: radius = 1.25, 1.00, 0.625 mm., Young's modulus = 1 GPa., Poisson's ratio = 0.30. From the test, the velocity after impact from analytical results given in Eq. (3.29) is compared to the simulations. It should be noted that only final velocity of the first impact is considered here. However, the simulation results last for 2 s to observe multiple impacts of the particle. For the linear model, we choose the average value of the collision time ($t_c = 500\Delta t$) suggested by Brilliantov et al. [11], which is $t_c = (10 - 1000)\Delta t$ with Δt being the time step. This collision time gives the relative error of post-collision less than 1%. According to the information from spherical particles in the preceding section, the initial guessed value for the damping parameter A based on the Hertzian-type force is in the order of 10^{-6} s. By means of trial and error, this guess value is

Table 3.1: Damping parameter A of the nonlinear (Hertzian contact) model corresponding to the normal restitution coefficient of 0.90 and 0.60.

Particle radius (mm)	A (for $\epsilon_n = 0.90$)	A (for $\epsilon_n = 0.60$)
1.250	1.50E-6 s.	2.80E-6 s.
1.000	1.20E-6 s.	2.25E-6 s.
0.625	7.30E-7 s.	1.40E-6 s.

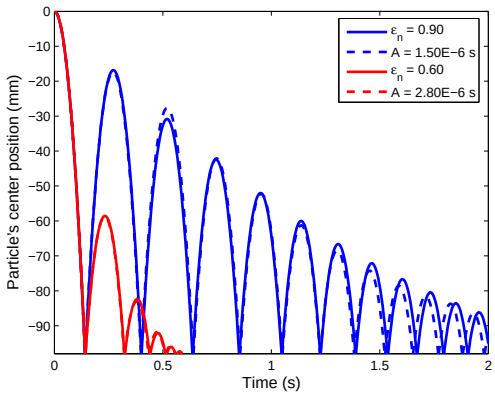

Figure 3.5: Comparison of particle dropped test (particle radius of 1.25 mm.) for linear and nonlinear spring-dashpot models: Linear spring-dashpot (Hookean contact) model with $\epsilon_n = 0.90$ (blue solid line), $\epsilon_n = 0.60$ (red solid line). Nonlinear spring-dashpot (Hertzian contact) model with A corresponding to $\epsilon_n = 0.90$ (blue dash line), A corresponding to $\epsilon_n = 0.60$ (read dash line), where ϵ_n is the coefficient of normal restitution, A is the damping parameter.

adjusted such that the relative error of the velocity after the first impact is within 1%. The damping parameter A for the Hertzian-type force of the disk particles for three particle radii are summarized in the Table 3.1. For comparison, the simulation results for both linear and nonlinear force models corresponding to the normal restitution coefficient of 0.90 and 0.60 for the particle radius of 1.25 mm are shown in Fig. 3.5.

3.6 Equations of Motion

The equations of motion for particles and Euler-Bernoulli beam are described in this section. We first give the ordinary differential equations of motion for particles. Then, the partial differential equation of motion for the slender beam in bending along with its prescribed boundary conditions is reviewed.

3.6.1 Equations of Motion for Particles

The governing equations of motion for particle i, consisting of translational and rotational motions, are described by the linear and angular momentum balance equations: (see e.g., Greenwood [34])

$$m_i \frac{d\vec{v}_i}{dt} = \sum_j \left(\vec{F}_{ij}^n + \vec{F}_{ij}^t \right) + m_i \vec{g} = \vec{F}_i^n + \vec{F}_i^t + m_i \vec{g}, \tag{3.30}$$

$$I_i \frac{d\vec{\omega}_i}{dt} = \sum_j \left(\vec{R}_i^c \times \vec{F}_{ij}^t + \vec{M}_{ij}^r \right) = \sum_j \left(\vec{R}_i^c \times \vec{F}_{ij}^t \right) + \vec{M}_i^r, \tag{3.31}$$

where m_i and I_i are mass and moment of inertia of particle i, $\vec{F}_i^n$ and $\vec{F}_i^t$ are total normal and tangential forces acting on particle i due to contacting pair j, $m_i \vec{g}$ is the body force acting on particle i, $\vec{M}_i^r$ is the total resisting moment acting on particle i and caused by rolling friction.

3.6.2 Equation of Motion for Euler-Bernoulli Beam Bending

The dynamics of transversely vibrating beams for a uniform Euler-Bernoulli beam is given in this section. The derivation for the dynamics equations for the Euler-Bernoulli beam can be found from many textbooks (see e.g., Meirovitch [69], Rao [84], [97]) or published literature (see e.g., Han et al. [38]). The beam used in the coupled DEM-FEM model in this dissertation based on the Euler-Bernoulli theory, which follows the assumptions given below:

- Axial dimension is considerably larger than the other two dimensions.
- The beam material is linear elastic, which obeys Hooke's law.
- The Poisson effect is neglected.
- Cross-sectional area is symmetrical so that the neutral and centroidal axes coincide.
- Planes perpendicular to the neutral axis remains perpendicular after deformation.
- Transverse shear strain is negligible.

Based on these assumptions, the Euler-Bernoulli beam theory is applicable for slender beams (ratio of beam length to thickness in the order of 20 or more). For thick beams, the Euler-Bernoulli beam theory gives a good approximations only for the

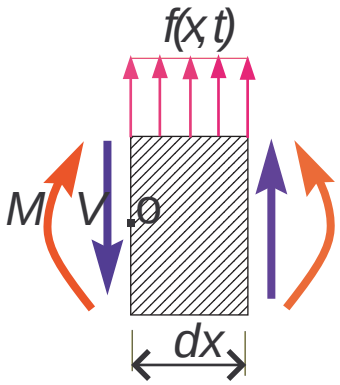

Figure 3.6: Schematic of differential beam segment. Note that the shear force and bending moment at $x + dx$ are $V + \frac{\partial V}{\partial x}dx$ and $M + \frac{\partial M}{\partial x}dx$.

lowest modes of vibration, but more accurate solutions for all vibration modes can be obtained from the Timoshenko beam theory (Timoshenko [101]). In the Timoshenko beam theory, the effects of shear and rotation are included to improve the accuracy for non-slender beams and/or high frequency responses. In this dissertation, the Euler-Bernoulli beam is used because the beam considered is a slender beam. Also, only the first mode of vibration is considered.

A free-body-diagram (FBD) for the differential beam segment exerted by a distributed force $f(x,t)$ (force per unit length), including the shear force V and bending moment M, is shown in Fig. 3.6. The equation of motion for the Euler-Bernoulli beam is obtained by summing forces acting on the beam segment as:

$$f(x,t)dx - V + \left(V + \frac{\partial V}{\partial x}dx\right) = \rho A dx \frac{\partial^2 u}{\partial t^2}, \tag{3.32}$$

which leads to

$$-\frac{\partial V}{\partial x} + \rho A \frac{\partial^2 u}{\partial t^2} = f(x,t), \tag{3.33}$$

where $u = u(x,t)$ is the transverse deflection at the axial location x and time t, ρ is the mass density and A is the cross-sectional area of the beam. By summing moments about point O and ignoring the rotational inertia, the moment equation can be obtained as

$$-M + \left(M + \frac{\partial M}{\partial x}dx\right) + \frac{1}{2}f(x,t)dx^2 + \left(V + \frac{\partial V}{\partial x}dx\right)dx - \frac{1}{2}\rho A \frac{\partial^2 u}{\partial t^2}dx^2 = 0. \tag{3.34}$$

Neglecting the higher-order of dx, the moment equation becomes

$$\frac{\partial M}{\partial x} + V = 0, \tag{3.35}$$

with the bending moment being proportional to the local curvature as $M = EI\frac{\partial^2 u}{\partial x^2}$. Combining Eq. (3.33) and (3.35) yields the partial differential equation of motion for a beam of uniform cross-section as

$$\rho A \frac{\partial^2 u(x,t)}{\partial t^2} + EI \frac{\partial^4 u(x,t)}{\partial x^4} = f(x,t), \tag{3.36}$$

where EI is defined as the effective bending stiffness of the beam, E is the Young's modulus of the beam, I is the area moment of inertia of the beam's cross-section about the neutral axis. To solve the differential equation in Eq. (3.36), the initial and boundary conditions are required. Four types of boundary conditions of interest in beam bending are given below:

- hinged end:

$$u(x,t) = 0, \frac{\partial^2 u(x,t)}{\partial x^2} = 0. \tag{3.37}$$

- clamped end:

$$u(x,t) = 0, \frac{\partial u(x,t)}{\partial x} = 0. \tag{3.38}$$

- free end:

$$\frac{\partial^2 u(x,t)}{\partial x^2} = 0, \frac{\partial^3 u(x,t)}{\partial x^3} = 0. \tag{3.39}$$

- sliding end:

$$u(x,t) = 0, \frac{\partial^3 u(x,t)}{\partial x^3} = 0. \tag{3.40}$$

3.7 Time Integration Schemes

Once the total forces and moments exerted on particles and nodal beam nodes in the coupled DEM-FEM system are calculated, the time integration is needed to approximate the position, velocity and the higher derivatives for the particles and nodal beam nodes in the next time steps. Due to the fact that the truncation error and round-off error are introduced in numerical computation, an appropriate numerical scheme is required. The selection of the numerical scheme depends on type of numerical scheme (implicit/explicit), stability, and accuracy. An explicit scheme directly computes the current time-step solution from the solution at the previous time-step,

but normally requires small time step size in order to achieve stability. In contrast, for an implicit method, the solution of a system of (possibly nonlinear) equations is required in order to compute the solution at the current time step based on the solution at the previous time steps. However, in general, no restrictions are imposed for implicit methods on the time step size for stability reasons. A numerical scheme is said to be stable if an error does not grow to be much larger during the calculation. On the other hand, the numerical scheme is unstable if the error grows without bounded during the calculation. A numerical scheme is said to be conditionally stable if it is stable only when certain restriction in step size is satisfied. The accuracy of the numerical schemes is measured in terms of the rate at which the approximate solution converges to the exact solution. In this section, the time integration schemes to be used in our coupled DEM-FEM model for particles and nodal beam nodes are reviewed.

3.7.1 Gear's Predictor-Corrector Schemes for DEM Time Integration

To update the position and higher derivatives for the particles, we use Gear's predictor-corrector time integration scheme. It is commonly used in molecular dynamics (MD) or discrete element method (DEM) simulations (see e.g., Allen and Tildesley [2], Gear [31], Pöschel and Schwager [81]). The numerical scheme is an

explicit scheme using a constant time step and containing three main stages: prediction, evaluation, and correction. In our coupled DEM-FEM code we implement the 5^{th}-order Gear's predictor-corrector scheme due to higher accuracy (see e.g., Allen and Tildesley [2], Pöschel and Schwager [81]).

Predictor: Approximate the particles' position and its derivatives at time step $t + \Delta t$ using Taylor series expansions. For the 5^{th}-order scheme, the Taylor series become

$$\begin{aligned}
\mathbf{r}_{\mathtt{pre}}(t+\Delta t) &= \mathbf{r}(t) + \Delta t\dot{\mathbf{r}}(t) + \frac{\Delta t^2}{2}\ddot{\mathbf{r}}(t) + \frac{\Delta t^3}{6}\dddot{\mathbf{r}}(t) + \frac{\Delta t^4}{24}\mathbf{r}^{\mathtt{IV}}(t) + \frac{\Delta t^5}{120}\mathbf{r}^{\mathtt{V}}(t),\\
\dot{\mathbf{r}}_{\mathtt{pre}}(t+\Delta t) &= \dot{\mathbf{r}}(t) + \Delta t\ddot{\mathbf{r}}(t) + \frac{\Delta t^2}{2}\dddot{\mathbf{r}}(t) + \frac{\Delta t^3}{6}\mathbf{r}^{\mathtt{IV}}(t) + \frac{\Delta t^4}{24}\mathbf{r}^{\mathtt{V}}(t),\\
\ddot{\mathbf{r}}_{\mathtt{pre}}(t+\Delta t) &= \ddot{\mathbf{r}}(t) + \Delta t\dddot{\mathbf{r}}(t) + \frac{\Delta t^2}{2}\mathbf{r}^{\mathtt{IV}}(t) + \frac{\Delta t^3}{6}\mathbf{r}^{\mathtt{V}}(t),\\
\dddot{\mathbf{r}}_{\mathtt{pre}}(t+\Delta t) &= \dddot{\mathbf{r}}(t) + \Delta t\mathbf{r}^{\mathtt{IV}}(t) + \frac{\Delta t^2}{2}\mathbf{r}^{\mathtt{V}}(t),\\
\mathbf{r}^{\mathtt{IV}}_{\mathtt{pre}}(t+\Delta t) &= \mathbf{r}^{\mathtt{IV}}(t) + \Delta t\mathbf{r}^{\mathtt{V}}(t),\\
\mathbf{r}^{\mathtt{V}}_{\mathtt{pre}}(t+\Delta t) &= \mathbf{r}^{\mathtt{V}}(t),
\end{aligned} \tag{3.41}$$

where $\mathbf{r}, \dot{\mathbf{r}}, \ddot{\mathbf{r}}, \dddot{\mathbf{r}}, \mathbf{r}^{\mathtt{IV}}, \mathbf{r}^{\mathtt{V}}$ are the position vector of particles and higher derivatives with the superscripts being the order of the derivatives, Δt is the time step size.

Evaluation: Compute the Difference (discrepancy) in accelerations obtained from the total forces $\mathbf{F} = m\ddot{\mathbf{r}}$ and from the predictor stage $\ddot{\mathbf{r}}$ at time step $(t + \Delta t)$. Thus, the discrepancy becomes

$$\Delta\ddot{\mathbf{r}} = \left[\ddot{\mathbf{r}}(t+\Delta t) - \ddot{\mathbf{r}}_{\mathtt{pre}}(t+\Delta t)\right]. \tag{3.42}$$

Correction: The predicted positions and higher time derivatives are corrected in this stage to improve the accuracy. Hence, the updated particle's position and higher time derivatives become

$$\begin{aligned}
\mathbf{r}_{\mathtt{cor}}(t+\Delta t) &= \mathbf{r}_{\mathtt{pre}}(t+\Delta t) + c_0\left(\frac{\Delta t^2}{2}\Delta\ddot{\mathbf{r}}\right),\\
\dot{\mathbf{r}}_{\mathtt{cor}}(t+\Delta t) &= \dot{\mathbf{r}}_{\mathtt{pre}}(t+\Delta t) + c_1\frac{1}{\Delta t}\left(\frac{\Delta t^2}{2}\Delta\ddot{\mathbf{r}}\right),\\
\ddot{\mathbf{r}}_{\mathtt{cor}}(t+\Delta t) &= \ddot{\mathbf{r}}_{\mathtt{pre}}(t+\Delta t) + c_2\frac{2}{\Delta t^2}\left(\frac{\Delta t^2}{2}\Delta\ddot{\mathbf{r}}\right),\\
\dddot{\mathbf{r}}_{\mathtt{cor}}(t+\Delta t) &= \dddot{\mathbf{r}}_{\mathtt{pre}}(t+\Delta t) + c_3\frac{6}{\Delta t^3}\left(\frac{\Delta t^2}{2}\Delta\ddot{\mathbf{r}}\right),\\
\mathbf{r}^{\mathtt{IV}}_{\mathtt{cor}}(t+\Delta t) &= \mathbf{r}^{\mathtt{IV}}_{\mathtt{pre}}(t+\Delta t) + c_4\frac{24}{\Delta t^4}\left(\frac{\Delta t^2}{2}\Delta\ddot{\mathbf{r}}\right),\\
\mathbf{r}^{\mathtt{V}}_{\mathtt{cor}}(t+\Delta t) &= \mathbf{r}^{\mathtt{V}}_{\mathtt{pre}}(t+\Delta t) + c_5\frac{120}{\Delta t^5}\left(\frac{\Delta t^2}{2}\Delta\ddot{\mathbf{r}}\right),
\end{aligned} \tag{3.43}$$

where the parameter c_i $(i = 0, 1, 2, 3, 4, 5)$ are given by

$$c_0 = \frac{3}{16}, \qquad c_1 = \frac{251}{360}, \qquad c_2 = 1, \qquad c_3 = \frac{11}{18}, \qquad c_4 = \frac{1}{6}, \qquad c_5 = \frac{1}{60}. \tag{3.44}$$

3.7.2 Newmark Method for FEM Time Integration

To integrate the (hyperbolic) differential equation in Eq. (B.9) for dynamic beam, several numerical integration schemes are available. Among them, Newmark method (see Newmark [76]) is widely used. Based on Newmark method, the equations of motion of the Euler-Bernoulli beam to be used in our 2D coupled DEM-FEM model are reviewed in this subsection. The displacement, velocity and acceleration of the

beam nodes at time step t_{n+1}, where $t_{n+1} = t_n + \Delta t$ are given by (see e.g., Reddy [86])

$$\begin{aligned} \mathbf{U}_{n+1} &= \mathbf{U}_n + \Delta t \ddot{\mathbf{U}}_n + \frac{1}{2}\Delta t^2 \ddot{\mathbf{U}}_{n+\gamma}, \\ \dot{\mathbf{U}}_{n+1} &= \dot{\mathbf{U}}_n + \Delta t \ddot{\mathbf{U}}_{n+\alpha}, \end{aligned} \tag{3.45}$$

where

$$\ddot{\mathbf{U}}_{n+\theta} = (1-\theta)\ddot{\mathbf{U}}_n + \theta \ddot{\mathbf{U}}_{n+1}. \tag{3.46}$$

The velocity and acceleration of the beam nodes at the time step t_{n+1} can be determined by substituting Eq. (3.46) into (3.45) as

$$\begin{aligned} \ddot{\mathbf{U}}_{n+1} &= a_3 \left(\mathbf{U}_{n+1} - \mathbf{U}_n\right) - a_4 \dot{\mathbf{U}}_n - a_5 \ddot{\mathbf{U}}_n, \\ \dot{\mathbf{U}}_{n+1} &= \dot{\mathbf{U}}_n + a_2 \ddot{\mathbf{U}}_n + a_1 \ddot{\mathbf{U}}_{n+1}, \end{aligned} \tag{3.47}$$

where the coefficient a_i $(i = 1, 2, 3, 4, 5)$ are given by

$$a_1 = \alpha \Delta t, \qquad a_2 = (1-\alpha)\Delta t, \qquad a_3 = \frac{2}{\gamma \Delta t^2}, \qquad a_4 = \frac{2}{\gamma \Delta t}, \qquad a_5 = \frac{1}{\gamma} - 1, \tag{3.48}$$

with α, γ denoting the parameters that determine the desired accuracy and stability of the integration scheme. Based on the parameters α and γ, the common integration schemes from the Newmark method are given in Table 3.2. The time step Δt used in a "stable" time integration scheme from the Newmark method is given by

$$\Delta t \leq \Delta t_{\mathtt{cri}} = \frac{1}{\sqrt{(\alpha - \gamma)\omega_{\mathtt{max}}^2/2}}, \tag{3.49}$$

where $\omega_{\mathtt{max}}$ is the maximum natural frequency of the system of the ODEs in Eq. (B.9). In our "BobKit" code, the Galerkin time integration scheme (stable) is implemented

Table 3.2: Time integration schemes obtained from the Newmark method for different values of the parameters.

	Scheme's name	Stability condition
$\alpha = 1/2, \gamma = 1/2$	Constant-average acceleration	Stable
$\alpha = 1/2, \gamma = 1/3$	Linear acceleration	Conditionally stable
$\alpha = 1/2, \gamma = 0$	Central difference	Conditionally stable
$\alpha = 3/2, \gamma = 8/5$	Galerkin	Stable
$\alpha = 3/2, \gamma = 2$	Backward difference	Stable

for FEM analysis part. Now, the displacement of the beam nodes can be obtained by substituting $\ddot{\mathbf{U}}_{n+1}$ in Eqs. (3.47) into (B.9). We get the system of algebraic equations

$$\tilde{\mathbf{K}}_{n+1}\mathbf{U}_{n+1} = \tilde{\mathbf{F}}_{n+1}, \tag{3.50}$$

where

$$\begin{aligned} \tilde{\mathbf{K}}_{n+1} &= \mathbf{K}_{n+1} + a_3\mathbf{M}_{n+1}, \\ \tilde{\mathbf{F}}_{n+1} &= \mathbf{F}_{n+1} + \mathbf{M}_{n+1}\left(a_3\mathbf{U}_n + a_4\dot{\mathbf{U}}_n + a_5\ddot{\mathbf{U}}_n\right). \end{aligned} \tag{3.51}$$

To calculate $\tilde{\mathbf{F}}$ from Eqs. (3.51), the displacement, velocity, and acceleration at the previous time step are required. At the initial condition, the displacement $\mathbf{U}_0$ and velocity $\dot{\mathbf{U}}_0$ are given for solving the second-order ODE in Eq. (B.9) where the acceleration can be computed from the differential equation as

$$\ddot{\mathbf{U}}_0 = \mathbf{M}^{-1}\left(\mathbf{F}_0 - \mathbf{K}\mathbf{U}_0\right). \tag{3.52}$$

To avoid matrix inversion of the mass matrix, the lumped mass matrix as discussed in Appendix B can be employed. After solving the linear system in Eq. (3.50), by

using Eqs. (3.51), for the displacement $\mathbf{U}$, the acceleration and velocity at the time step t_{n+1} are computed from Eqs. (3.47).

In summary, steps for solving the system of (hyperbolic) ODEs given in Eq. (B.9) using the Newmark method are as follows. For a given $\mathbf{K}$, $\mathbf{M}$, $\mathbf{F}$, $\mathbf{U}$, and $\dot{\mathbf{U}}$ at the initial time step, compute the acceleration at the initial condition from Eq. (3.52). For all time step t_{n+1}, calculate the displacement from Eq. (3.50) followed by the acceleration and velocity from Eqs. (3.47).

3.8 Description and Algorithm of the Coupled DEM-FEM

For a coupled 2D DEM-FEM simulation, two possible contact types called "full contact" and "partial contact" can occur during the contact between a discrete particle and a finite element. In full contact, as illustrated in Fig. 3.3b, the contact region between the particle and the beam element lies entirely within a single beam element, whereas the contact region touches more than one beam element in partial contact as shown in Fig. 3.7. The force model used for the discrete-element/finite-element interaction is the same as that used for the particle-particle interaction. However, the "radius" of an element is taken as infinity and thus the reduced radius R^* of this contacting pair is the same as that of the discrete element; that is $R^* = R$ where R

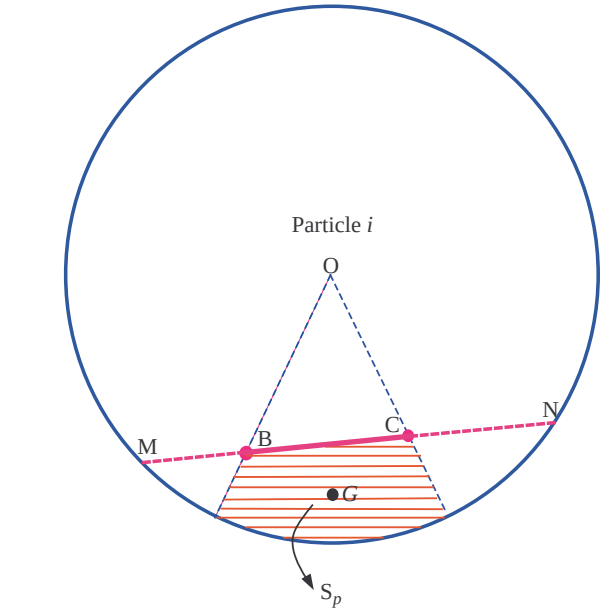

(a)

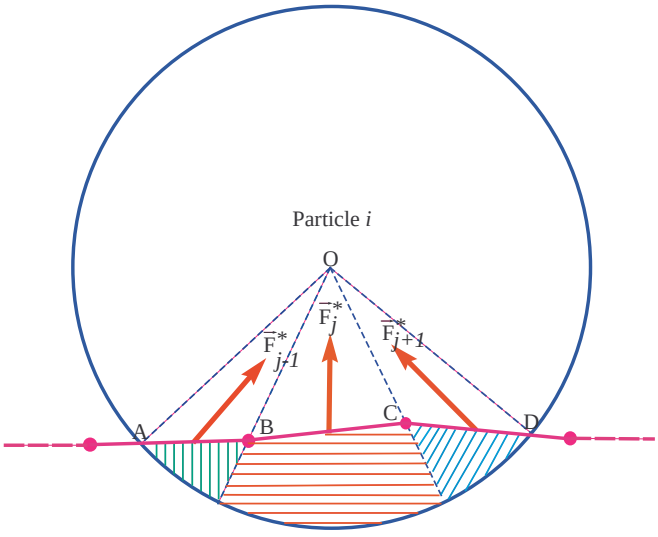

(b)

Figure 3.7: Partial contact: (a) Definition of scaling factor, (b) Normal force of three contact beam elements.

is the particle radius. The computational time step (Δt) to be used in the coupled DEM-FEM model is given by

$$\Delta t = \texttt{min}\left[\Delta t^{\texttt{FEM}}, \Delta t^{\texttt{DEM}}\right], \tag{3.53}$$

where $\Delta t^{\texttt{FEM}}$ and $\Delta t^{\texttt{DEM}}$ are the time step for FEM-beam and DEM-particle parts, respectively.

For full contact between particle and beam element, calculation of the normal contact force is similar to the wall case where the normal force is perpendicular to the beam element. However, calculation of the normal force for the partial contact is different in terms of the magnitude and direction as mentioned in Han et al. [36]. The procedure to compute the normal force are summarized for clarification below. First, calculate the partial contact force, for the j^{th} beam element, F_j^* by scaling the full contact force $\tilde{F}_j$ as

$$F_j^* = \alpha_{sf}\tilde{F}_j, \tag{3.54}$$

where $\alpha_{sf} \in (0, 1)$ is the scaling factor. Here, the full contact force $\tilde{F}_j$ is computed from the virtual full contact width by extending one or two ends of the segment, if necessary. The scaling factor can be determined from two different approaches:

1. Overlap area ratio: this approach was proposed by Petrinic [79] for combined FEM-DEM simulation of shot peening process. The scaling factor is determined

from

$$\alpha_{sf} = \frac{S_p}{S_f}, \tag{3.55}$$

where S_p and S_f are the area of the overlap region of partial and full contacts as shown in Fig. 3.7a. The overlap area of full contact is given as

$$S_f = 2R^2 \arctan\left(\frac{\xi}{a}\right) - a(R-\xi) \simeq \frac{4}{3}a\xi, \tag{3.56}$$

where R is the radius of the particle, and a denotes the half-contact width given by

$$a = \sqrt{\xi(2R-\xi)} \simeq \sqrt{2R\xi}. \tag{3.57}$$

The approximation is only for small deformation condition. Based on this approach, the calculation of the scaling factor requires a large number of numerical operations due to the computations of S_p, S_f, and the position of the centroid of the overlap area G as shown in Fig. 3.7a.

2. Contact width ratio: This approach was proposed by Han et al. [36] to improve the calculation efficiency. The scaling factor is determined from

$$\alpha_{sf} = \frac{w_p}{w_f}, \tag{3.58}$$

where $w_p = \|\overline{BC}\|$ and $w_f = \|\overline{MN}\|$ are the partial and full contact width as shown in Fig. 3.7a. In this approach, the contact point is assumed to be the middle point of the line segment as shown in Fig. 3.7a. Thus, the computational operations are significantly reduced.

The total normal contact force acting on the particle that contacts more than one beam element is given by:

$$\vec{F}_n = \sum_j F_j^* \vec{n}_j^*, \tag{3.59}$$

where $\vec{n}^*$ is the unit normal vector of the j^{th} beam element pointing from the contact point to the particle center as shown in Fig. 3.7b.

The description of the 2D coupled DEM-FEM simulation is summarized as follows: compute the contact velocity of the contacting pair using Eq. (3.6) if the particle overlap between particle and beam element(s) is detected followed by the computation of the contact forces. Once the contact force acting on a particle is computed, the reaction force on the beam element is added up into the system force vector acting on the beam. The finite element formulation for the Euler Bernoulli beam leads to the system of second-order (hyperbolic) differential equations (Eq. (B.9)) where **U** is the beam nodal displacement vector, **M** is the beam mass matrix, **K** is the beam stiffness matrix, and **F** is the force vector acting on the beam including the contact interactions with the discrete elements and the applied external force. We use the stable Galerkin time integration scheme (a particular type of Newmark family of methods) to approximate the new nodal beam displacement. This integration scheme reduces the differential equations (Eq. (B.9)) to a system of algebraic equations (Eq. (3.50)). It should be noted that the right-hand side vectors in Eqs. (3.51) include the initial and boundary conditions and the external loads applied to the beam. The

external loads are the contact interactions with the discrete elements and the applied load. At each time step, the nodal beam displacements are obtained by solving the system of linear equations, Eq. (3.50) together with (3.51). The accelerations and velocities for the beam are calculated from the Eqs. (3.47) with the coefficients in Eqs. (3.48). Note also that the system mass and stiffness matrices are constant during the simulation.

The algorithm, as illustrated in Fig. 3.8 and implemented in our 2D coupled DEM-FEM simulation, has the following steps: input initial data (particle and box coordinates; particle, box, and beam dimensions; material parameters; initial kinematic quantities e.g. position, velocity, acceleration, etc); for a given time step we detect all contacts between particles, particle-beam element, particle-rigid wall to compute contact forces acting on the particle-discrete elements and beam-finite elements; we compute the total forces for all particles followed by all external forces acting on the beam including the contact interaction with the discrete elements and the applied load; we then perform time integration using the 5^{th} order Gear's predictor-corrector time integration scheme for the motion of the discrete element particles and the Galerkin algorithm descried above for the motion of the beam-finite elements; the positions and velocities are updated to continue to the next time step.

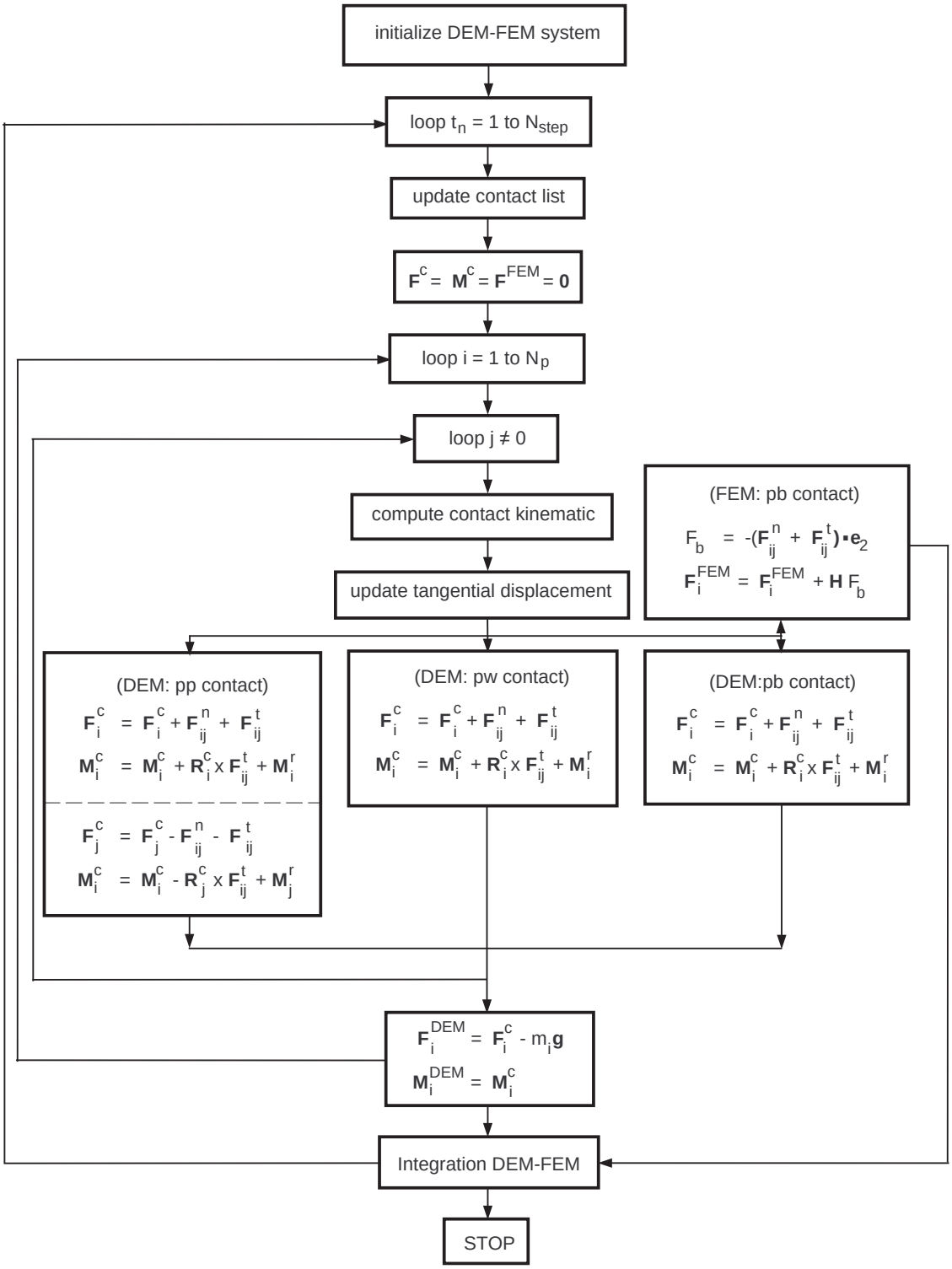

Figure 3.8: Algorithm of the 2D Coupled DEM-FEM Model.

Chapter 4

Derivation of the Effective Elastic Moduli and Particle-Size Dependence for Aggregates of Identical Elastic Disks

4.1 Introduction

Granular materials such as sand, gravel, and soil are envisioned as a collection of particle, which are highly discontinuous and nonhomogeneous with typically two phases consisting of particles for solids and gas for voids. The overall elastic behavior of a granular assembly may be modelled using the homogenization theory. This theory relates the macroscopic (global) behavior of the granular assembly to the microscopic (local) behavior of granular particle and voids by deducing the global constitutive law from the local contact laws. The global variables are (average) stress and strain while the local variables are contact force and contact relative displacement.

Based on homogenization theory, two basic hypotheses (approaches) can be employed: "kinematic (or Voigt) hypothesis" and "static hypothesis". For the kinematic hypothesis, the relative displacement at the contact point is defined as the function of the strain using localization operator and the stress is the function of the contact force using averaging operator. For static hypothesis, the contact force is defined as a function of stress using localization operator and the strain is the function of the contact relative displacement using averaging operator. For the local constitutive law in microscopic level, the theory of Hertz is usually used to relate the contact force and relative displacement of the contact particles. The generalized Hooke's law, for the global constitutive law, relates the stress and strain of the granular assembly in the macroscopic level. By applying the homogenization theory, the effective elastic moduli of the granular assembly are normally determined by using the kinematic (see Fig. 4.1 in the outer path) and static (see Fig. 4.1 in the inner path) hypotheses. The averaging operator allows the global variables to be defined from the local variables while the local variables are to be defined from the global variables using the localization operator (see e.g., Emeriault et al. [28]).

Most derivations of the elastic moduli of the granular assembly using the homogenization theory have been done for both 3D (sphere) and 2D (disk) of equal-sized particles. The elastic constants of the granular assembly for the spherical particles were derived for the regular packing (see e.g., Deresiewicz [21], Duffy and Mindlin [27]) and

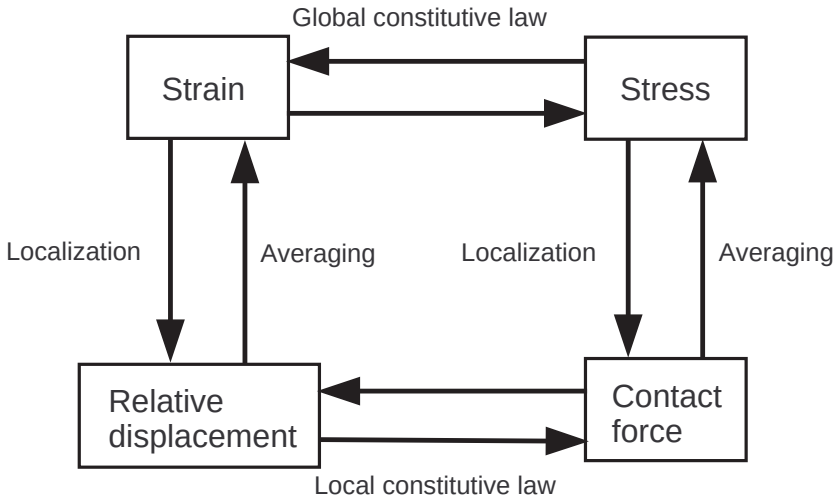

Figure 4.1: Definition of the different operators of localization and averaging. From Emeriault et al. [28].

random packing (see e.g., Chang et al. [16], Digby [22], Liao et al. [63], Walton [102]). For 2D particles (disks), the closed-form expression of the effective elastic constants of randomly packed particles can be found from e.g., Bathurst and Rothenburg [5] and Chang and Liao [15].

In this chapter, the analytical solution of effective elastic moduli of a 2D similar granular assembly (disks) is first derived in terms of stiffness of two contacting particles based on the "best-fit hypothesis", which was proposed by Liao et al. [64] (see also Liao et al. [63]). This hypothesis can be considered as the modified kinematic hypothesis where more realistic relation for the relative displacement field in the granular assembly is expected by postulating that the mean displacement is the best fit of the actual displacement field. For the closed-form solution, the derivation

is limited to isotropically distributed and equal-size particles with no slip. Using the homogenization theory based on the best-fit hypothesis, the procedure to derive the effective elastic moduli of a 2D granular assembly in terms of contact stiffness are as follows: starting with kinematics and contact law of two contacting particles, the micro-macro relationships consisting of contact displacement-strain and contact force-stress relationships are derived. Then, the stress-strain relationship at macroscopic level is applied to obtain the elastic moduli of the granular assembly in terms of the stiffness of the contacting particles. Next, based on the derived elastic moduli in combination with Hertzian contact of two contacting particles, the effective Young's modulus of 2D similar granular assembly is derived in term of particle radius. Finally, the effective Young's modulus of the granular assembly is used to derive the particle-size dependence (PSD) of bending resonance of the 2D granular layer. For simplicity, the index notation is used throughout the derivation.

4.2 Effective Elastic Moduli for Aggregates of Identical Elastic Disks Derived from the Best-Fit Hypothesis

4.2.1 Micromechanics

Kinematics of Two Particles in Contact

The contact relative displacement (or particle deformation) Δ_i^c between particles p and q due to the displacement of the particle centers and the rotation of particles is given by

$$\Delta_i^c = \Delta_i^{pq} = u_i^q - u_i^p = \left(U_i^q + e_{ji}\omega^q R_j^{qc}\right) - \left(U_i^p + e_{ji}\omega^p R_j^{pc}\right), \quad i,j = 1,2 \tag{4.1}$$

where u_i^p is the displacement of particle p, U_i^p is the displacement of the center of the particle p and ω^p is its rotation (positive in counter-clockwise direction), e_{ji} is the two-dimensional permutation tensor, R_j^{pc} denotes the vector from the center of particle p to the contact point c (see Fig. 4.2a). Recall that the normal Δ^n and tangential Δ^t components of the contact relative displacement Δ_i^c used in the contact force model (in section 3.4) are assigned as ξ and ζ, respectively.

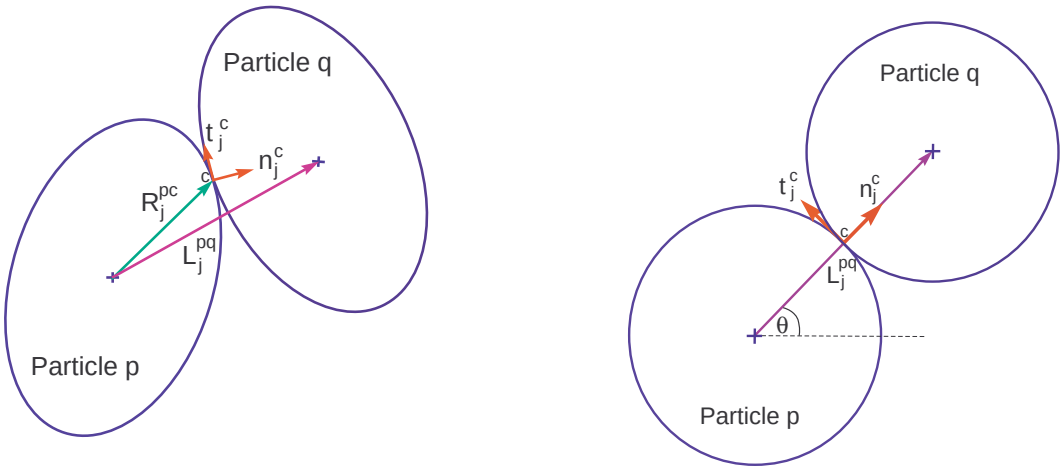

(a) (b)

Figure 4.2: (a) Contact geometry of particles in contact. (b) Contact orientation θ, local coordinate system in normal and tangential components $(\mathbf{n}^c, \mathbf{t}^c)$, and branch vector $\mathbf{L}^c$ of two identical disks p and q in contact.

Contact Law

For an elastic behavior of two particles in contact, a general expression for the contact constitutive relation between inter-particle force F_j^c and inter-particle deformation (contact relative displacement) Δ_i^c is given by

$$\Delta_i^c = S_{ij}^c F_j^c, \tag{4.2}$$

where S_{ij}^c is the inter-particle contact stiffness tensor. The stiffness tensor can be expressed in terms of the normal and tangential stiffness (K_n and K_t) as

$$S_{ij}^c = \frac{1}{K_n} n_i^c n_j^c + \frac{1}{K_t} t_i^c t_j^c, \tag{4.3}$$

with $\mathbf{n}^c$ and $\mathbf{t}^c$ denoting the (local) unit normal and tangential vectors at the contact point. For equal particle sizes (see Fig. 4.2b), two unit vectors, in term of the contact

orientation θ (positive in counter-clockwise direction) from the horizontal axis, are given by

$$\mathbf{n}^c = (\cos\theta, \sin\theta)\,, \qquad \mathbf{t}^c = (-\sin\theta, \cos\theta)\,. \tag{4.4}$$

Note that the normal and tangential stiffness (K_n and K_t) implemented in our BobKit code for both linear (Hookean) and nonlinear (Hertzian) contact models are given in subsection 3.4.1 and 3.4.2.

4.2.2 Micro-Macro Relationships

Contact Displacement-Strain Relationships

For kinematic homogenization assumption, the relative displacement at the contact point is defined as a function of mean strain of the granular assembly where the uniform strain (for bonded particles) is frequently assumed. The displacement of the center of a particle (i.e., particle p) in the assembly is given as (see e.g., Kruyt and Rothenburg [53])

$$U_i^p = u_{i,j} r_j^p, \tag{4.5}$$

with $u_{i,j}$ being the displacement gradient and r_j^p denoting the position vector of the center of particle p. Applying Eq. (4.5) to Eq. (4.1), the corresponding contact relative displacement becomes

$$\Delta_i^c = u_{i,j}\left(r_j^q - r_j^p\right) - e_{ji}\omega_j\left(R_j^{pc} - R_j^{qc}\right). \tag{4.6}$$

Here, the rigid body ration ia assumed (i.e., $\omega^p = \omega^q = \omega$). For convenience the branch vector L_j^c, which represents the vector from the center of particle p to the center of the contacting particle q as shown in Fig. 4.2, is used in the relative displacement and defined as

$$L_j^c = L_j^{pq} = r_j^q - r_j^p = R_j^{pc} - R_j^{qc}. \tag{4.7}$$

Note that the branch vector for two identical disks of radii R becomes $L_j^c = 2Rn_j^c$ with n_j^c being the unit normal vector (see Fig. 4.2b). As a result, the relative displacement between contacting particles based on kinematic hypothesis (or uniform strain assumption) becomes (see e.g., Agnolin and Kruyt [1], Kruyt and Rothenburg [53])

$$\Delta_i^c = \epsilon_{ij} L_j^c, \qquad i, j = 1, 2 \tag{4.8}$$

Note that, by using the skew-symmetric part of strain $e_{ji}\omega_j = (u_{i,j} - u_{j,i})/2$, the term $u_{i,j} - e_{ji}\omega_j$ is equal to the symmetric strain $\epsilon_{ij} = (u_{i,j} + u_{j,i})/2$.

As proposed by Liao et al. [64] (see also Liao et al. [63]) the best-fit hypothesis is considered as the modified kinematic hypothesis. For this hypothesis the (actual) relative displacement of two contacting particles accounts for both affine and non-affine deformations. As a result, the contact relative displacement can be expressed as

$$\Delta_i^c = \epsilon_{ij} L_j^c + E_i^c, \tag{4.9}$$

where $\epsilon_{ij}L_j^c$ is the affine displacement contribution from the uniform strain assumption (see Eq. (4.8)), E_i^c is the non-affine displacement contribution (displacement fluctuation on the mean filed). Applying the least-squares method, the difference in contact relative displacements over number of contacts within the granular assembly can be expressed by the scalar value e as

$$e = \sum_{c=1}^{N} \left(E_i^c\right)^2 = \sum_{c=1}^{N} \left(\Delta_i^c - \epsilon_{ij}L_j^c\right)^2, \tag{4.10}$$

where N is the total number of contacts in the assembly. Minimizing e with respect to the the strain field of the assembly ϵ_{mn}, we need to solve:

$$\frac{\partial e}{\partial \epsilon_{mn}} = 0. \tag{4.11}$$

This leads to the relation

$$\sum_{c=1}^{N} \left(\Delta_i^c - \epsilon_{ij}L_j^c\right) \frac{\partial}{\partial \epsilon_{mn}} \left(\Delta_i^c - \epsilon_{ij}L_j^c\right) = 0, \tag{4.12}$$

yielding the average strain of the assembly as (e.g., Liao et al. [63])

$$\epsilon_{ij} = \frac{1}{V} \sum_{c=1}^{N} \Delta_i^c L_n^c A_{jn}, \tag{4.13}$$

with A_{jn} being the fabric tensor

$$A_{jn} = \left[\frac{1}{V} \sum_{c=1}^{N} L_j^c L_n^c\right]^{-1}. \tag{4.14}$$

As seen in Eq. (4.14), the fabric tensor is symmetry. It relates to branch vector (or vector connecting two contact particles, see Fig. 4.2), and structure of the assembly (see e.g., Liao et al. [63], Madadi et al. [66]).

Contact Force-Stress Relationships

Based on the principle of virtual work, the incremental complimentary work δW of the granular assembly with volume V (thin disk with small thickness b), evaluated via the average stress σ_{ij} and the incremental average strain ϵ_{ij}, may also be evaluated via the contact force F_i^c and incremental contact relative displacement $\delta\Delta_i^c$ of all contacting particles within the granular assembly as

$$\delta W = V\sigma_{ij}\delta\epsilon_{ij} = \sum_{c=1}^{N} F_i^c \delta\Delta_i^c. \tag{4.15}$$

The relationship between the average stress of the assembly σ_{ij} and the contact force between particles F_i^c is obtained by substituting Eq. (4.13) into Eq. (4.15). We get (see e.g., Liao et al. [63])

$$F_i^c = \sigma_{ij} L_n^c A_{jn}. \tag{4.16}$$

4.2.3 Macromechanics

To derive the elastic modulus of the granular assembly in term of the stiffness (K_n and K_t) of the contacting particles, the constitutive equation that relates the stress σ_{ij} and strain ϵ_{ij} of the packing in term of the compliance tensor S_{ijkl} is formulated. For a linear elastic material the constitutive equation can be expresses as

$$\epsilon_{ij} = S_{ijkl}\sigma_{kl}, \qquad i,j,k,l = 1,2 \tag{4.17}$$

By combining Eq. (4.2), (4.3), (4.13), (4.16) and (4.17), the derived stiffness tensor becomes

$$\begin{aligned} S_{ijkl} &= \frac{1}{V}\sum_{c=1}^{N} S_{ik}^{c} A_{jk} L_{k}^{c} A_{lm} L_{m}^{c} \\ &= \frac{1}{V}\sum_{c=1}^{N}\left(\frac{1}{K_n} n_i^c n_k^c A_{jk} L_k^c A_{lm} L_m^c + \frac{1}{K_t} t_i^c t_k^c A_{jk} L_k^c A_{lm} L_m^c\right). \end{aligned} \tag{4.18}$$

For analytical manipulation, it is convenience to transform a summation of over all contacts to an integral form by using the definitions of the contact distribution function $\chi(\theta)$ and the group average $\bar{\varphi}(\theta)$. The transformation can be expressed as (see Bathurst and Rothenburg [5] for detail)

$$\frac{1}{V}\sum_{c=1}^{N}\varphi^{c} = \frac{N}{V}\int_{0}^{2\pi}\chi(\theta)\bar{\varphi}(\theta)d\theta, \tag{4.19}$$

where the contact distribution function $\chi(\theta) = 1/2\pi$ for isotropic assembly of packing. By applying the transformation in Eq. (4.19) to Eq. (4.18), the compliance tensor of the packing for identical disks of radii R that the branch vector can be expressed as $L_i^c = 2Rn_i^c$ with n_i^c being the unit normal vector (see Fig. 4.2b) is given by

$$S_{ijkl} = \frac{V}{2\pi R^2 N}\int_{0}^{2\pi}\left(\frac{1}{K_n} n_i^c(\theta) n_j^c(\theta) n_k^c(\theta) n_l^c(\theta) + \frac{1}{K_t} t_i^c(\theta) n_j^c(\theta) t_k^c(\theta) n_l^c(\theta)\right) d\theta. \tag{4.20}$$

The fabric tensor in Eq. (4.14) for identical particles of radii R, by using transformation expression (Eq. (4.19)), becomes $A_{ij} = \left[\frac{2R^2N}{V}\delta_{ij}\right]^{-1}$ with δ_{ij} being the Kronecker delta symbol. Under assumption of plane stress problem, the stress-strain relation

(Eq. (4.17)) of an isotropic assembly for identical disks of radii R can be expressed in matrix form as

$$\begin{bmatrix} \epsilon_{11} \\ \epsilon_{22} \\ 2\epsilon_{12} \end{bmatrix} = \begin{bmatrix} S_{1111} & S_{1122} & S_{1112} \\ S_{2211} & S_{2222} & S_{2212} \\ S_{1211} & S_{1222} & S_{1212} \end{bmatrix} \begin{bmatrix} \sigma_{11} \\ \sigma_{22} \\ \sigma_{12} \end{bmatrix}, \tag{4.21}$$

where

$$\begin{aligned} S_{1111} &= S_{2222} = \frac{V}{8R^2N}\left(\frac{3}{K_n} + \frac{1}{K_t}\right), \\ S_{1122} &= S_{2211} = \frac{V}{8R^2N}\left(\frac{1}{K_n} - \frac{1}{K_t}\right), \\ S_{1212} &= \frac{V}{8R^2N}\left(\frac{1}{K_n} + \frac{3}{K_t}\right), \\ S_{1112} &= S_{1211} = S_{1222} = S_{2212} = 0. \end{aligned} \tag{4.22}$$

Note that all components of the compliance tensor $S_{ijkl}, i, j, k, l = 1, 2$ in terms of the inter-particle contact stiffness (K_n, K_t) can be easily calculated from the unit normal and tangential vectors (Eq. (4.4)). Now, the effective elastic constants of the assembly are obtained by comparing to the classical elasticity of an isotropic material, which the stress-strain relation can be written as

$$\epsilon_{ij} = -\frac{\bar{\nu}}{\bar{E}}\sigma_{kk}\delta_{ij} + \frac{(1+\bar{\nu})}{\bar{E}}\sigma_{ij}, \qquad i, j, k = 1, 2 \tag{4.23}$$

or in matrix form,

$$\begin{bmatrix} \epsilon_{11} \\ \epsilon_{22} \\ 2\epsilon_{12} \end{bmatrix} = \frac{1}{\bar{E}} \begin{bmatrix} 1 & -\bar{\nu} & 0 \\ -\bar{\nu} & 1 & 0 \\ 0 & 0 & 2(1+\bar{\nu}) \end{bmatrix} \begin{bmatrix} \sigma_{11} \\ \sigma_{22} \\ \sigma_{12} \end{bmatrix}, \tag{4.24}$$

with $\bar{E}, \bar{G}, \bar{\nu}$ denoting the Young's modulus, shear modulus, and Poisson's ratio of the elastically isotropic material, respectively. By comparing the components of the

compliance tensor in Eq. (4.21), (4.22) with Eq. (4.24), the effective elastic constants of the assembly for identical disks of radii R based on the best-fit hypothesis become

$$\begin{aligned} \bar{\nu} &= \frac{1-\lambda}{1+3\lambda}, \\ \bar{E} &= \frac{8R^2NK_n}{V}\left(\frac{\lambda}{1+3\lambda}\right), \\ \bar{G} &= \frac{2R^2NK_n}{V}\left(\frac{\lambda}{1+\lambda}\right), \end{aligned} \tag{4.25}$$

with $\lambda = K_t/K_n$ being the ratio of tangential to normal contact stiffness (stiffness ratio). It is interesting to compare the effective constants of the 2D granular assembly obtained by the best-fit hypothesis with existing kinematic and static hypotheses. Chang and Liao [15] derived the effective Poisson's ratio $\bar{\nu}$, Young's modulus $\bar{E}$, and shear modulus $\bar{G}$ for aggregates of identical elastic 2D particles (disks) with radii R as follows:

Based on the kinematic hypothesis (see Eq. (56) on page S204)

$$\begin{aligned} \bar{\nu}^{\texttt{kinematic}} &= \frac{1-\lambda}{3+\lambda}, \\ \bar{E}^{\texttt{kinematic}} &= \frac{4R^2NK_n}{V}\left(\frac{1+\lambda}{3+\lambda}\right), \\ \bar{G}^{\texttt{kinematic}} &= \frac{R^2NK_n}{2V}\left(1+\lambda\right). \end{aligned} \tag{4.26}$$

Based on the static hypothesis (see Eq. (57) on page S204)

$$\begin{aligned} \bar{\nu}^{\texttt{static}} &= \frac{1-\lambda}{1+3\lambda}, \\ \bar{E}^{\texttt{static}} &= \frac{8R^2NK_n}{V}\left(\frac{\lambda}{1+3\lambda}\right), \\ \bar{G}^{\texttt{static}} &= \frac{2R^2NK_n}{V}\left(\frac{\lambda}{1+\lambda}\right). \end{aligned} \tag{4.27}$$

At this point, we only consider the effective elastic moduli consisting of the Young's modulus $\bar{E}$ and shear modulus $\bar{G}$ of the granular assembly. For comparison, the effective elastic moduli of granular assembly for identical disks based on existing (kinematic and static) and best-fit hypotheses are plotted in Fig. 4.3. Obviously, the elastic moduli based on the static hypothesis are the same as that of the best-fit hypothesis (see Eqs. (4.25), (4.27)) and their lower values (lower bound) are estimated. In contrast, the upper estimates (upper bound) of the elastic moduli are obtained from the kinematic hypothesis. In Fig. 4.3, the elastic moduli increase with increasing in contact stiffness ratio. It implies that a granular layer with bonded contacts resists more compressive (see Fig. 4.3a) and shearing (see Fig. 4.3b) loads. In addition, granular layer with the same value of stiffness ratio resists more compressive than shearing (see Fig. 4.3a, b), i.e. $\bar{E}$ is higher than $\bar{G}$. According to Chang and Liao [15] study, the lower estimates of the elastic moduli derived based on the static hypothesis quite agree with the simulation results. As a result, the effective elastic Young's modulus of the granular assembly from our derivation based on the best-fit hypothesis is confirmed with the results obtained from the static assumption. Moreover, our derivation is supposed to compare with our simulation results from the couple DEM-FEM model for the quasi-static analysis in section 5.4.

It is useful to relate the ratio N/V, denoting contact density, given in Eqs. (4.25) to the packing property of the assembly as follows. The number of contacts per

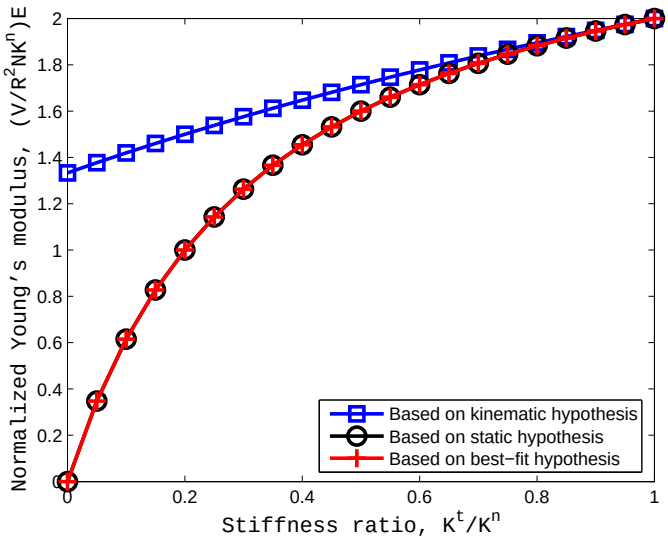

(a)

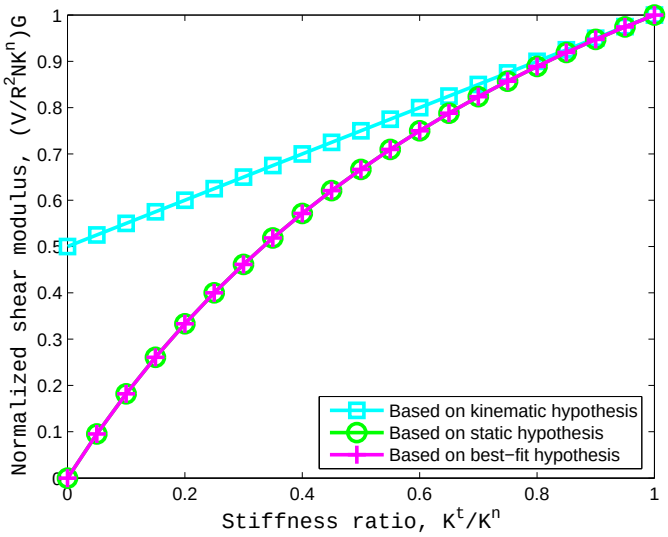

(b)

Figure 4.3: Upper and lower estimates of normalized elastic moduli: (a) Young's modulus $\bar{E}$, (b) shear modulus $\bar{G}$, with various stiffness ratio K_t/K_n values for aggregates of identical disks using homogenization theory. The elastic moduli based on the existing (kinematic and static) hypotheses are derived by Chang and Liao [15] whereas the best-fit hypothesis proposed by Liao et al. [64] is used for our derivation.

particle (i.e. coordination number of the particle) is introduced. Thus, the average coordination number K of the granular assembly is defined as (see e.g., Bathurst and Rothenburg [5])

$$K = \frac{N}{N_p}, \tag{4.28}$$

where N is the total number of contacts within the granular assembly, N_p is the total number of particles. Also, the packing fraction ϕ of the granular assembly is given as

$$\phi = \frac{V_p}{V} = \frac{\pi R^2 b N_p}{V}, \tag{4.29}$$

with V_p being the total volume of the particles, b denoting the thickness of the 2D particles (disks) of radii R. Combining Eq. (4.28) and (4.29) yields

$$\frac{N}{V} = \frac{K\phi}{\pi R^2 b}. \tag{4.30}$$

By substituting Eq. (4.30) into Eqs. (4.25), the effective elastic constants of the assembly for aggregates of identical disks of radii R with thickness b can be expressed in term of the contact stiffness (K_n, K_t) as

$$\begin{aligned} \bar{\nu} &= \frac{K_n - K_t}{K_n + 3K_t}, \\ \bar{E} &= \frac{8K\phi}{\pi b}\left(\frac{K_n K_t}{K_n + 3K_t}\right), \\ \bar{G} &= \frac{2K\phi}{\pi b}\left(\frac{K_n K_t}{K_n + K_t}\right). \end{aligned} \tag{4.31}$$

4.3 Effective Young's Modulus of the Granular Assembly

In this section, the effective Young's modulus $\bar{E}$ of a granular assembly is derived in term of particle radius R of similar 2D particles (disks). We follow the same procedure as Kang (see Kang [46], Kang et al. [47]) where the effective Young's modulus in term of the particle radius for a random packing of identical elastic spherical particles is derived. Based on the Hertzian contact of an elastic disk, the effective Young's modulus $\bar{E}$ of a granular assembly in Eqs. (4.31) derived from the best-fit hypothesis can be expressed in term of the contact width a as

$$\bar{E} = \frac{16K\phi}{\pi b}\frac{Ea}{(1+\nu)(2-\nu)}. \tag{4.32}$$

Note that the contact stiffness term inside parenthesis in Eqs. (4.31) can be approximated as

$$\frac{K_n K_t}{K_n + 3K_t} = \frac{2\pi Ea}{\pi(1+\nu)(2-\nu) + 6a\ln\left[4R/\xi\exp\left(1+\nu\right)\right]} \simeq \frac{2Ea}{(1+\nu)(2-\nu)}, \tag{4.33}$$

with the stiffness of a contacting particle (K_n and K_t) giving in Eq. (3.21) and (3.23). Also, small contact width $a = \sqrt{\xi R}$ (see Eq. (A.3)) is reasonably assumed such that $\pi(1+\nu)(2-\nu) \gg 6a\ln\left[4R/\xi\exp\left(1+\nu\right)\right]$. Recall that the contact width a between two contacting disks with finite thickness is given by (see e.g., Johnson [45])

$$a = \left(\frac{4PR^*}{\pi E^*}\right)^{1/2}, \tag{4.34}$$

where $P = F^n/b$ is the applied normal force F^n per unit thickness b of the disk. The reduced radius R^* and reduced Young's modulus E^* are given as

$$\begin{aligned} \frac{1}{R^*} &= \frac{1}{R_1} + \frac{1}{R_2}, \\ \frac{1}{E^*} &= \frac{1-\nu_1^2}{E_1} + \frac{1-\nu_2^2}{E_2}, \end{aligned} \tag{4.35}$$

with E_i, ν_i, R_i $(i = 1, 2)$ are the Young's modulus, Poisson's ratio, and radius of particles, respectively. Similar to Kang [46], we assume that the contact force F^n on a given particle contact is equal to the total weight of the particles above a given particle divided by the number of contacts over which the force is distributed. Here, $F^n = F^n(y) = \pi\rho g b R^2(h-y)/K\phi y$ with y being the depth in the granular layer that varies from 0 to h, ρ defining the mass density of the particle, and g being the gravitational acceleration. Hence, the average contact width can be expressed as

$$< a >= \left\langle \left(\frac{4F^n(y)R^*}{\pi b E^*} \right)^{1/2} \right\rangle, \tag{4.36}$$

where the ensemble average $\langle \cdot \rangle$ can be defined as an integral through the granular layer. Accordingly, the average contact width for aggregates of similar elastic disks becomes

$$< a >= \left[\frac{4\rho g(1-\nu^2)}{EK\phi} \right]^{1/2} R^{3/2} Q(y), \tag{4.37}$$

with

$$Q(y) = \frac{1}{h} \int_R^h \left[\frac{h-y}{y} \right]^{1/2} dy. \tag{4.38}$$

By substituting the average contact width (Eq. (4.37)) into Eq. (4.32), the effective Young's modulus of the granular assembly for identical disks becomes

$$\bar{E} = \left[\frac{1,024\rho g E K \phi(1-\nu)}{\pi^2 b^2 (1+\nu)(2-\nu)^2}\right]^{1/2} R^{3/2} Q(y). \tag{4.39}$$

4.4 Particle-Size Dependence (PSD) of Bending Resonance of the Granular Layer

Due to no experimental results of 2D-particles loaded beam under small dynamic vibration, we use an available 3D experimental results of a glass bead loaded plate induced by an acoustic wave from Kang [46] as shown in Fig. 4.4 to explain the resonant behavior of the system. If that the 2D experiment exists, then the resonant behavior is expected to be, at least, qualitatively similar to the 3D case because it is about small vibration of granular layer loaded elastic support system. In Fig. 4.4, the normalized frequency is defined as the frequency of the loaded plate (granular layer loaded on top of elastic support) divided by the frequency of the unloaded plate (elastic support alone), and the mass ratio is defined as mass of glass beads (granular layer) divided by mass of the plate (elastic support). As seen in Fig. 4.4, the first resonant frequency first decreases (Region A) until reaching the minimum and then increases (Region B). Observe that the analytical solution of a clamped plate (shown as solid line in Fig. 4.4) falls into the Region A as well. It can be seen that there is no

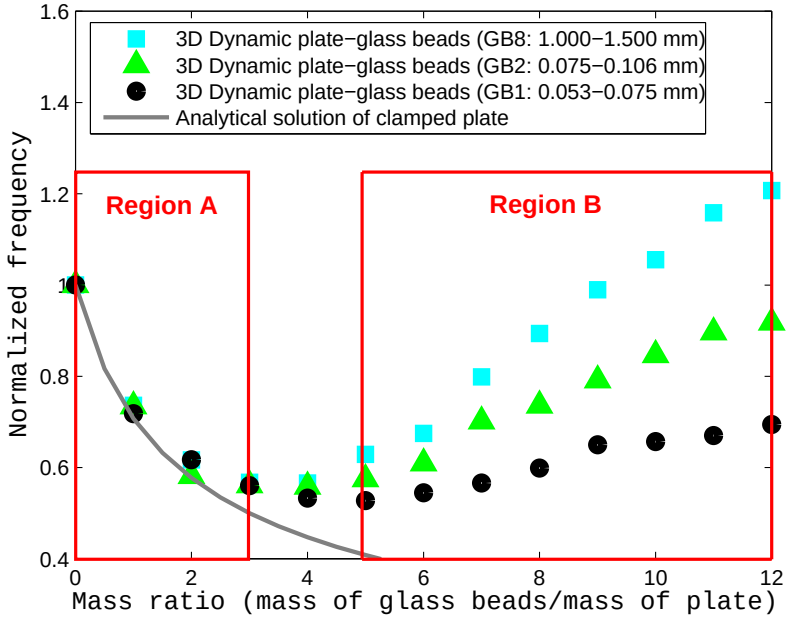

Figure 4.4: The first resonant frequency of a glass bead loaded plate obtained from 3D dynamic experiments by Kang [46] for three particle sizes of GB1: 0.053-0.075 mm, GB2: 0.075-0.106 and GB8: 1.0-1.5 mm for comparison with our coupled 2D quasi-static and dynamic DEM-FEM simulations. The particle sizes is selected because the separation in frequency curves is obviously distinct. In Region A, no particle size effect is observed as the solid line obtained from the analytical solution of a clamped plate. In Region B; however, particle size becomes an important factor in shifting/changing resonant frequencies.

particle size effect on the resonant behavior in Region A (mass ratio < 3). However, in region B (mass ratio ≥ 5), the size of particles is important in increasing of the resonant frequency. Observe that the system with larger particles leads to stiffer layer (see Fig. 4.4). More discussion can be founded in Kang (see Kang [46], Kang et al. [47]).

The analytical model of a 2D particles loaded beam (or simply beam-layer) system

under free vibration for both regions A and B as described above is developed with the same procedure as in spherical particles loaded plate by Kang (see Kang [46], Kang et al. [47]). For 2D analysis, the first bending frequency of the Euler-Bernoulli's beam with clamped-clamped ends is given by (see e.g., Kelly [48])

$$\omega_1 = \left(\frac{\lambda_1}{L_b}\right)^2 \sqrt{\frac{D_b}{\rho_b A_b}} = \left(\frac{\lambda_1}{L_b}\right)^2 \sqrt{\frac{E_b I_b}{\rho_b A_b}}, \tag{4.40}$$

where $\lambda_1 = 4.730$ is the eigenvalue associated with the first bending mode of a clamped beam, $D_b = E_b I_b$ denotes the bending stiffness, E_b is the Young's modulus, ρ_b is the mass density, A_b is the cross-sectional area, $I_b = bh_b^3/12$ is the moment of inertia of the cross-sectional area, h_b is the thickness, b is the width (in the third dimension and being the same as the thickness of particles), and L_b is the length of the beam, respectively.

Region A is a "mass dominant" regime in which the combined system (2D particles loaded on top of an elastic beam, or simply beam-layer system) behaves as a beam loaded by added mass. It can be assumed that the mass of particles is dominant in this regime. As a result, the first bending resonance in region A can be written as

$$\omega_A = \left(\frac{\lambda_1}{\bar{L}}\right)^2 \sqrt{\frac{\bar{D}}{\bar{\rho}\bar{A}}}. \tag{4.41}$$

Here $\bar{D}$, $\bar{\rho}, \bar{A}$ and $\bar{L}$ are the effective bending stiffness, density, cross-sectional area, and length of the beam-layer system, respectively. Note that the length of the beam is the same as that of the beam-layer system ($\bar{L} = L_b$). The effective density $\bar{\rho}$ is

defined as the average density of the beam-layer system

$$\bar{\rho} = \frac{h_b}{\bar{h}}\rho_b(1+M), \tag{4.42}$$

where $M = m_p/m_b$ is the mass ratio (mass of particle layer normalized by mass of the beam) with m_p, m_b being the mass of particle layer and beam, respectively. Note that the the effective density of the combined system given in Eq. (4.42) is obtained from $\bar{\rho}\bar{V} = m_b + m_p$ where $\bar{\rho}\bar{V}$ represents the total mass of the beam-layer system. $\bar{V} = bL_b\bar{h}$ is the effective volume where $\bar{h} = h_b + h_p$ is the effective thickness of the combined system with h_p being the thickness of particle layer. Thus, the normalized bending frequency $\tilde{\omega}$ in region A becomes

$$\tilde{\omega} = \frac{\omega_A}{\omega_1} = \sqrt{\frac{1}{M+1}}, \tag{4.43}$$

with $\bar{D} = D_b$ due to no difference in bending stiffness obtained from the analytical solution and the beam-layer system in region A (see Fig. 4.4). In region B ("bending stiffness" regime), if the thickness of the particle layer is dominant in shifting/changing resonant frequency, then the beam will have a minor influence on the frequency response of the beam-layer system as shown in Fig. 4.4. The effective thickness of the beam-layer in term of mass ratio M is obtained from $\bar{V} = V_b + V_p = m_b/\rho_b + m_p/\rho_p$ with V_p, ρ_p being the volume and density of particle layer, respectively. The relation leads to the effective thickness $\bar{h}$ of the beam-layer

system as

$$\bar{h} = h_b \left(1 + \frac{\rho_b}{\rho_p} M\right). \tag{4.44}$$

The bending resonance of the beam-layer system in region B is given by

$$\omega_B = \left(\frac{\lambda_1}{L_b}\right)^2 \sqrt{\frac{\bar{E}\bar{I}}{\bar{\rho}\bar{A}}} = \left(\frac{\lambda_1}{L_b}\right)^2 \sqrt{\frac{\bar{E}h_b^2 \left(1 + \frac{\rho_b}{\rho_p} M\right)^3}{12\rho_b \left(1 + M\right)}}, \tag{4.45}$$

with $\bar{E}, \bar{I}$, and $\bar{A}$ denoting the effective Young's modulus, moment of inertia of the cross-sectional area, cross-sectional area of the beam-layer system, respectively. Thus, the normalized resonant frequency of the beam-layer system in region B is given by

$$\tilde{\omega} = \frac{\omega_B}{\omega_1} = \sqrt{\frac{\bar{E}\left(1 + \frac{\rho_b}{\rho_p} M\right)^3}{E_b \left(1 + M\right)}} \propto \sqrt{\frac{\left(1 + \frac{\rho_b}{\rho_p} M\right)^3}{\left(1 + M\right)}}. \tag{4.46}$$

From the Eq. (4.46), for sufficiently large M, the resonant frequency in region B is expected to linearly depend on M. This implies that the resonant frequency increases as increasing in thickness of the particle layer with minor effect in the elastic support beam. From the 3D experiments as shown in Fig. 4.4, the bending frequency becomes higher for the layer of bigger particles. As a result, the dependence of the slope of normalized frequency $\tilde{\omega}$ on the particle size in region B is studied next.

As mentioned earlier, the dependence of the slope $\tilde{\omega}$ on the particle size in region B is discussed here. The linear dependence of $\tilde{\omega}$ on M is expected for relatively large M ($M > 5$) (or thick particle layer) (see Fig. 4.4). In region B, it is clear that the slope of the normalized frequencies depends on the particle size (see Fig. 4.4) as well

as other parameters such as contact interfaces, stiffness of particles, etc. However, the influence of particle size in the slope of normalized frequency $\tilde{\omega}$ is considered here. The slope of each $\tilde{\omega} - M$ curve in region B defined as $\sigma = \partial\tilde{\omega}/\partial M$ is extracted. In Eq. (4.43) and Eq. (4.46), the general function to fit over the entire $\tilde{\omega} - M$ curves is given by

$$\tilde{\omega} = \sqrt{\frac{A}{M+1} + BM + CM^2}, \tag{4.47}$$

where A, B, C are the fit coefficients. This function is first introduced by Korman and Sabatier [51] and later used in Kang [46] and Kang et al. [47] for 3D experiments for bending vibration of granular layer loaded on top of elastic plate induced by an acoustic wave. From Eq. (4.47), it is obvious that the dependent parameter $\sigma = \sqrt{C}$ for the relatively large value of M (in region B) and its value is examined. To obtain the dependence of σ on the particle radius R in region B, the power-law dependence is introduced and given by (see e.g., Korman and Sabatier [51], Kang [46], Kang et al. [47])

$$\sigma(R) = \alpha R^{\beta}, \tag{4.48}$$

where α, β are the fit parameters obtained from the method of least-squares. In a $\ln(\sigma) - \ln(R)$ plot, the β value represents the slope of the curve in region B.

The value of β of an aggregate of spherical particles is derived by Kang (see Kang [46], Kang et al. [47]) and ends up with $\beta = 1/6 (= 0.167)$; that is, the dependence of σ is $R^{1/6}$. Here, the analytical result is based on the effective medium theories

and limited to a random packing of identical elastic spherical particles. Many researchers, for example, Digby [22], Walton [102] and more recently Jenkins et al. [43], use the effective medium theories to predict the effective elastic moduli of an aggregate of spherical particles under the hydrostatic pressure. However, from the 3D dynamic experiments of granular materials loaded plate induced by an acoustic wave, the dependence of σ is $R^{0.305}$ for sand, and $R^{0.330}$ for glass bead (see Kang [46], Kang et al. [47]). The discrepancy of the dependence of σ on R obtained from analytical prediction and experiments is attempted to explain in Kang et al. [47]. He pointed out that the effective medium theories for granular system may not be able to estimate the effective moduli correctly, but need more comprehensive effective medium theories developed by Jenkins et al. [43]. In addition, the difference between the analytical prediction for the well-bonded model (two particles initially in contact remain in contact after the external load is applied) and the experimental results can be explained by the failure of the well-bonded model (see Makse [67]) to approximate the dynamic bending vibration of the granular system. It should be pointed out that 3D experiments of the granular materials loaded plate under quasi-static load were not performed there. The resonant response under quasi-static and dynamic loads on the 2D particles loaded beam is analyzed in Chapter 5 and 6 and compared to the 2D analytical model, which is discussed next.

Recall that the normalized bending frequency $\tilde{\omega}$ in region B (for relatively large

M) given in Eq. (4.46) becomes

$$\tilde{\omega} = M\sqrt{\left(\frac{\rho_b}{\rho_p}\right)^3 \frac{\bar{E}}{E_b}}. \tag{4.49}$$

Then, the slope of each $\tilde{\omega} - M$ curve in region B is given by

$$\sigma = \frac{\partial\tilde{\omega}}{\partial M} = \sqrt{\left(\frac{\rho_b}{\rho_p}\right)^3 \frac{\bar{E}}{E_b}}. \tag{4.50}$$

In region B (large layer thickness or large M), the effective Young's modulus of the beam-layer system $\bar{E}$ in Eq. (4.50) is considered to be the same as that of the effective of the 2D particle system in Eq. (4.43) because the elastic support beam has minor effect in bending frequency in this regime . By substituting the effective Young's modulus $\bar{E}$ in Eq. (4.39) into Eq. (4.49), the normalized resonant frequency in region B becomes

$$\tilde{\omega} = M\sqrt{C_B R^{3/2} Q(R/h)}, \tag{4.51}$$

where

$$C_B = \sqrt{\frac{1,024\rho g K\phi(1-\nu)}{\pi^2 b^2(1+\nu)(2-\nu)^2}\left(\frac{\rho_b}{\rho_p}\right)^6\left(\frac{E}{E_b^2}\right)}, \tag{4.52}$$

$$Q(R/h) = \int_{R/h}^{1}\sqrt{\frac{1-\tilde{y}}{\tilde{y}}}d\tilde{y} = \frac{\pi}{4} - \sqrt{\frac{R}{h}\left(1-\frac{R}{h}\right)} - \frac{1}{2}\arcsin\left(\frac{2R}{h}-1\right). \tag{4.53}$$

From Eq. (4.51)-(4.53), it can be seen that the bending frequency in region B depends on particle size (R), thickness of layer (M), and structure of particle packing ($\bar{n}$ and ϕ). Particularly, in term of particle size, layer of the bigger particles is stiffer than

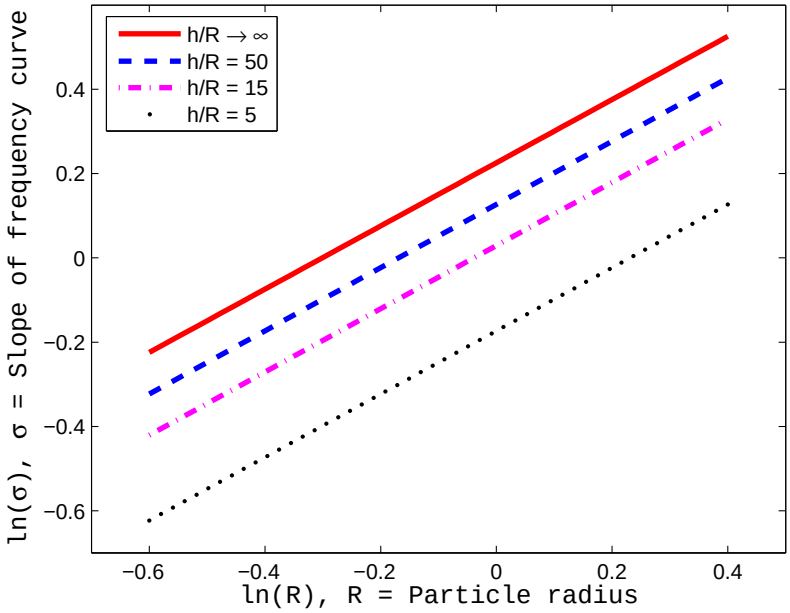

Figure 4.5: The dependence of the bending resonant frequency, σ, on the particle radius R in the "bending stiffness" regime (region B in Fig. 4.4): $\sigma(R) = \alpha R^{\beta}$ obtained from the analytical model for 2D particles (disks). The result shown is for the selected values of $h/R = 5$, $h/R = 15$, $h/R = 50$, and $h/R \to \infty$.

those of small particles. Finally, the dependence of slope bending resonance σ on particle size R for beam-layer system in region B is given by

$$\sigma = \frac{\partial \tilde{\omega}}{\partial M} = \sqrt{C_B R^{3/2} Q(R/h)} \propto \sqrt{R^{3/2} Q(R/h)}. \tag{4.54}$$

From the Eq. (4.54), it is obvious that the dependence σ depends on the particle size (radius) R. The plot of some values of h/R is shown in Fig. 4.5.

In Fig. 4.5, the dependence of bending resonance (slope of the resonant frequency-mass curves) σ linearly increases with increasing in particle radius R for all values of h/R. It implies that, for the same layer thickness (same large M), the layer of bigger

particles is stiffer than those of smaller particles. Also, as the particle layer of the same particle size is thicker (larger h/R), the dependence of the bending resonance increases; that is, the resonant frequency is high for large layer thickness. Note that as $h/R \to \infty$ (large layer thickness) such that $Q(0) = \pi/2$, the dependence σ is $R^{3/4}$. This dependence value obtained from the analytical model will be compared to our quasi-static and dynamic analysis in Chapter 5 and 6.

Chapter 5

Quasi-Static Analysis of the Granular-Layer/Elastic-Beam (GLEB) System

5.1 Introduction

For years, many researchers attempted to understand the response of granular materials and evaluate the mechanical properties of the granular assembly under a variety of applied loads. In this chapter, the behavior of the contact force chains and the resonant behaviors of the granular-layer/elastic-beam (GLEB) system under slow bending deformation are studied using the coupled DEM-FEM BobKit code. The study of the force chains will show a potential future strategy for enhancing the convection cells for more efficient mixing and segregation through combined shaking/bending vibrated granular system. In addition, the resonant behavior of the granular layer under a slowly applied (quasi-static) push-up load is examined via an analogy with an

equivalent elastic multilayered, or composite, beam (ECB). This analogy is based on evaluating the effective moduli and bending stiffness of the granular assembly. The bending stiffness of the granular layer is related to the particle sizes and this relation is obtained from a study of the particle-size dependence. The simulation results are compared with an analytical model, which was derived in chapter 4. The plan for the resonant analysis of the GLEB system is as follows: the quasi-static deformation of the GLEB system under a uniformly distributed load applied to the elastic beam in the upward direction is computed using the coupled DEM-FEM BobKit code; the "effective" Young's modulus of the granular layer is extracted from the deformation of the GLEB system using an analogy with an elastic composite beam (ECB) system; the resonant frequency of the GLEB system is numerically solved based on the computed Young's modulus of the granular layer; finally, the "equivalent" bending stiffness of the granular layer is computed. It should be noted that, based on the theory of elastic composite beam employed in this thesis, the first natural frequencies of the granular layer are the same as that of the GLEB system.

The sections in this chapter are arranged as follows: the simulation setup and parameters for this analysis are given first; the changes in the structure of the force chains of the granular layer under the slow-dynamic (quasi-static) bending deformation of the GLEB system for both close-packed monodispersed and random-packed polydispersed particles systems are studied with and without rolling resistance; the

resonant behavior of the GLEB system and the effective bending stiffness of the 2D granular layer are computed and qualitatively compared with the existing 3D dynamic experiments of the glass beads loaded on top of an elastic plate by Kang [46].

5.2 Simulation Setup and Parameters

For all simulations in this dissertation, granular layers of close-packed monodispersed particles and random-packed polydispersed particles are considered along with the parameters and material properties summarized in Table 5.1-5.2. The parameters for the elastic beam on top of which the granular particles rest are also contained in Table 5.1. To prepare the random-packed polydispersed particles system, a uniform distribution in particle size (radius) is first generated inside the computational domain for all three particle sizes given in Table 5.2 such that the particle radius is in the range $[0.8R, 1.2R]$ where R is the particle radius. Then, the particles are dropped under the action of gravity in the rigid box and the final positions of the particles will be used as their starting positions in the simulations. Fig. 5.1 shows particles preparation of the random-packed polydispersed particles for average particle radius of 0.625 mm.

The coupled 2D DEM-FEM model described in chapter 3 is used for the quasi-static (slow dynamics) analysis of the GLEB system when the elastic beam, loaded by

Table 5.1: Parameters and material properties used in the simulation.

Parameters and material properties	Value
Beam	
• Dimension (length, thickness, depth)	100 mm, 0.25 mm, 0.25 mm
• Number of discretized beam elements	50 elements
• Density	8,575 kg/m^3
• Young's modulus	103 GPa
• Poisson's ratio	0.34
Particle	
• Dimension (thickness)	0.25 mm
• Size (radius)	1.25 mm, 1.0 mm, 0.625 mm
• Density	2,600 kg/m^3
• Young's modulus	1 GPa
• Poisson's ratio	0.3
Wall	
• Density	8,575 kg/m^3
• Young's modulus	103 GPa
• Poisson's ratio	0.34
Contacting interface of all contacts	
• Sliding friction coefficient, μ_s	0.3
• Rolling friction coefficient, μ_r	0.03
• Normal restitution coefficient, ϵ_n (for Hookean-type force)	0.9
• Damping parameter, A (for Hertzian-type force)	
Particle radius = 1.25 mm	1.50E-6 s
Particle radius = 1.0 mm	1.20E-6 s
Particle radius = 0.625 mm	0.73E-6 s

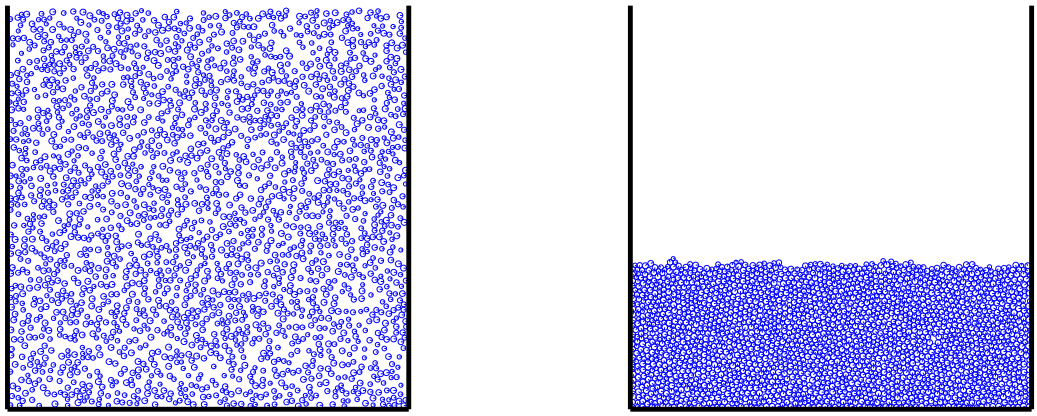

(a) (b)

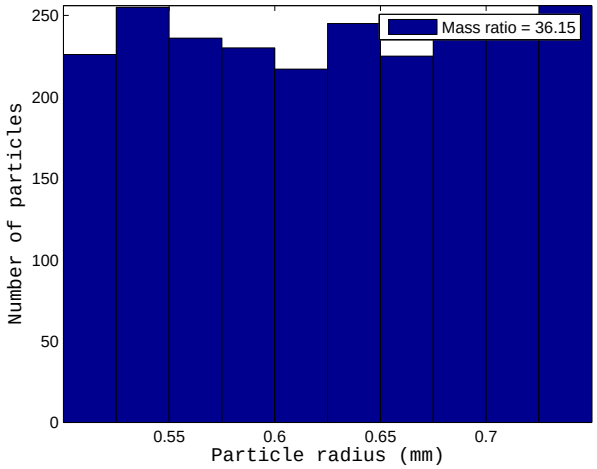

(c)

Figure 5.1: (a) A uniform distribution in particle size (radius, R) of 0.625 mm is first generated inside the computational domain (rigid box) such that the particle radius is in the range of [0.8R, 1.2R] before the particles are dropped under the gravity in the rigid box. (b) The final position from the dropped particles is used as the starting position of the granular-layer/elastic-beam (GLEB) system. (c) The histogram bar plot of the particle distribution obtained in (a) where the mean and standard deviation of this particle size are 0.626 and 0.073 mm.

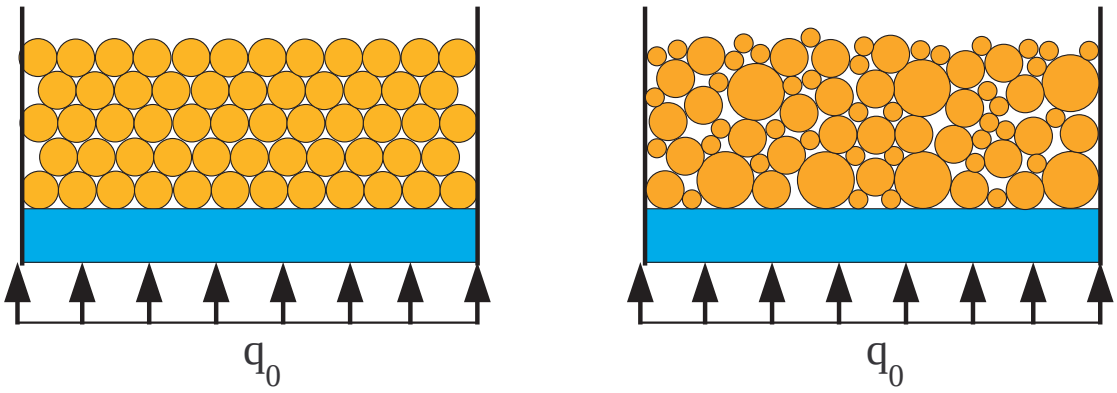

(a) (b)

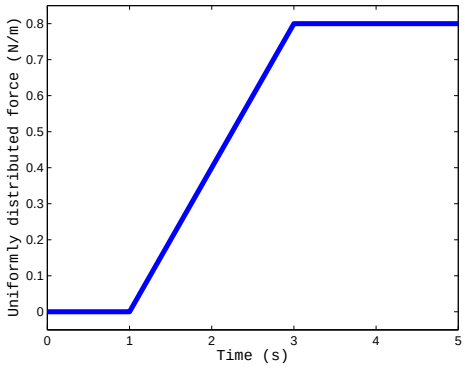

(c)

Figure 5.2: A granular-layer/elastic-beam (GLEB) system subjected to a uniformly distributed force $\mathtt{q}_0$ (force per unit length): (a) granular layers of close-packed monodispersed particles, (b) granular layers of random-packed polydispersed particles. (c) The uniformly distributed applied force, $\mathtt{q}_0$, as a function of time.

Table 5.2: Particle data used in the quasi-static analysis. Here, "monodispersed" and "polydispersed" are the short notations for the close-packed monodispersed and random-packed polydispersed particles, respectively.

Particle radius, R	Mass ratio		Number of particles
	Monodispersed	Polydispersed	
R = 1.250 mm	4.70	4.79	79
	9.41	9.84	158
	14.11	14.60	237
R = 1.000 mm	7.54	7.84	198
	11.32	11.69	297
	15.09	15.54	396
R = 0.625 mm	2.37	2.47	159
	4.73	4.89	318
	9.47	9.76	636
	14.20	14.58	954
	35.50	36.15	2385

the granular layer, is deformed in bending by a push-up uniformly-distributed force, as shown in Fig. 5.2a (for close-packed monodispersed particles), b (for random-packed polydispersed particles). The magnitude of the applied force (per unit length) is shown in Fig. 5.2c as a function of time. The structural changes that take place in the force chains, resonant behavior and effective bending stiffness of the granular layer during quasi-static bending of the clamped-clamped elastic beam loaded by the granular layer are studied. The system is allowed to reach an equilibrium position under its own weight for 1 s real time without any other applied loading. After that, the applied force linearly increases for 2 s (to reduce transient effects that would be caused by an applied force that is discontinuous) and stays constant for another

2 s (see Fig. 5.2c). Both random-packed polydispersed and close-packed monodispersed particles, with and without rolling resistance (rolling resistance is applied to all contacts: particle-particle, particle-wall, particle-elastic beam), are considered in the following sections.

5.3 Structure and Evolution of the Force Chains

In this section, we consider the structure of the force chains for the thickest granular layer (ratio of the granular layer's and the mass of the beam $\simeq 36$) because the richness of the structure of the force chains can be observed easier. For better visualization, a logarithmic scale is employed to compute the line thickness that represents the magnitude of the normal force in contact between particle-particle, particle-wall, or particle-finite element:

$$L = \mathtt{ln}\left[\frac{F_{ij}^{n}(\mathtt{exp}(1)-1)}{F_{\mathtt{max}}^{n}}+1\right], \tag{5.1}$$

where L is the line-thickness in the plot, F_{ij}^{n} is the magnitude of the contact normal force between pair (i,j), $F_{\mathtt{max}}^{n}$ is the maximum normal force in the system during the entire simulation event. Note that the log scale allows us to see forces that are several times smaller than the largest one plotted. The contact forces that are 100 times smaller than the largest normal force are left out during the post-processing stage.

The evolution of the force chains during quasi-static bending of the GLEB system for close-packed monodispersed and random-packed polydispersed particles, with and without rolling resistance, is discussed in the following section. Since, qualitatively, the evolution of the contact force chains for both linear and nonlinear force models is similar, the snapshots of the force chains for the linear force model are illustrated in this chapter.

5.3.1 Structure of the Force Chains for Close-Packed Monodispersed Particles

Fig. 5.3 shows the structural changes of the force chains taking place in the granular material during the bending deformation caused by the uniformly distributed force pushing upward on the beam, when rolling resistance is present. The first snapshot (at t = 0.025 s) shows the formation of arches with the granular layer resting mostly on the left and right end parts of the beam while the middle part, closest to the beam, a region of lower pressure is observed. This confirms the results in Baxter et al. [6], Luding [65] and Zhou et al. [111], which discuss the formation of such arches and transmittal of the force chains in granular piles on rigid supports. Here, on the elastic foundation, this result is preserved. The low pressure region in the middle and bottom of the granular layer is notable. Notice that high pressure occurs at the side walls. Side walls are not present in other simulations (see e.g Baxter et

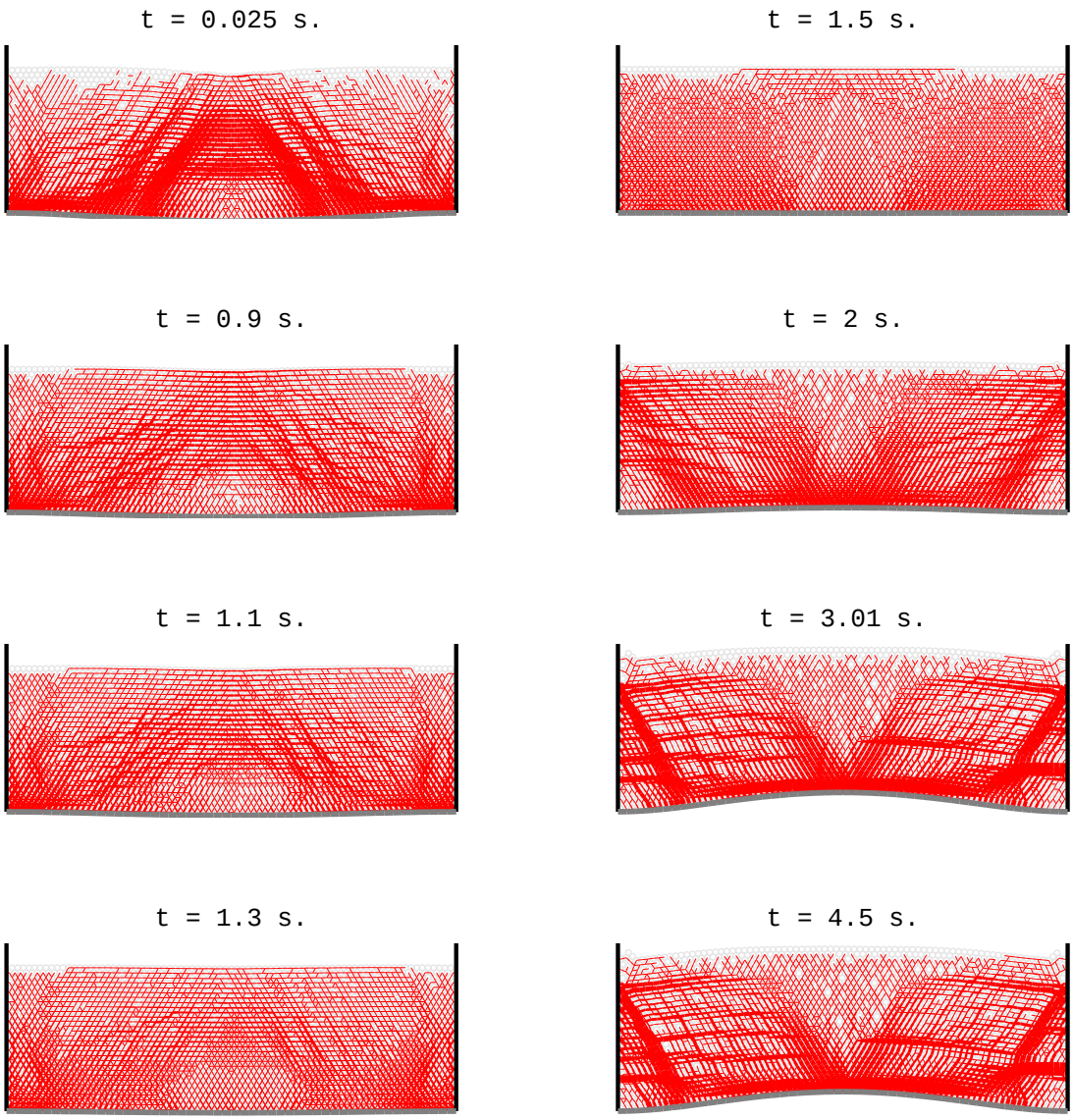

Figure 5.3: Snapshots of the contact force chains for close-packed monodispersed particles (shown in red) of the granular-layer/elastic-beam system under bending deformation with rolling resistance at t = 0.025 s, 0.9 s, 1.1 s, 1.3 s, 1.5 s, 2.0 s, 3.01 s, and 4.5 s. The particles, walls, and beam are drawn in light gray, black, and gray, respectively.

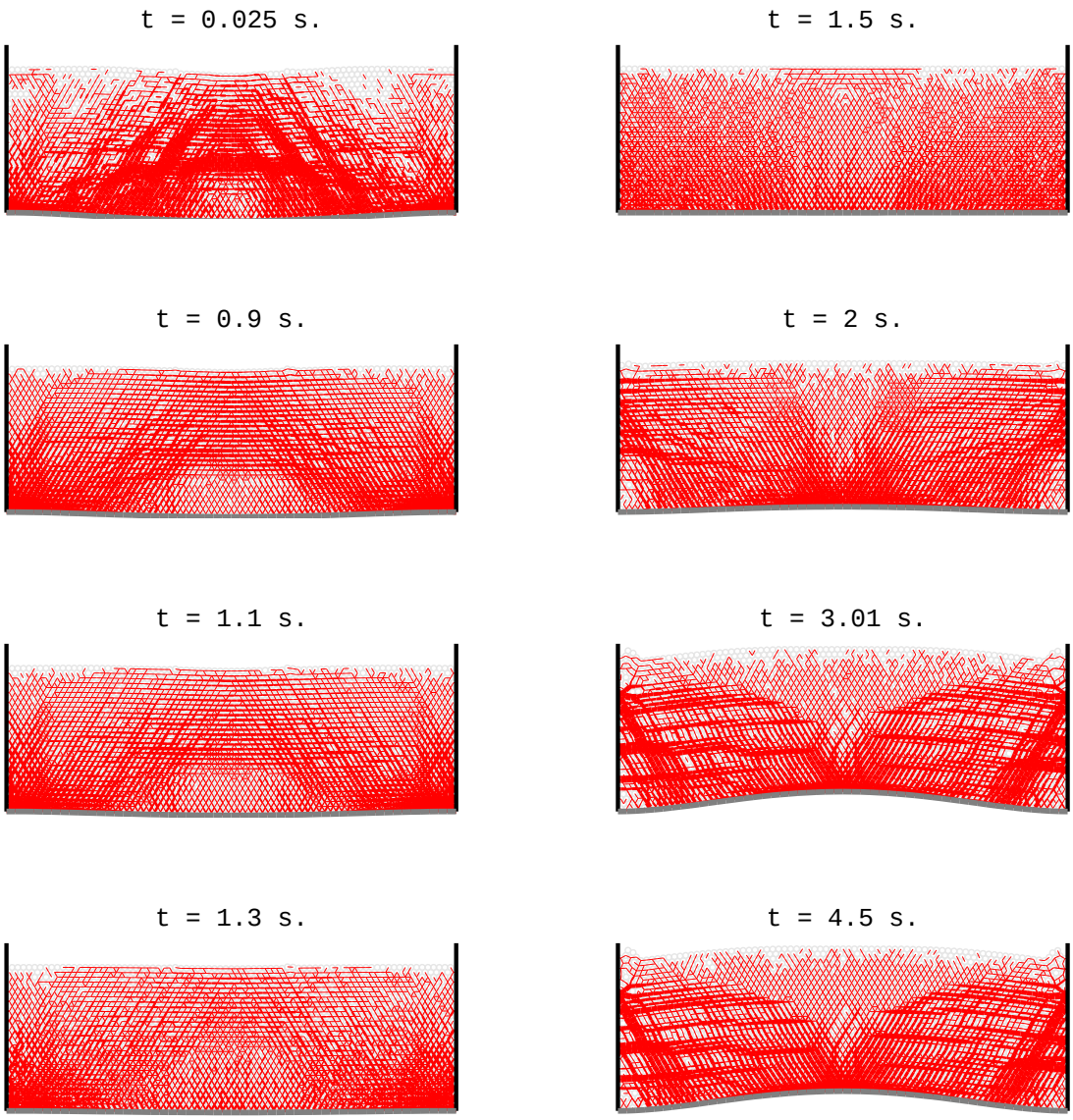

Figure 5.4: Snapshots of the contact force chains for close-packed monodispersed particles (shown in red) of the granular-layer/elastic-beam system under bending deformation without rolling resistance at t = 0.025 s, 0.9 s, 1.1 s, 1.3 s, 1.5 s, 2.0 s, 3.01 s, and 4.5 s. The particles, walls, and beam are drawn in light gray, black, and gray, respectively.

al. [6], Luding [65] and Zhou et al. [111]). The system reaches equilibrium before 1 s, at which instant the force chains look similar to those at 0.025 s (see figure at 0.9 s). It should be noticed that the force intensity at equilibrium position (see figure at 0.9 s) is more less than the relaxation position (see figure at 0.025 s at which the system starts to move downward and vibrate before reaching the equilibrium position) due to the inertia effect. As the push-up force is increasing in amplitude (after 1 s), the force chain arches start to be destroyed (see figures at 1.1 s, 1.3 s and 1.5 s) and a V-shaped area of low contact forces is formed in the upper center part of the layer (see figure at 1.5 s). With further upward bending of the granular layer, the system is developing force chains that start pushing against the side-walls and the middle portion of the beam (see figure at 2 s). Soon after the force stops from increasing (after 3 s, see figure at 3.01 s), and remains constant (see figure at 4.5 s) for the rest of the simulation, the force chain structure looks similar. Notice the "inverted arch" shape of the force chains that now push against the walls and rest against the middle part of the beam. The pressure at the corners of the granular layer is also reduced but it increases in the upper parts of the layer. A particularly interesting feature is the V-shaped region of low pressure bounded by strong force chains seen in the last picture in Fig. 5.3. The V-shaped area of the force chains generated during bending forms regions that may lead to convection cells for enhanced mixing in vibrated granular media (see Bobaru et al. [9]).

Without rolling resistance, the structural changes of the force chains evolved during bending deformation are shown in Fig. 5.4. The overall formation of the force-chain structures is similar to the case when rolling resistance is included. However, higher symmetry (see figures at 0.025 s) and more clear "inverted arch" shape (see figures at 3.01 s and 4.5 s) of the force chains are noticeable when the rolling resistance is included. In addition, the rolling resistance induces higher force intensity of the granular layers on top of the elastic beam (see figures at 2 s, 3.01 s and 4.5 s). This is true because high contact force is expected at the granular layer contact to the beam as the push-up force is continuously increasing. So far, the variation of the force chain structure is observed during quasi-static load (bending deformation). In the next section, the structural changes of the force chains for random-packed polydispersed granular particles are investigated.

5.3.2 Structure of the Force Chains for Random-Packed Polydispersed Particles

The structural changes in the force chains under quasi-static bending of the GLEB system by a distributed force in the upward direction applied to the beam, for a random-packed polydispersed granular layer with rolling resistance, are shown in Fig. 5.5. The first snapshot (t = 0.025 s) when the system starts to move downward and vibrate due to gravity before reaching equilibrium position (t = 0.9 s) shows

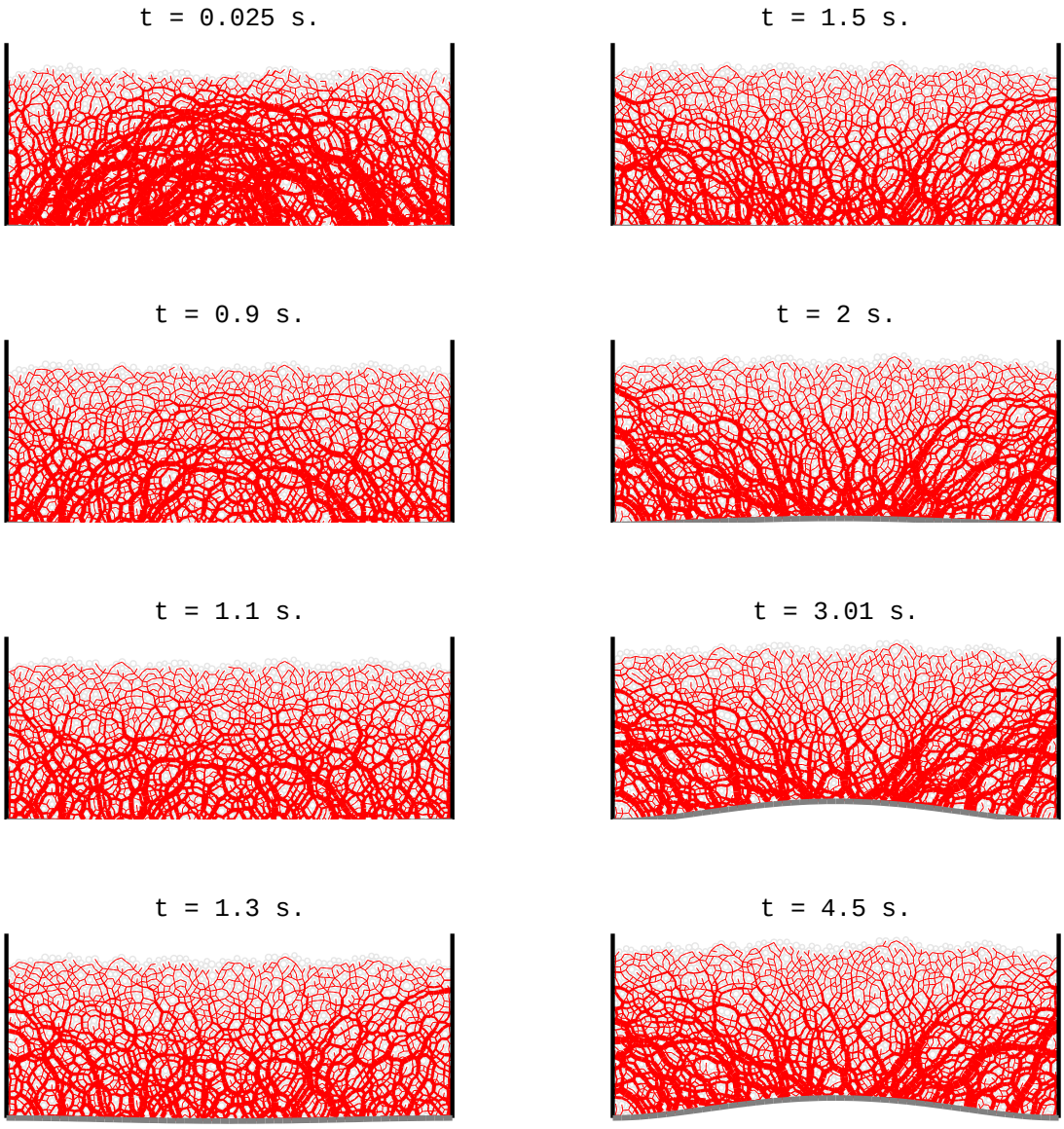

Figure 5.5: Snapshots of the contact force chains for random-packed polydispersed particles (shown in red) of the granular-layer/elastic-beam system under bending deformation with rolling resistance at t = 0.025 s, 0.9 s, 1.1 s, 1.3 s, 1.5 s, 2.0 s, 3.01 s, and 4.5 s. The particles, walls, and beam are drawn in light gray, black, and gray, respectively.

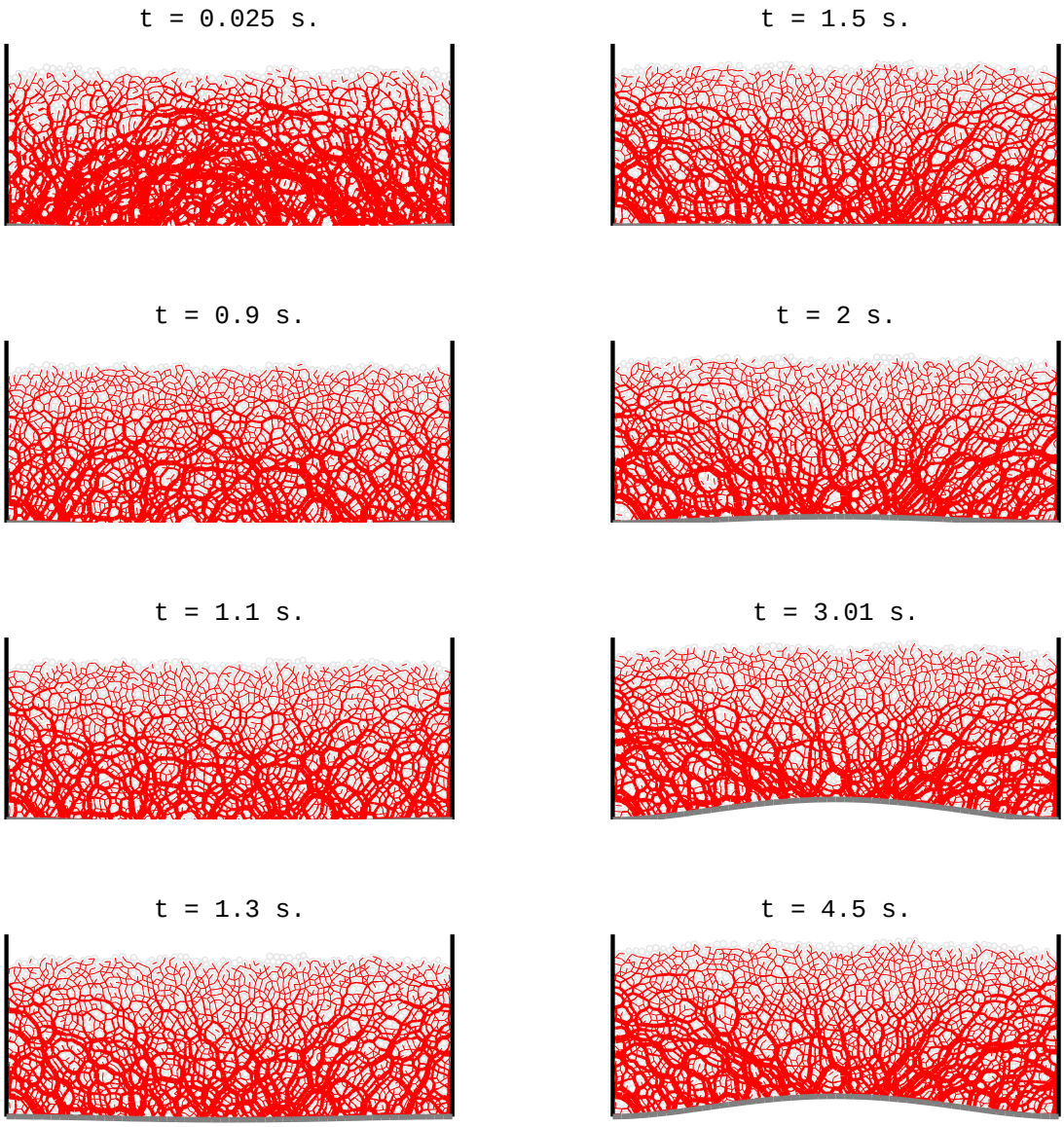

Figure 5.6: Snapshots of the contact force chains for random-packed polydispersed particles (shown in red) of the granular-layer/elastic-beam system under bending deformation without rolling resistance at t = 0.025 s, 0.9 s, 1.1 s, 1.3 s, 1.5 s, 2.0 s, 3.01 s, and 4.5 s. The particles, walls, and beam are drawn in light gray, black, and gray, respectively.

the formation of a "bush branches" of the granular layer resting on the elastic beam. These branches are arching together over the central part and resting mostly against the end parts of the beam. This arch formation is different from the close-packed monodispersed particles case, where a "pyramidal arch" formed. Also, it can be seen that high force intensity covers all over the top including the middle portion of the elastic beam, albeit with lower intensity over the middle section of the beam. After the system's relaxation (see figure at 0.9 s), the arch formation remains but lower intensity of the contact forces is observed. This observation remains for the case when the push-up force applies to the elastic beam (see figure at 1.1 s). Soon after the uniform load applied to the elastic beam beam (at t = 1.3 s and 1.5 s), higher pressure is observed at both side walls and the arch formations are destroyed. This is the beginning of the beam curving up. Under further pushing-up load (figures at 2 s, 3.01 s, and 4.5 s, high contact force intensity at the walls is noticeable. Due to the forces transmitted to the side walls, the lower pressure is now observed at the ends of the elastic beam (see figure at 4.5 s). Similar to the close-packed monodispersed particles' case, the "inverted arch" is observed when the elastic beam starts bending upward. The evolution of the structural changes in the force chains under the quasi-static pushing-up load without rolling resistance is shown in Fig. 5.6. The overall contact force formation is similar to the rolling resistant case.

5.4 Resonant Behavior of the GLEB System and Effective Bending Stiffness of the Granular Layer

In this section, the effective resonant behavior of the Granular-Layer/Elastic-Beam (GLEB) system is studied and qualitatively compared with dynamic experimental results conducted in 3D where a circular plate is loaded on top by a granular (glass bead) layer (Kang [46]). For comparison, the mass ratio (glass-bead mass/circular-plate mass) of a glass bead loaded plate system from the 3D dynamic experiment by Kang [46] is limited up to 12 because of available data. All analysis in this section, we use parameters and particle data given in Table 5.1-5.2 for linear (Hookean) and nonlinear (Hertzian) force models. The influence of rolling resistance is considered in this section as well. By "effective resonant behavior" we mean the resonant behavior of an equivalent composite, two-layered, beam (ECB) (see Fig. 5.7a) in which the lower beam is identical to the beam in the GLEB system and the upper beam has the same thickenss, density, and depth as the granular layer. The boundary conditions on the ECB system are clamped-clamped ends. Kang et al. [47] showed that the numerical results for both clamped and roller boundary conditions have a minor influence on the first resonant frequency for the regime of interest. A detailed discussion on the boundary and the interface conditions is given in Kang et al. [47].

From the computed mid-point displacement of the GLEB system, we compute the required elastic modulus for the upper beam in the ECB system (see Fig. 5.7a) that

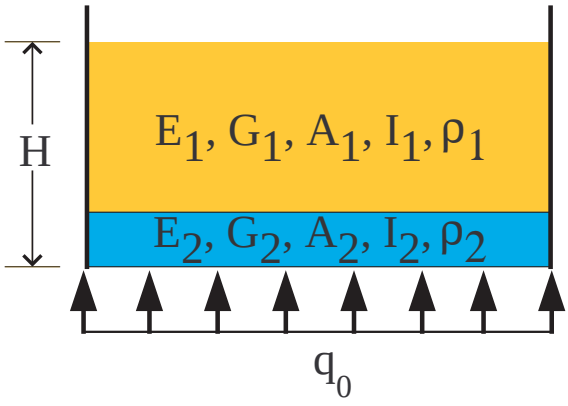

(a)

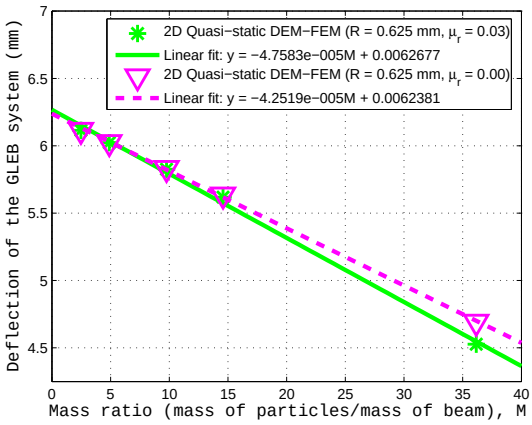

(b)

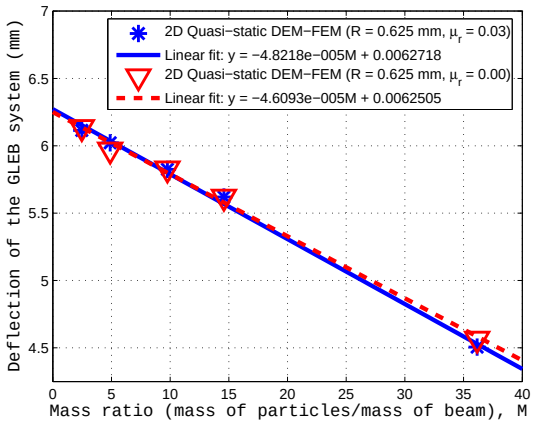

(c)

Figure 5.7: (a) The composite beam (ECB) system equivalent to the GLEB system in Fig 5.2. Total deflections of the granular-layer/elastic-beam (GLEB) system from the 2D quasi-static DEM-FEM analysis along with the linear curve fit for random-packed polydispersed particles of average radius of 0.625 mm based on: (b) Nonlinear spring-dashpot (Hertzian contact) model, (c) Linear spring-dashpot (Hookean contact) model. Results are shown for two cases: with (solid line) and without (dashed line) rolling resistance. Similar results for both contact force models with rolling resistance are observed. Without rolling resistance, however, the difference is noticeable for very thick granular layer.

would give the same displacement value for the same applied force. The resonant behavior of this ECB system is then computed based on the theory of multilayered (composite) beams. This resonant frequency is then considered to be the resonant frequency of the GLEB system. Fig. 5.7b, c show the mid-point deflections of the GLEB system (for random-packed polydispersed particles with the average particle radius of 0.625 mm) obtained from the 2D coupled DEM-FEM simulation for five different granular layer thicknesses (or mass ratios of 2.47, 4.89, 9.76, 14.58, and 36.15 in Table 5.2) along with a linear curve fit. For small deflection of the beam compared to the beam length, a linear curve fit is used to evaluate the mid-pint deflections at all other intermediate thicknesses. Here, the system deflections for both linear and nonlinear contact force models are compared. The parameters used for the top beam (granular layer) in the ECB system are given by (see also Table 5.1): $A_1 = H_1 b_1$, $I_1 = b_1 H_1^3/12$, $\rho_1 = M_1/V_1$, $V_1 = A_1 L$, $\nu_1 = 0.30$ where A_1 is the cross-sectional area, I_1 is the cross-sectional moment of inertia, ρ_1 is the average mass density, M_1 is the mass, V_1 is the volume, H_1 is the thickness, b_1 is the depth, L is the length, ν_1 is the Poisson's ratio, respectively. It should be noted that the selection of the Poisson's ratio is reasonable because its influence on the results, for this kind of deformation (bending), is minimal (see computations and discussions in Kang et al. [47]). To find the Young's modulus of the top beam in the ECB, a nonlinear equation from Eq. (5.2) that connects the bending stiffness and the deflection under a uniformly-distributed

force for a composite beam is numerically solved. This Young's modulus value is then used to compute the first bending resonant frequency for the ECB which will be considered as the first natural bending resonant frequency of the GLEB system.

5.4.1 Effective Young's Modulus of the Granular Layer from Bending Deformations

The procedure to compute The Young's modulus of the top beam (granular layer) are described as follows. For a given thickness, the Young's modulus (E_1) is computed from the nonlinear equation (Eq. (5.2), see Xu and Wu [104] for more detail). For the clamped-clamped (CC) boundary conditions on both beams (see Fig. 5.7a), the mid-point deflection of the ECB system under a uniformly distributed load is given by

$$y_{\mathtt{max}} = \frac{q_0 L^4}{384\overline{EI}} \left[1 + \left(\beta^2 - 1\right) f_{\mathtt{cc}}(\alpha L) + 48 \left(\frac{H}{L}\right)^2 \frac{\overline{EI}}{H^2 \overline{\kappa A G}} \right]. \tag{5.2}$$

Here $y_{\mathtt{max}}$ is the maximum (mid-point) deflection, q_0 is the uniformly distributed load, L and $H = H_1 + H_2$ are the length and total height of the two beams with H_i $(i = 1, 2)$ denoting the beams height, $EI = \sum EI = E_1 A_1 E_2 A_2 h^2/(E_1 A_1 + E_2 A_2)$ is the flexural stiffness of the composite beam with $\sum EI = E_1 I_1 + E_2 I_2$ and h being the distance between the centroid of two beams, $\overline{\kappa A G} = \kappa_1 A_1 G_1 + \kappa_2 A_2 G_2$ with κ_i $(i = 1, 2)$ denoting the shear correctors of the Timoshenko's beam theory and depending on the shape of the cross-section of the two beams, $\alpha^2 = k_s(1/E_1 A_1 + 1/E_2 A_2 + h^2/\sum EI)$

is the composite parameter related to the stiffness of the shear connector k_s, $\beta^2 = \overline{EI}/\sum EI$ with E_i, G_i, A_i, I_i $(i = 1, 2)$ denoting the Young's modulus, shear modulus, cross-sectional area, and second moment of area of the two beams, respectively. Note that the correction of the partial interaction (inter-layer slip between the contact surfaces) and shear deformation are given in the second and third terms in the brackets in Eq. (5.2), where

$$f_{\mathsf{cc}}(\alpha L) = \frac{48}{\alpha^2 L^2} - \frac{192\sinh(\alpha L/2)}{\alpha^3 L^3} + \frac{192\coth(\alpha L/2)\left[\cosh(\alpha L/2) - 1\right]}{\alpha^3 L^3}. \tag{5.3}$$

It should be noted that the clamped-clamped boundary conditions on the top beam are reasonable assumption here because using rolling boundary conditions on the top beam have a minor effect within our deformation regime of interest as it was shown in Kang et al. [47]. Moreover, the results of Kang et al. [47] for the match between a granular layer and a composite-plate elastic system (in the range of $\simeq 3 - 5$ MPa.) are used as an initial guess for the Young's modulus value, for each granular layer thickness, in the nonlinear equations solver (MATLAB's "fzero" function) employed in the solution of Eq. (5.2). The values of the Young's modulus of the granular layer obtained from the linear (Hookean contact) and nonlinear (Hertzian contact) force models for both close-packed monodispersed and random-packed polydispersed particles are given in the Fig. 5.8.

One can see that the Young's modulus values decrease almost monotonically as

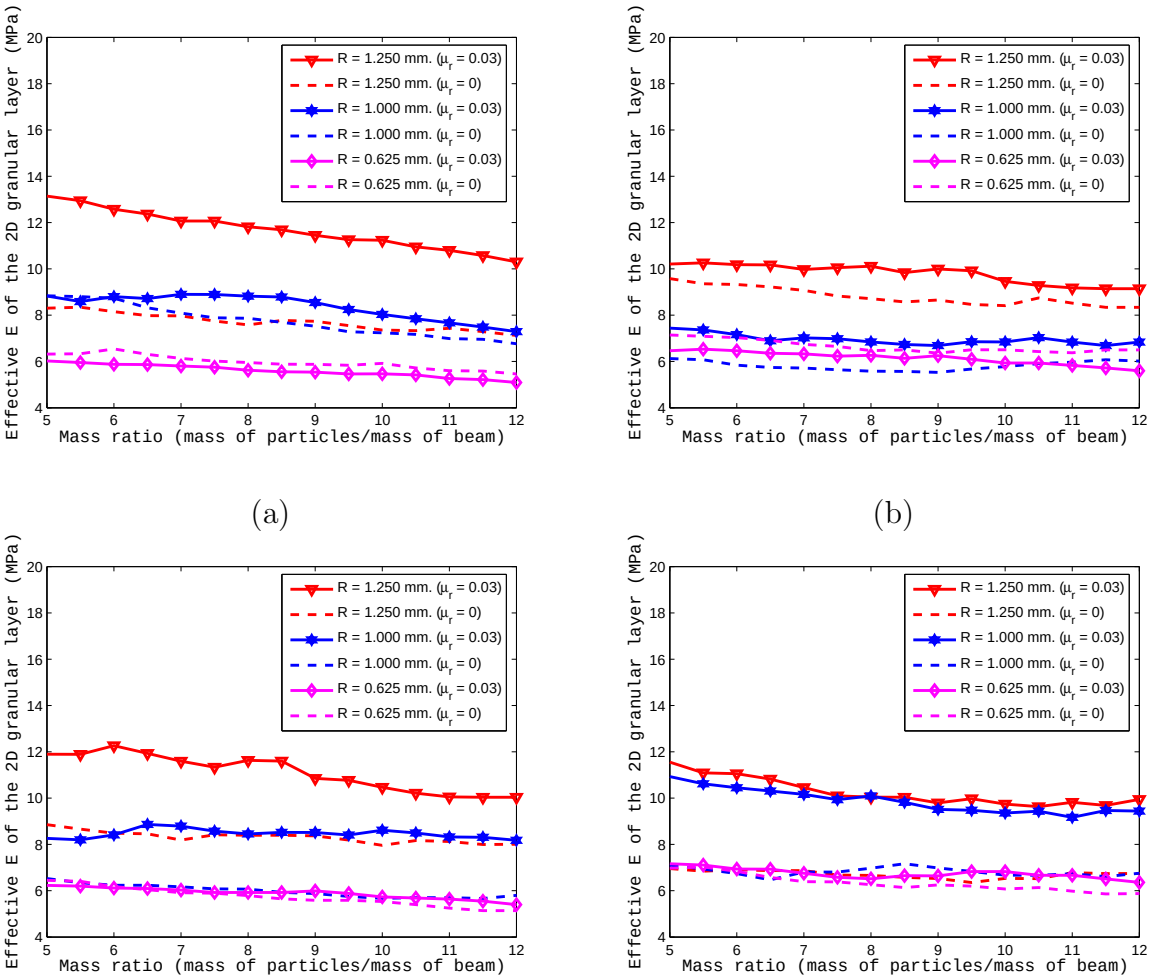

Figure 5.8: The effective Young's modulus of the 2D granular layer from the 2D quasi-static DEM-FEM analysis for close-packed monodispersed and random-packed polydispersed particles as a function of the layer thickness (or mass ratio). Results shown are based on: Linear spring-dashpot (Hookean contact) model, (a) for close-packed monodispersed particles, and (b) for random-packed polydispersed particles; and Nonlinear spring-dashpot (Hertzian contact) model, (c) for close-packed monodispersed particles, and (d) for random-packed polydispersed particles.

the particle layer becomes thicker. For example, the values of Young's modulus for the biggest particle size, in the present of rolling resistance, decrease from 13 MPa (for the thinner layer) to 10 MPa (for the thicker layer) for both force models used in this dissertation. These values are slightly higher than those obtained from the three-dimensional experiments of Kang et al. [47] and Yanagida et al. [106]. In addition, the trends in terms of increased layer thickness are opposite to those measured and shown in Fig. 7 of Kang et al. [47]. These differences are to be expected since the contact forces scale differently with particle size in 2D than in 3D. Also, these values are significantly lower than those from wave speed measurements (see Johnson [45], Oelze et al. [77]). When rolling resistance is included in the simulations, the Young's modulus values for the bigger particles are larger than those for the smaller particles. Moreover, the values of Young's modulus for the random-packed polydispersed particles are lower than those of close-packed monodispersed particles. This behavior can be observed for both the linear and nonlinear contact force models. The scaling of the bending stiffness of the granular layer with the particle size is given in section 5.4.4.

5.4.2 Resonant Behavior of the GLEB System

Based on the Young's modulus values computed above, the first resonant frequencies of the ECB system are then obtained by solving the characteristic equation of

free vibration (see Xu and Wu [104]), for clamped-clamped (CC) ends:

$$\begin{vmatrix} \mathbf{A}_{\mathtt{c1}}(0) & \mathbf{A}_{\mathtt{c2}}(0) & \mathbf{A}_{\mathtt{c3}}(0) \\ \mathbf{A}_{\mathtt{c1}}(L) & \mathbf{A}_{\mathtt{c2}}(L) & \mathbf{A}_{\mathtt{c3}}(L) \end{vmatrix} = 0, \tag{5.4}$$

where

$$\mathbf{A}_{\mathtt{c1}}(x) = \begin{bmatrix} \sin(k_1 x) & \cos(k_1 x) \\ (-g_{\mathtt{c1}} k_1^3 + g_{\mathtt{c2}} k_1)\cos(k_1 x) & (g_{\mathtt{c1}} k_1^3 - g_{\mathtt{c2}} k_1)\sin(k_1 x) \\ (k_1^5 - g_{\mathtt{c3}} k_1^3)\cos(k_1 x) & -(k_1^5 - g_{\mathtt{c3}} k_1^3)\sin(k_1 x) \end{bmatrix},$$

$$\mathbf{A}_{\mathtt{c}i}(x) = \begin{bmatrix} \sinh(k_i x) & \cosh(k_i x) \\ (g_{\mathtt{c1}} k_i^3 + g_{\mathtt{c2}} k_i)\cosh(k_i x) & (g_{\mathtt{c1}} k_i^3 + g_{\mathtt{c2}} k_i)\sinh(k_i x) \\ (k_i^5 + g_{\mathtt{c3}} k_i^3)\cosh(k_i x) & (k_i^5 + g_{\mathtt{c3}} k_i^3)\sinh(k_i x) \end{bmatrix}, \qquad i = 2, 3$$

$$\begin{aligned} g_{\mathtt{c1}} &= \alpha^2 \gamma_3 (\gamma_5 + 1), \\ g_{\mathtt{c2}} &= \alpha^2\beta^2 + \left(\alpha^2\gamma_3 - 2\alpha^2\beta^2\gamma_3 - 2\beta^4\right)\gamma_1\gamma_3\omega^2, \\ g_{\mathtt{c3}} &= -\alpha^2 - \frac{\beta^2\gamma_6}{(\gamma_5+1)} + \frac{\gamma_1\gamma_3\omega^2}{(\gamma_5+1)} + \beta^2\gamma_1\gamma_3\omega^2 + \frac{\alpha^2 g_{\mathtt{c4}}}{g_{\mathtt{c2}}}, \\ g_{\mathtt{c4}} &= \alpha^2 - \beta^2\gamma_1\gamma_3\gamma_4\omega^4 - \left(\alpha^2\gamma_3 + \beta^2\right)\gamma_1\gamma_3\omega^2, \\ \gamma_1 &= \frac{\overline{\rho A}}{\overline{EI}}, \gamma_2 = \frac{\overline{\rho I}}{\overline{\rho A}}, \gamma_3 = \frac{\overline{EI}}{\overline{\kappa AG}}, \gamma_4 = \frac{\overline{\rho I}}{\overline{\kappa AG}}, \gamma_5 = \frac{F}{\overline{\kappa AG}}, \gamma_6 = \frac{F}{\overline{EI}}. \end{aligned} \tag{5.5}$$

Here ω is the resonant frequency of the composite beam, F is the applied axial force (where $F = 0$ in our case), $\overline{\rho A} = \rho_1 A_1 + \rho_2 A_2$, $\overline{\rho I} = \rho_1 I_1 + \rho_2 I_2$, ρ_i $(i = 1, 2)$ is the mass density of the beams, $\pm k_i$ $(i = 1, 2, 3)$ are the six eigen-roots of the equation

$$\begin{aligned} &(\gamma_5 + 1)\, k^6 + \left[\beta^2\gamma_1\gamma_2(\gamma_5+1)\,\omega^2 + \gamma_1\gamma_3\omega^2 - \alpha^2(\gamma_5+1) - \beta^2\gamma_6\right] k^4 + \\ &\left[\beta^2\gamma_1\gamma_4\omega^4 - \beta^2\gamma_1\omega^2 - \alpha^2\gamma_1\gamma_3\omega^2 - \alpha^2\gamma_1\gamma_2(\gamma_5+1)\,\omega^2 + \alpha^2\gamma_6\right] k^2 + \\ &\left(\alpha^2\gamma_1\omega^2 - \alpha^2\gamma_1\gamma_4\omega^4\right) = 0. \end{aligned} \tag{5.6}$$

The resonant frequencies of the ECB system, obtained from numerical computation by solving the characteristic equation (Eq. (5.4)) together with Eqs. (5.5)-(5.6), are shown in Fig. 5.9.

The resonant bending frequencies in the presence of rolling resistance of the ECB (or, equivalently, of the GLEB) system normalized by the frequency of the bottom beam alone, for various thicknesses of the top beam (which replaces the granular layer), are shown in Fig. 5.9. For a qualitative comparison, in Fig. 5.9, some of the 3D experimental results on glass bead layers loaded on a circular plate by Kang [46] (see Fig. 4.4) are included. Note that the contact force models used in our simulations correspond to the 2D Hookean (linear) and Hertzian (nonlinear) contacts, and the scaling with the particle radius in 2D (disks) differs from that in 3D (spheres). The experimental data in Kang [46] was obtained from experiments performed using a circular plate loaded on top by granular materials (sieved glass beads) and driven to resonance by acoustic wave sweep. As the granular mass loading the beam increases, the thickness of the granular layer does too, and this provides additional bending stiffness to that of the supporting beam. The mechanism responsible for this phenomenon is the behavior of the force chains, shown in the preceding section. An increased (bending) stiffness of the GLEB system results in a higher resonant frequency compared to the case when the supporting beam is loaded by a mass with no stiffness (such as a liquid), which is called a "mass-loaded" beam (see Fig. 5.9).

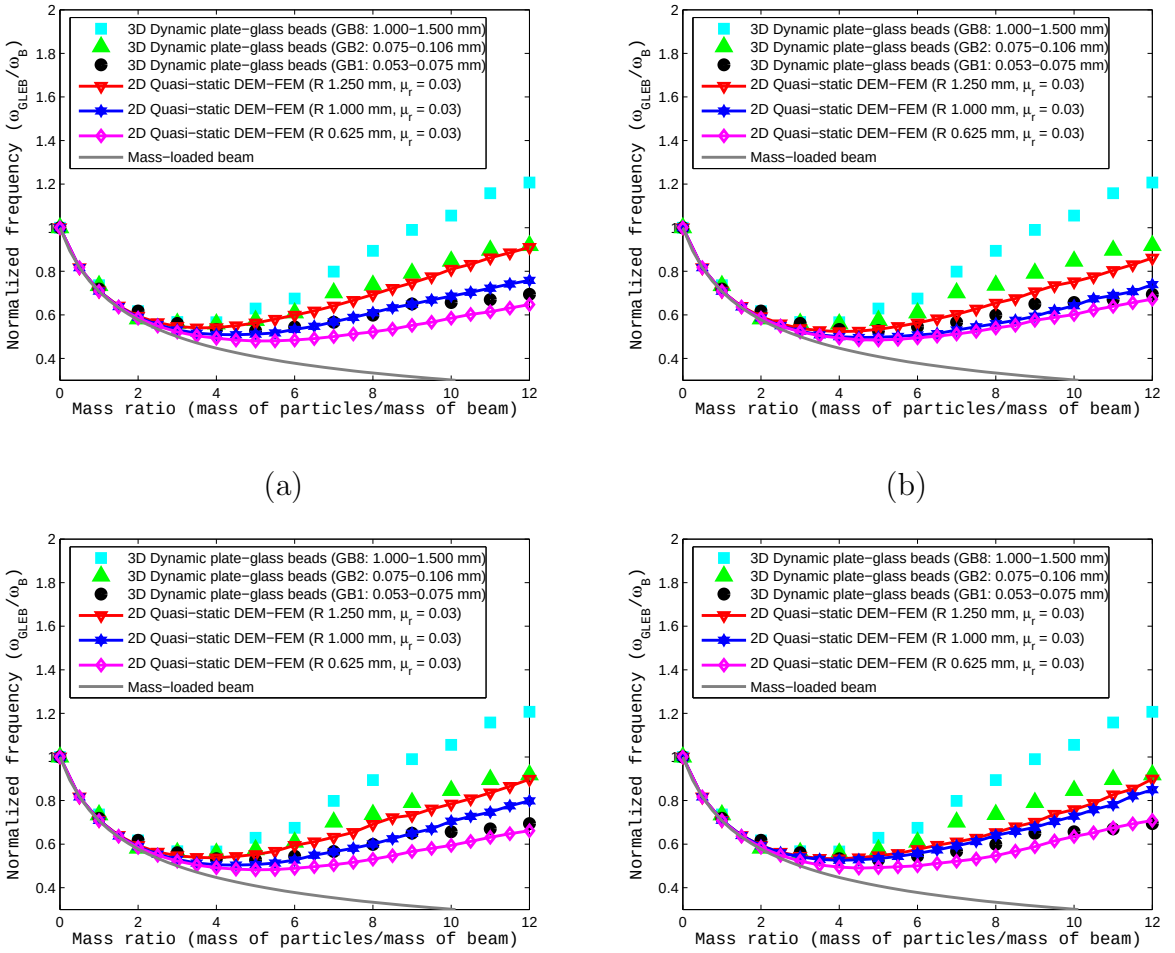

Figure 5.9: The first resonant frequency from the 2D quasi-static DEM-FEM analysis and 3D dynamic plate-glass beads by Kang [46]. The resonant frequency of the "equivalent composite beam" (ECB), or equivalently the "granular-layer/elastic-beam" (GLEB) system, normalized by the frequency of the lower elastic beam and the experimental results normalized by the frequency of the supporting plate. Results shown are based on: Linear spring-dashpot (Hookean contact) model, (a) for close-packed monodispersed particles, and (b) for random-packed polydispersed particles; and Nonlinear spring-dashpot (Hertzian contact) model, (c) for close-packed monodispersed particles, and (d) for random-packed polydispersed particles.

It can be seen that the resonant frequencies fall into two regimes: "mass dominant" regime, up to mass ratios $\simeq 3$, and "bending stiffness" regime, for mass ratios $>$ 5. Two regimes are observed from the experiment for the glass-bead loaded plate system. Although the present computations are done in 2D and using quasi-static bending deformation, the coordination with the 3D experimental results obtained from dynamic resonance is remarkable. In the mass-dominant regime, the frequency decreases as the mass increases with no addition in bending stiffness. In contrast, for the bending-stiffness regime, the frequency increases as the thickness (or mass ratio) increases resulting in a stiffer system. As seen from the figures, both the linear and nonlinear force models give similar results in presence of rolling resistance (see Fig. 5.9a, c for close-packed monodispersed particles). The difference in the resonant frequencies, however, for close-packed monodispersed and random-packed polydispersed particles (see Fig. 5.9a, b for linear, and Fig. 5.9c, d for nonlinear force models) is noticeable particularly as the mass ratio > 6. The granular layer of close-packed monodispersed particle results in higher resonant frequencies. The shift in resonant frequencies is observed for different particle sizes; the layer with larger particles results in higher bending resonant frequencies. This observation is true for all simulation results in this section. For smallest particle size (radius of 0.625 mm), no difference in frequency is observed regardless of particle packing and force model used. This is likely due to the fact that rolling resistance, which enhances

the resonant frequency, is dependent on the particle size as given in Eq. (3.26) for the Johnson model. In contrast with the 3D dynamic experimental data by Kang [46], the coupled 2D DEM-FEM quasi-static simulations show that the resonant frequencies continue to increase as the thickness increases whereas the experimental values show a levelling of the frequencies for larger mass ratios (thicker layers) especially for the bigger particle sizes. One of the explanations for the observed experimental results is that once the granular layer becomes too thick, driving it into resonance requires forcing amplitudes that lead to a nonlinear response with possible separation from the supporting plate which is difficult to process in the same manner as the one described in Kang et al. [47].

5.4.3 Effective Bending Stiffness of the Granular Layer

The values of computed (equivalent) bending stiffness of the granular layer (top beam) in the ECB system, for various particle sizes, as a function of the layer thickness (or mass ratio) in the presence of rolling resistance are shown in Fig. 5.10. The experimental results from Kang [46] are also shown for a qualitative comparison. The calculation of the bending stiffness of the granular layer D_1 is based on the beam thickness H_1 as $D_1 = E_1 I_1(H_1)$ with E_1 being the Young's modulus of the granular layer obtained from the preceding section. Notice that the effective bending stiffness of the 2D granular layer compares well with the experimental values obtained via

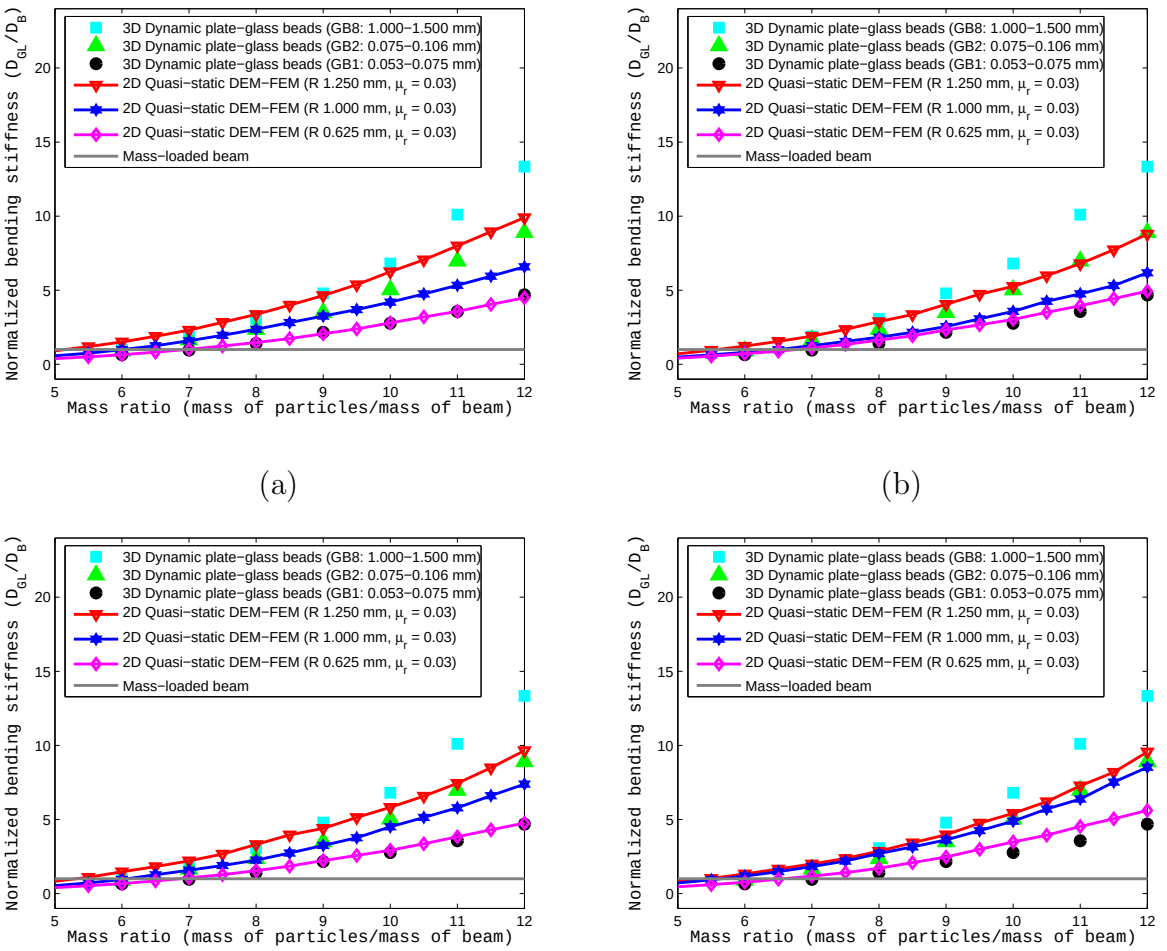

Figure 5.10: The effective bending stiffness from the 2D quasi-static DEM-FEM analysis and 3D dynamic plate-glass beads by Kang [46]. The computed effective bending stiffness of the granular layer (or the top beam in the ECB system) are normalized by the bending stiffness of the lower elastic beam; the experimental results are normalized by the bending stiffness of the supporting plate. Results are based on: Linear spring-dashpot (Hookean contact) model, (a) for close-packed monodispersed particles, and (b) for random-packed polydispersed particles; Nonlinear spring-dashpot (Hertzian contact) model, (c) for close-packed monodispersed particles, and (d) for random-packed polydispersed particles.

the 3D dynamic plate tests. The results from the coupled 2D DEM-FEM model show that the granular layer becomes stiffer than the elastic beam alone as the mass ratio becomes larger than about 5-7 depending on the particle size. The bigger the particles the stiffer the granular layer they form (see Fig. 5.10). Results from linear and nonlinear force models are fairly similar particularly when the rolling resistance is included (see Fig. 5.10a, c, and Fig. 5.10b, d). The difference in bending stiffness of the particle layer can be observed between close-packed monodispersed and random-packed polydispersed particles. The bending stiffness of the granular layer for the random-packed particles is less compared to the close-packed particles (see Fig. 5.10a, b, and Fig. 5.10c, d). That is, the layer of the close-packed particles is stiffer than the random-packed particles.

5.4.4 Particle-Size Dependence (PSD) of Bending Resonance of the Granular Layer

In this section, the dependence of the sizes of 2D granular particles in the granular layer on the shift in resonant frequency, within the bending stiffness regime (mass ratio > 5), is investigated. The procedure to obtain the particle-size dependence of bending frequency σ within the "bending stiffness" regime (Region B) are as follows:

- From the bending resonant frequency ($\tilde{\omega} - M$) curves obtained in subsection

5.4.2, we apply "linear" fit using MATLAB function "polyfit" to get the dependence of bending frequency σ corresponding to each particle size R. Here the linear fit is used because the dependent parameter σ is expected to linearly depends on M for relatively large M (see Eq. (4.50-4.51) in section 4.4).

- Based on the power-law fit $\sigma = \alpha R^{\beta}$, we apply "linear" fit using MATLAB function "polyfit" to the function $\mathtt{ln}\sigma = \beta \mathtt{ln}R + \mathtt{ln}\alpha$ so that the β represents the slope of the $\mathtt{ln}\sigma - \mathtt{ln}R$ plot.

The values of the particle-size dependence σ in the region B obtained from our quasi-static analysis are listed in Table 5.3. It is clear that the dependence of the bending frequency σ increases as increasing in particle radius R for all cases. Note that these dependence values are much larger than those of 3D dynamic experiments by Kang [46] for the glass beads loaded plate. For example, for the glass bead size of 1.0-1.5 mm (GB8) compared to particle radius of 1.25 mm, the dependence (slope) of the bending frequency σ in region B obtained from the 3D dynamic experiment is 0.109, but about 4.453 in average for all cases listed in Table 5.3. The difference may due to "2D versus 3D" or "quasi-static versus dynamic".

As shown in section 4.4, the analytical dependence of the slope of the resonant curves σ for an aggregate of random-packed monodispersed disks (2D) in the granular layer is 3/4; that is, $\sigma \propto R^{0.75}$ (Eq. (4.54)) where R is the particle radius.

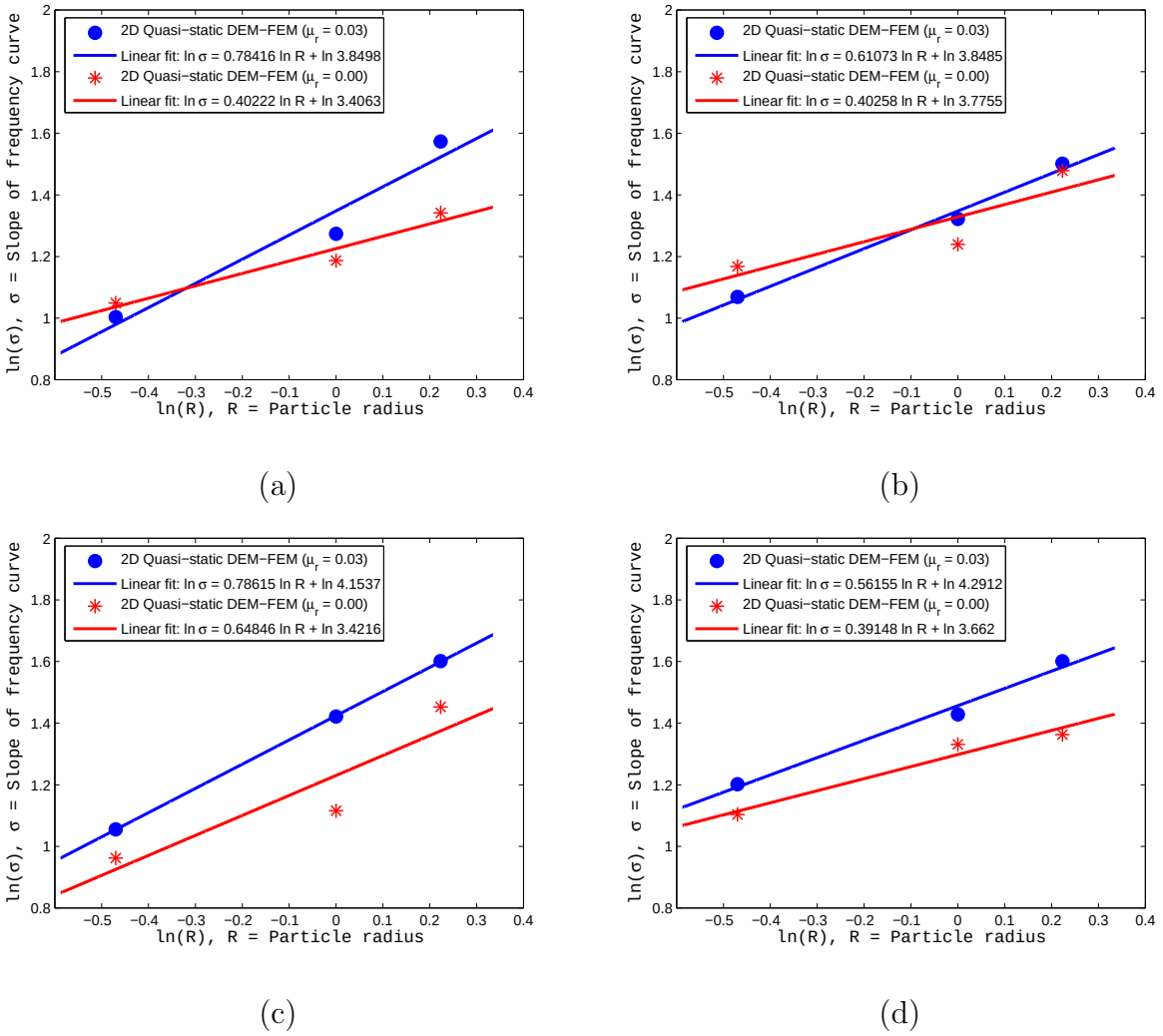

Figure 5.11: The dependence of the bending resonant frequency, σ, on the particle radius R in the "bending stiffness" regime: $\sigma(R) = \alpha R^{\beta}$ from the 2D quasi-static DEM-FEM analysis. Note that in $\ln\sigma - \ln R$ plot the β value represents the slope of the straight line. The analytical result for 2D disks gives $\beta = 0.75$. Results shown are based on: Linear spring-dashpot (Hookean contact) model, (a) for close-packed monodispersed particles, and (b) for random-packed polydispersed particles; and Non-linear spring-dashpot (Hertzian contact) model, (c) for close-packed monodispersed particles, and (d) for random-packed polydispersed particles.

Table 5.3: The slope of the frequency curves σ obtained from the 2D quasi-static DEM-FEM analysis for the close-packed monodispersed and random-packed polydispersed particles with three different particle radii, R, of 1.25, 1.0, and 0.625 mm. Results shown are based on the nonlinear (Hertzian contact) and linear (Hookean contact) force models with and without rolling resistance.

	Radius, R (mm)	$\sigma_{\texttt{Hertzian}}$		$\sigma_{\texttt{Hookean}}$	
		$\mu_r = 0.03$	$\mu_r = 0$	$\mu_r = 0.03$	$\mu_r = 0$
Monodispersed particles	R = 1.250	4.959	4.274	4.823	3.825
	R = 1.000	4.143	3.051	3.574	3.277
	R = 0.625	2.873	2.617	2.728	2.855
Polydispersed particles	R = 1.250	4.957	3.908	4.488	4.387
	R = 1.000	4.173	3.784	3.751	3.454
	R = 0.625	3.326	3.015	2.912	3.215

To compare with the analytical result, the particle-size dependence of the bending resonant frequencies obtained from the quasi-static analysis of the ECB system is illustrated in the Fig. 5.11. The simulation for both linear (Hookean contact) and nonlinear (Hertzian contact) force models of the close-packed monodispersed particles (see Fig. 5.11a, c) gives good results compared to the analytical model with the relative error less than 5%, in particular, when the rolling resistance is included. Without rolling resistance, however, the nonlinear contact force gives more accurate result than the linear force model. For example, the close-packed monodispersed particles, the error from the nonlinear model is approximately 13 % but 46 % for the linear model. For random-packed polydispersed particles (see Fig. 5.11b, d) the larger error is obtained regardless of the rolling resistance. This is due to the fact that the dependence of the resonant frequency curve from the analytical model is based

on random-packed monodispersed particles with no particle rotation (well-bonded model).

5.5 Summary and Conclusions

In conclusion, the coupled 2D Discrete Element Method-Finite Element Methods (DEM-FEM) simulation is implemented and used to analyze the behavior of granular layers under bending deformation. For a granular-layer/elastic-beam (GLEB) system, the structural changes taking place in the force chains during a slow-dynamics (quasi-static) push-up bending of the system are investigated. An analogy with a composite elastic beam is used to extract, from the computed DEM-FEM response, the Young's modulus of the corresponding granular layer. The values are in the range of 6-13 MPa for the case when rolling resistance is considered and 6-10 MPa when rolling resistance is absent. These values are slightly higher than those obtained from the experiments of Kang et al. [47] and Yanagida et al. [106], which are likely due to the difference between the Hertzian contact forces in 2D (for disks) compared to 3D (for spheres). The obtained values are significantly lower than those expected from wave speed measurements (see Johnson [45], Oelze et al. [77]). From the Young's modulus values, the first resonant bending frequencies of the equivalent composite beam (ECB) system, which is analog to our GLEB system, for various thicknesses of the

granular layer on top of the elastic beam, are determined. The corresponding bending stiffness of the granular layer alone is computed. The values obtained match qualitatively well the experimental results conducted in 3D experiments on glass beads on top of an elastic circular plate (see Kang [46]) even if the contact model in 2D is different from that in 3D. There is an increase in the granular layer bending stiffens with an increase in the layer thickness. For close-packed monodispersed particles, the quasi-static simulation results for both linear (Hookean contact) and nonlinear (Hertzian contact) spring-dashpot models are quite similar particularly in presence of rolling resistance. The evolution of the force chain structures shows that the stiffening effect can be explained by the reversal of the self-forming force-chain arches, which, instead of resting on the supporting beam, now (when the system is bent upwards) push against the side-walls and the middle of the beam. Furthermore, the layer of close-packed monodispersed particles behaves more stiffer than the random-packed polydispersed particles. The 3D dynamic experimental evidence in Kang [46] points toward a discrepancy between the measured particle-size dependence of bending resonance of the granular layer and the one predicted by well-bonded static analytical 3D models. In contrast, the 2D quasi-static results above lead to a particle-size dependence that matches the analytical model based on 2D contacts. For a possible prediction of the 3D experimentally-observed particle-size dependence reported in Kang et al. [47] and explanation of the discrepancy with the analytical values given

by well-bonded effective media models, a simulation of dynamic vibration and resonant behavior of the GLEB system is needed. In the next section, we investigate the behavior of the GLEB system under dynamic loading.

Chapter 6

Dynamic Analysis of the Granular-Layer/Elastic-Beam (GLEB) System

6.1 Introduction

From the preceding section for quasi-static analysis, the bending resonance land within those values obtained from the 3D dynamic experiments. Even the results for 2D quasi-static simulation are close to the 3D dynamic experiments, they do not match well for a given particle size. Possible implications for this discrepancy are "2D versus 3D" and "static versus dynamic" analysis. For simplicity, we continue to use the BobKit code for 2D dynamic analysis. In this chapter, the resonant behavior of a granular-layer/elastic-beam (GLEB) system under small oscillating force is studied using the BobKit code. Various parameters, including the material properties of a particle and properties of contact interfaces, effect to the system resonance are

examined. In addition, the mechanical properties of the granular assembly such as equivalent bending stiffness of the layer, under system resonance are investigated. The relationship between particle sizes of the granular assembly and bending stiffness of the layer is also examined and compared to the analytical model and an existing dynamical experiments of the 3D granular system loaded on top of an elastic plate contacted by Kang [46].

In this dynamic analysis, the input energy, in term of the driving force and frequency, for the linear response is first investigated. The driving force and driving frequency is considered as an input energy for the 2D granular-layer/elastic-beam system whereas an acoustic wave transmitted from the energy source to excite the bottom elastic plate of the 3D granular-layer/elastic-plate system (Kang [46]). Some aspects from the linear and nonlinear force models used in the quasi-static analysis to the shift change in the resonant frequency of the GLEB system are also pointed out. Followed by the material properties of a particle and contact interfaces influences in the resonant behaviors of the GLEB system are examined. The resonant behaviors of the GLEB system obtained from the BobKit code for 2D dynamic analysis are compared to the 3D experiments by Kang [46].

6.2 Methodology to Extract the Frequency Response

In 3D dynamic experiments, a frequency sweep is used through an acoustic speaker to drive a plate loaded by a granular layer into resonance. Here, the input energy in term of driving force and driving frequency is considered in 2D dynamic simulation for analogy with 3D case. In dynamic analysis, the bending resonance of the GLEB system is explicitly obtained by transforming the response amplitude in time domain into the frequency domain using the Fast-Fourier-Transform (FFT). Note that the response amplitude is considered as the vertical displacement of the supporting beam in the GLEB system computed by the BobKit code. The procedure of the transformation are as follows:

- Average the vertical displacement of all beam nodes (averaged displacement) computed by the BobKit code (in time domain) to recover the first resonant bending frequency and eliminate the possibility of higher modes interference.

- Apply the "fft" function in MATLAB on the averaged displacement to obtain the frequency response of the system.

6.3 Influence of Parameters on Resonant Behavior of the Granular-Layer/Elastic-Beam (GLEB) System

Basic parameters and materials properties used in the dynamic analysis are the same as quasi-static case, which is given as in Table 5.1 in section 5.2, otherwise specified. According to the 3D dynamic experiment by Kang [46] (page 45), the resonant frequencies for mass ratios (mass of glass beads normalized by mass of circular plate) of 6-10 are in "bending stiffness" regime (Region B) for all particle sizes. Hence, the medium particle size (radius of 1.0 mm) of the close-packed monodispersed particles with mass ratio of 7.54 given in Table 5.2 is reasonably selected for all following subsections. This selection is quite confirmed from our quasi-static analysis in subsection 5.4.3 (see Fig. 5.10) that the resonant frequency falls into the bending stiffness regime particularly when rolling resistance is included in the contact model. The resonant frequency of the GLEB system under small vibration induced by a uniformly distributed load applied to the elastic beam is first studied. From the experiments of vibration of the granular-plate system conducted by Kang [46], it is crucial to examine the amount of the energy input to the system such that the response frequency is in the linear regime. In this simulation, the input energy is measured in term of the driving force which is considered as a uniformly distributed force applied to the bottom elastic beam. Other parameters such as Young's modulus of a particle, friction

between contact interfaces influence in the shift change in the resonant frequency are investigated as well.

6.3.1 Influence of Driving Force Magnitude

A sufficiently large driving force needs to be applied to the elastic lower beam of the GLEB system in order to induce resonance but small enough such that a linear response is obtained (i.e. no separation of significance between the granular layer and the beam). Here, a uniformly distributed force of 4.0, 2.0, 1.5 and 1.0 mN/m with a linearly sweeping frequency over the range 0-100 Hz from 0.5 s to 2.5 s as shown in Fig. 6.1, is tested with rolling resistance ($\mu_r = 0.03$) for a thick granular layer (mass ratio of 7.54) of the close-packed monodispersed particles of radius of 1.0 mm. The nonlinear (Hertzian contact) force model is considered because it is capable for nonlinear contact behavior that the linear (Hookean contact) force model may not. By applying FFT on the averaged displacement in vertical direction of all beam nodes in time domain, the frequency response of the GLEB system is shown in Fig. 6.2.

From Fig. 6.2, the linear behavior with a clear peak of the response is obtained for lower input forces (2.0, 1.5 or 1.0 mN/m) but not for the higher force of 4.0 mN/m. Note that other nonlinear curves are not included in this figure for clarity. Nevertheless, The frequency response obtained from this study is qualitatively similar to the 3D experiments by Kang [46] (page 31). Hence, the driving force of 1.0 mN/m

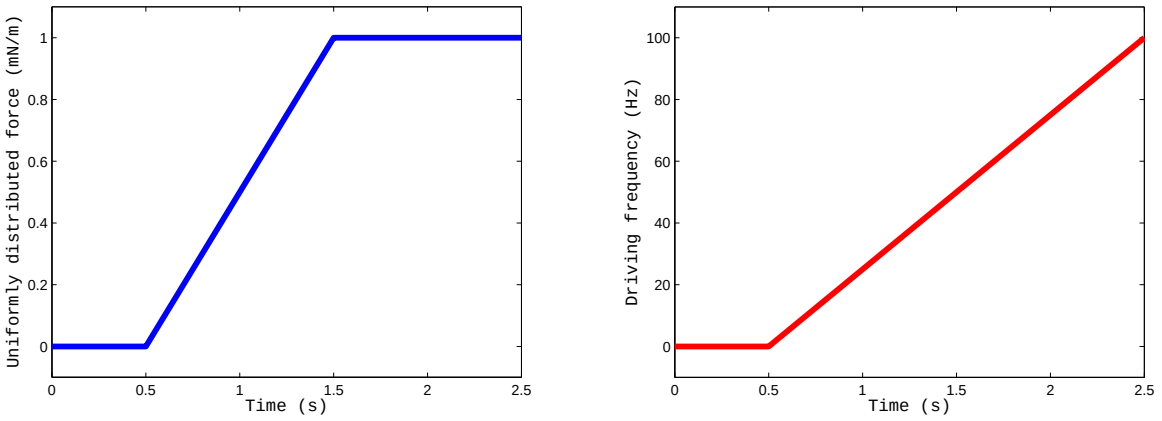

(a) (b)

Figure 6.1: (a) The uniformly distributed driving force, q_0 (force per unit length), as a function of time where the case of q_0 = 1.0 mN/m is shown. (b) The driving frequency as a function of time. The GLEB system is allowed to reach an equilibrium position under its own weight for 0.5 s without any other applied loading for the dynamic analysis.

(800 times smaller than that used in the quasi-static analysis) is selected for all dynamic simulations in this chapter to ensure a linear response of the system. It should be noted that the amount of input energy also depends on how fast/slow to drive the force as well. However, we limit to use the same driving frequency as shown in Fig. 6.1b. for all simulations and this frequency sweep is similar to that used in the experiments of Kang [46].

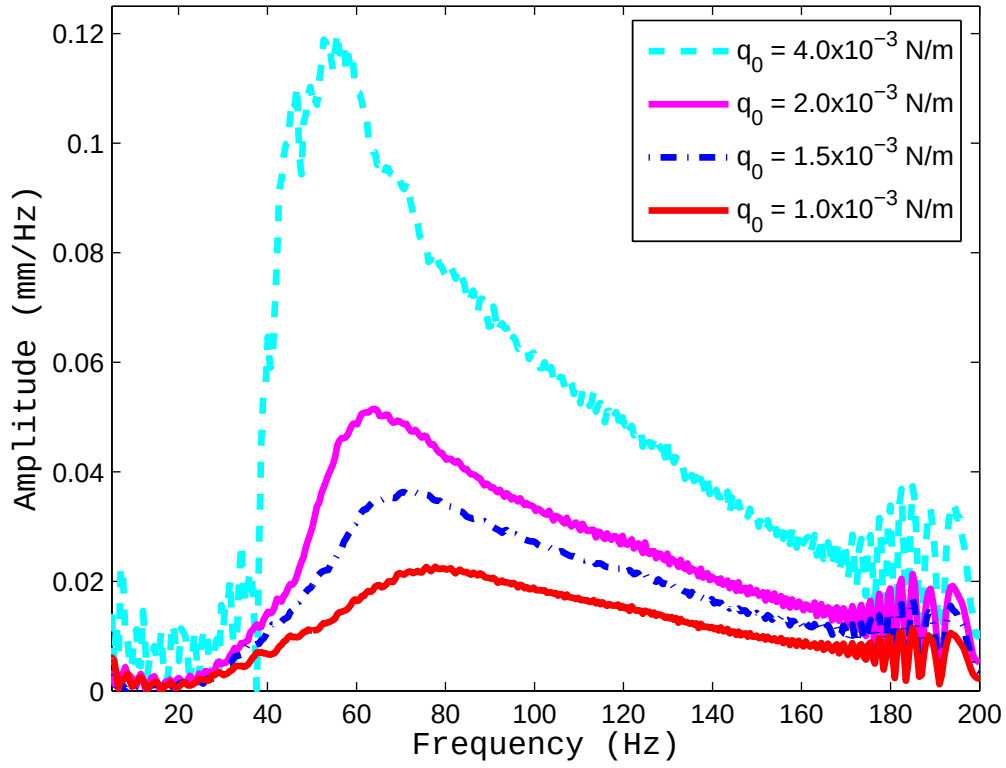

Figure 6.2: The bending resonant behavior of the GLEB system from the 2D dynamic DEM-FEM analysis for a close-packed monodispersed particles (for particle radius of 1.0 mm, particles' Young's modulus of 1 GPa and mass ratio of 7.54). The driving force of 4.0, 2.0, 1.5, and 1.0 mN/m is applied vertically to the elastic bottom beam of the GLEB system. Other nonlinear curves are not shown for clarification; however, the nonlinear behavior is observed as the driving force is high ($q_0 \geq 4$ mN/m). Results are based on the nonlinear (Hertzian contact) force model.

6.3.2 Influence of Linear and Nonlinear Contact Force Models

The influence of using the linear and nonlinear force models in the dynamic resonance analysis is investigated in this subsection. In addition to parameters given in Table 5.1, the close-packed monodispersed particles of radius of 1.0 mm and Young's modulus of particle of 1 GPa for mass ratios of 1.90, 3.77, 7.54 and 11.32 in presence of rolling resistance ($\mu_r = 0.03$) is selected for this test.

Since the amplitude of the frequency response, particularly for the nonlinear (Hertzian contact) force model, for mass ratio of 1.90 is much higher than those of 3.77, 7.54 and 11.32, the frequency response of the smallest mass ratio for the linear (Hookean contact) and nonlinear (Hertzian contact) force models along with the FEM beam is shown separately in Fig. 6.3. Fig. 6.4 shows the frequency response for the linear and nonlinear force models. Note that the 1^{st} resonant frequency of the supporting beam alone is about 89 Hz. From the figures (Fig. 6.3-6.4), it can be seen that, for the particles' Young's modulus of 1 GPa, the frequency response for both linear and nonlinear force models shows resonant behavior of the GLEB system. However, the linear force model (see Fig. 6.4a) is not able to capture the stiffening effect (increasing resonant frequency as the thickness of the granular increases), but the nonlinear force model (see Fig. 6.4b) is able to capture that. This behavior is in contrast to that observed in the quasi-static (slowly applied force) analysis in chapter

5 where the stiffening of the granular layer is noticed for both force models. This leads us to conclude that the nonlinear, Hertzian-type force, which better approximates the real contact of 2D elastic bodies, is able to capture the experimentally observed behavior. Hence, the nonlinear force model is used in analysis of dynamic resonance of the GLEB system.

It should be noted that the frequency response obtained from the nonlinear-type force is qualitatively similar to those observed from the experiments (see Kang [46]); that is, smooth line of the frequency response for small mass ratio (thin layer, see Fig. 6.3) and non-smooth line for large mass ratio (thick layer, see Fig. 6.4b). Compared to the 3D experiments from Kang [46] (page 45) with about the same mass ratio of 7.54, the value of the resonant frequency for particle radius of 1.0 mm as shown in Fig. 6.4b (the normalized value is about 0.87) is in the range of the same glass beads size (GB8: 1.0-1.5 mm). However, from this similar result, we cannot claim that the bending frequency obtained from our 2D simulations is the same as the 3D experiments because it is only one particular data point. Moreover, unclear variation in frequency response observed from the 3D experiments for the glass bead sizes of GB5: 0.3-0.42 mm, GB6: 0.42-0.6 mm, GB7: 0.6-0.85 mm, GB8: 1.0-1.5 mm is observed (see Kang [46], page 45).

For completeness, stiffer particles with Young's modulus of 10 and 100 GPa for mass ratio of 7.54 are used to test using the linear force model. This test is to ensure

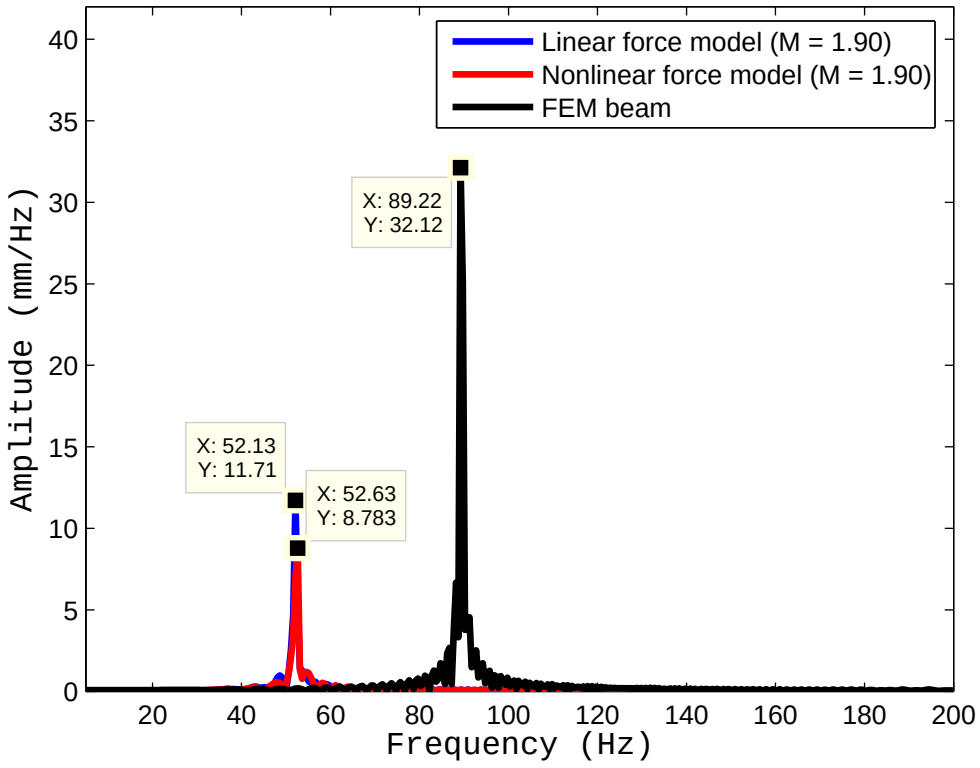

Figure 6.3: The bending resonant behavior of the GLEB system from the 2D dynamic DEM-FEM analysis for a close-packed monodispersed particles (for particle radius of 1.0 mm, particles' Young's modulus of 1 GPa and mass ratio of 1.90) based on linear (in blue) and nonlinear (in red) contact force models. The figure includes the FEM beam alone (in black) where the 1^{st} resonant frequency is about 89 Hz.

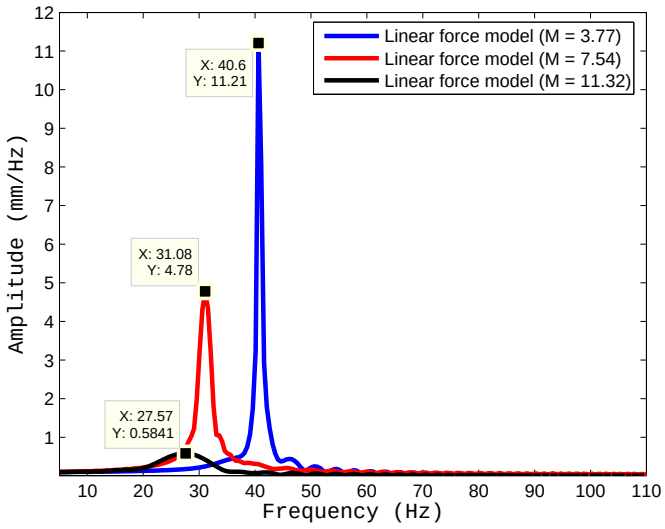

(a)

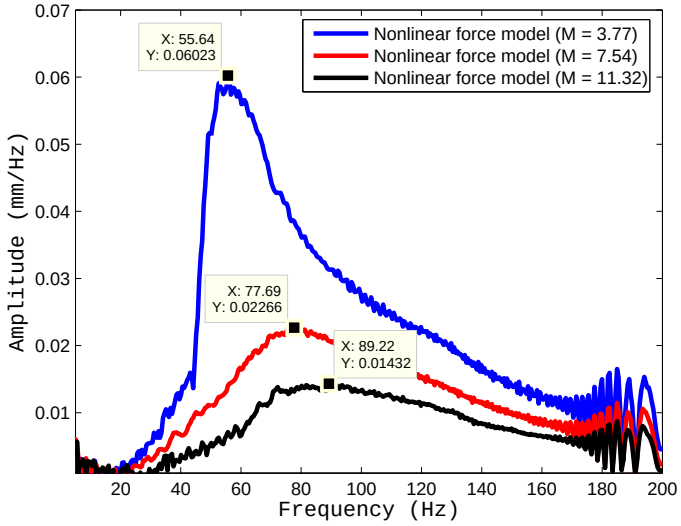

(b)

Figure 6.4: The bending resonant behavior of the GLEB system from the 2D dynamic DEM-FEM analysis for a close-packed monodispersed particles (for particle radius of 1.0 mm, particles' Young's modulus of 1 GPa, and mass ratio of 3.77, 7.54 and 11.32). Results are based on: (a) the linear (Hookean contact) force model, (b) the nonlinear (Hertzian contact) force model.

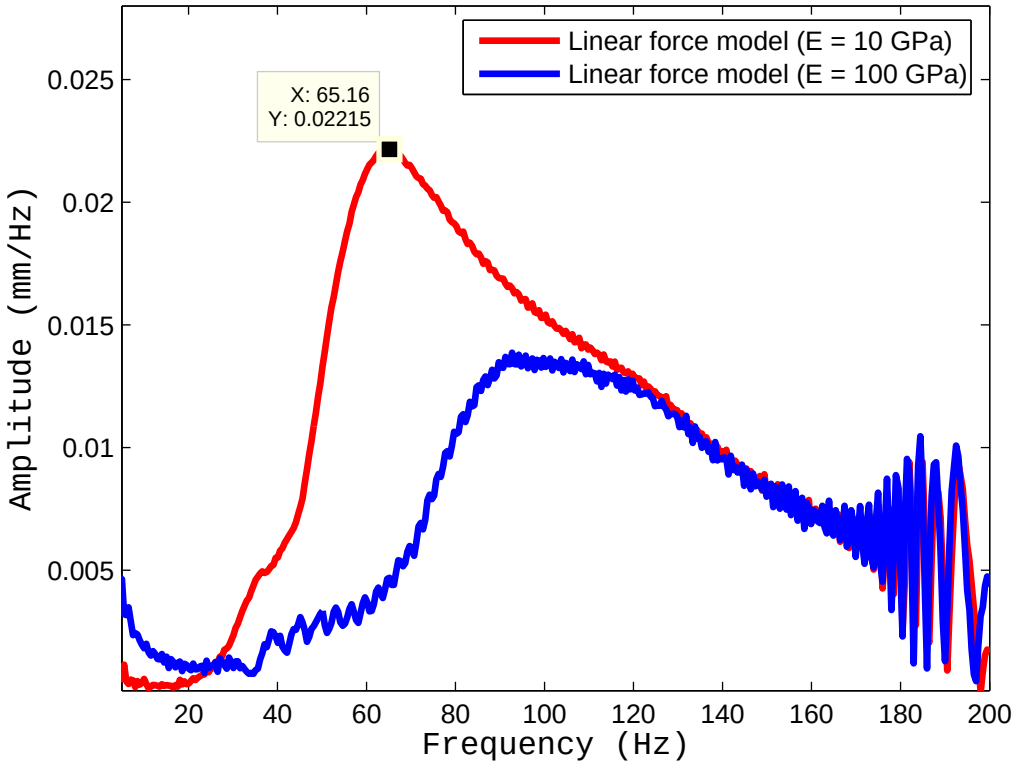

Figure 6.5: The bending resonant behavior of the GLEB system from the 2D dynamic DEM-FEM analysis for a close-packed monodispersed particles (for particle radius of 1.0 mm and mass ratio of 7.54) with Young's modulus of particle of 10 and 100 GPa. Result are based on linear (Hookean contact) force model. Note that the normalized frequency of the clear paek for the Young's modulus of 10 GPa is about 0.73. Hence, the linear force model is able to capture the stiffening effect when stiffer particle is used (typical value of the Young's modulus of the glass beads in the range of 20-70 GPa).

whether or not, for stiffer particles, the linear force model is capable of capturing the stiffening effect of the granular layer. In the limit, the linear model should converge to the nonlinear one so one can expect that, for stiff enough particles, the linear model also captures the stiffening effect. Same parameters are used as in the preceding test except for the particles' Young's modulus of 10 and 100 GPa, respectively. The frequency response is shown in Fig. 6.5. From this figure, we observe that the linear force model is, in fact, able to capture the stiffening effect for a stiff particle. Note that the typical value of the Young's modulus of a granular particles like sand and glass beads is in the range 20-70 GPa. However, other types of particles, like grains, beans, etc. and particles in the pharmaceutical industry are much softer that the particle's Young's modulus value is generally less than 100 MPa (see e.g., Zuo et al. [113]).

It should be emphasized that real material properties should be used for the linear force model, particularly in dynamic analysis of a particle system. Therefore, to compare with the 3D dynamic experiments by Kang [46], the linear model cannot be trusted once the Young's modulus of the particles is below 20 GPa. Thus, the nonlinear force model is more appropriate to use in simulations because it gives a good approximation of real contact behavior for wider range of particles's Young's modulus values.

6.3.3 Influence of Particle's Young Modulus

As discussed in the preceding subsection, the Young's modulus (or simply modulus) of individual granular particles plays an important role in DEM simulations, particularly for the linear contact force model. From a computational point of view, simulations with stiffer particles require smaller time steps as given in Eq. (3.11). From a mechanical point of view, choosing too soft particles results in unrealistic of deformations and contact forces since the Hertz model is a good approximation for relatively stiff particles. Most of dynamic simulations performed in this dissertation use a Young's modulus of 1 GPa which is less than the real value of granular materials like sand and glass beads (20-70 GPa). This value is commonly used in simulation of granular materials in the literature (see e.g., Pöschel and Schwager [81]). Moreover, the modulus value used in the nonlinear model gives the stiffening effect of a granular layer as mentioned in the preceding subsection.

In this subsection, the influence of Young's modulus of granular particle on the resonant behavior of the granular assembly, for the nonlinear (Hertzian contact) force model in presence of rolling resistance along with other parameters given in Table 5.1, is investigated. Both close-packed monodispersed and random-packed polydispersed particles of mass ratio of 7-8 for particle radius of 1.0 mm with five different values of Young's modulus of 10 MPa, 100 MPa, 1 GPa, 10 GPa and 100 GPa are tested.

It is essential to examine whether or not the minimum value of the selected Young's modulus (E = 10 MPa) is valid for the Hertz model. From the equation of normal deformation of the 2D particle in contact given in Eq. (2.31), it is possible to approximate the range of validity for the Hertz model. For small normal force ($P << \pi RE$), Eq. (2.31) leads to $\xi = (P/\pi E)\ln(4R/\xi)$ (see also Gerl and Zippelius [32]). By defining the non-dimensional force λ_f and deformation λ_d such that $\lambda_f = P/\pi\rho g R^2$ (normal force with respect to particle weight) and $\lambda_d = \xi/R$ (normal deformation with respect to particle radius), the valid Young's modulus of the contact particle E for the Hertzian model can be expressed as $E = \rho g R(\lambda_f/\lambda_d)\ln(4/\lambda_d)$ where ρg is the body force of particle per unit cross-sectional area with g, ρ and R denoting the gravitational acceleration, mass density, and radius of particle, respectively. For small deformation, taking $\lambda_d = 0.01$, $\lambda_f = 500$, $g = 9.81$ m/s^2, ρ = 2,600 kg/m^3, R = 1.0 mm, the Young's modulus of the particle is about 7.6 MPa which is below the minimum value used in this subsection (10 MPa).

The resonant frequencies for the two particle systems: close-packed monodispersed and random-packed polydispersed particle with five different values of Young's modulus are shown in the Fig. 6.6. Based on the nonlinear (Hertzian contact) force model, the resonant frequencies of the close-packed monodispersed particles are higher than those of the random-packed polydispersed particles for all given modulus values ranging from 10 MPa up to 100 GPa (see Fig. 6.6). It implies that the layer of the

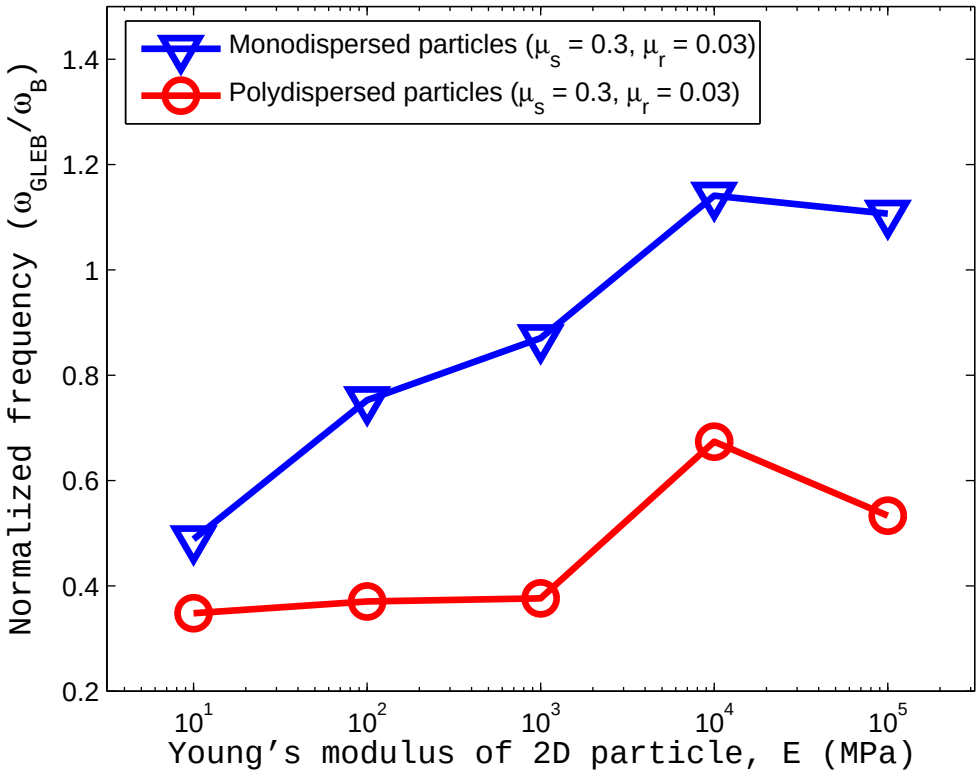

Figure 6.6: The first resonant frequency of the GLEB system from the 2D dynamic DEM-FEM analysis for a close-packed monodispersed (for mass ratio of 7.54) and random-packed polydispersed (for mass ratio of 7.84) particles (for particle radius of 1.0 mm) with five different Young's modulus of 10 MPa, 100 MPa, 1 GPa, 10 GPa, and 100 GPa. Results are based on the nonlinear (Hertzian contact) force model.

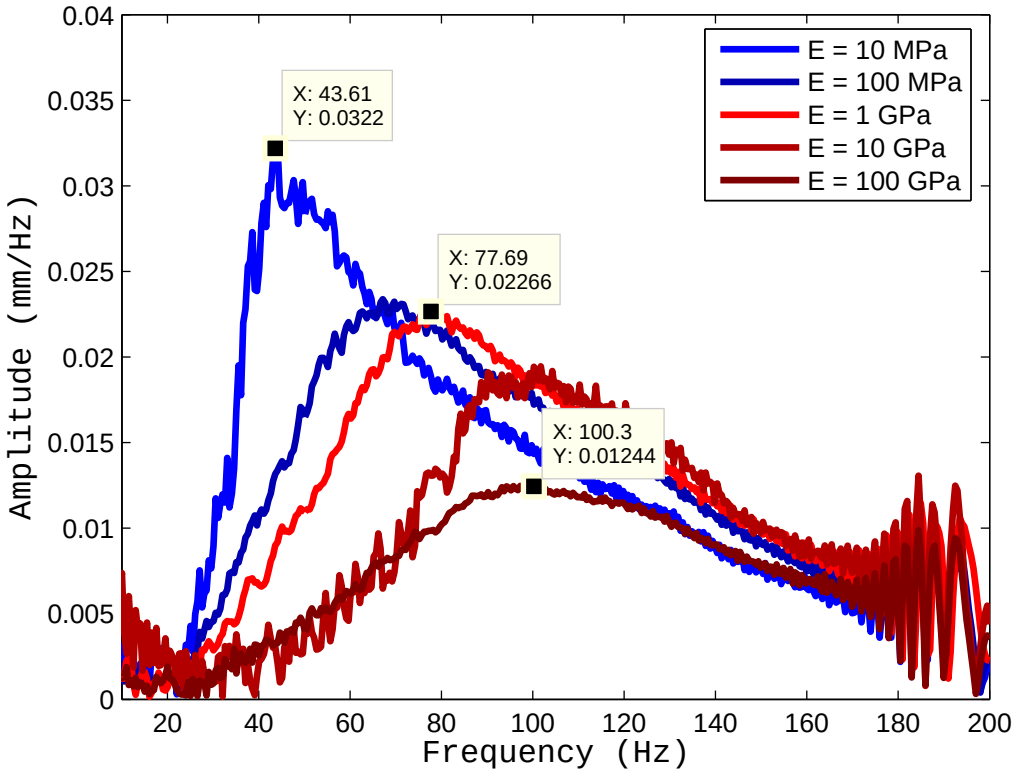

Figure 6.7: The bending resonant behavior of the GLEB system from the 2D dynamic DEM-FEM analysis for a close-packed monodispersed particles (for particle radius of 1.0 mm and mass ratio of 7.54) with five different Young's modulus of 10 MPa, 100 MPa, 1 GPa, 10 GPa, and 100 GPa. Results are based on the nonlinear (Hertzian contact) force model.

close-packed particles is stiffer than the random-packed particles. In Fig. 6.6, for the close-packed monodispered particles, the resonant frequency increases linearly with the particle modulus up to 10 GPa after which it stays more or less constant, and the stiffening effect is observed even for the layer of a soft particle ($E = 10$ MPa). The amplitude-versus-frequency signal of the GLEB system, for the monodispersed particles, for each particle's Young's modulus value is shown in Fig. 6.7 where the peak of the resonant signal corresponding to the modulus of 10 MPa, 1 GPa and 100 GPa is illustrated. The stiffening effect for the polydispersed particles is noticed only for a stiff particle ($E \geq 10$ GPa) where the typical value of the Young's modulus of glass beads is about 20-70 GPa. At this point, it should be emphasized that stiffer particle increases the resonant frequency of the GLEB system for both particle systems (see Fig. 6.6). Moreover, for a given layer thickness, a close-packed monodispersed particles is stiffer than the random-packed polydispersed particles. In the next subsection, the dissipative mechanism in term of sliding and rolling frictions is studied.

6.3.4 Influence of Friction

The effects and influence of sliding and rolling friction between the contact interfaces on the resonant frequency of the GLEB system are studied in this subsection. As a particle rotates upon the contact surfaces, the resisting moment (or rolling resistance) due to rolling friction slows down the particle's rotation and possibly results in

frequency shifting of the GLEB system. Therefore, the rolling friction is also studied. The influence of sliding and rolling frictions on the resonant frequency of the GLEB system for monodispersed and polydispersed particles is studied for the case when the particle radius of 1.0 mm, particles' Young's modulus of 1 GPa, and for mass ratio of 7-8 along with parameters given in Table 5.1. For this test, the sliding friction coefficients of 0.1, 0.3 and 0.5, and rolling resistance coefficients of 0.0 and 0.03 are considered. The shift changes in the resonant frequencies based on the nonlinear (Hertzian contact) force model, are shown in Fig. 6.8.

It is seen that, for monodispersed and polydispersed particles, the sliding friction between contact interfaces influences the shift change in the resonant frequency: higher friction results in a stiffer granular layer, only when the rolling resistance is included in the contact force model (see Fig. 6.8). This is because particles within the layer stick together due to rolling resistance. The stiffening effect due to the increased stiffness is to be expected since, in the limiting case of well bonded particles, the effective stiffness of the granular layer is high (e.g., Kang [46], Kang et al. [47]). The influence is particularly strong for the close-packed monodispersed particles system (see Fig. 6.8a). However, this observation differs from our work in study of resonant behavior of the GLEB system under free vibrations where the rolling resistance plays no role in increasing the resonant frequencies (Rattanadit et al. [85]). In absence of rolling resistance, the sliding friction plays no role in increasing the resonant

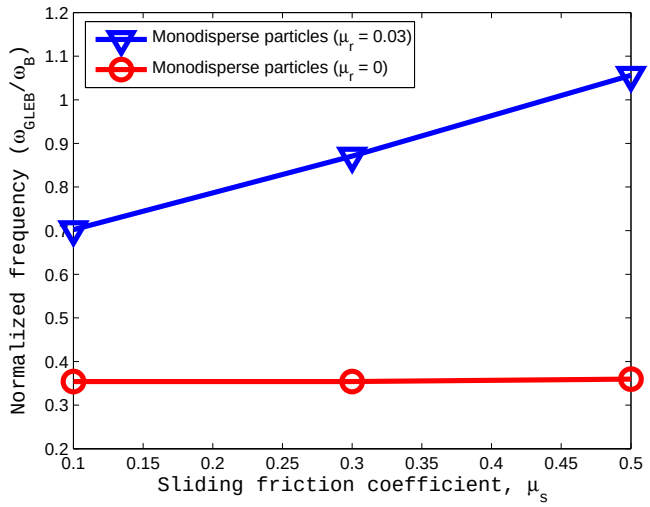

(a)

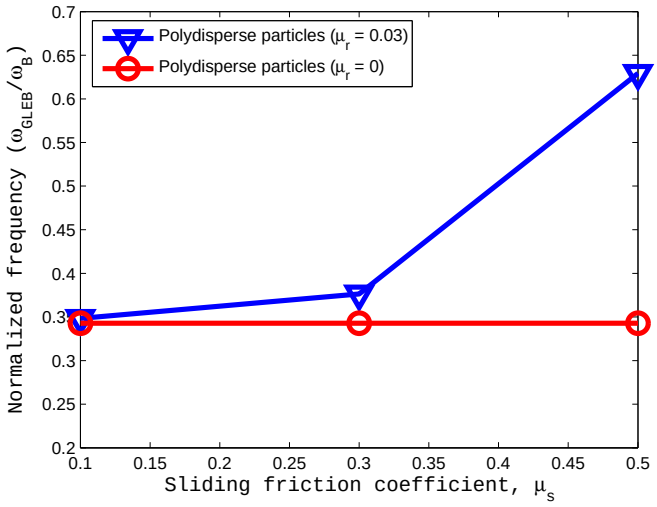

(b)

Figure 6.8: The first resonant frequency of the GLEB system from the 2D dynamic DEM-FEM analysis based on the nonlinear (Hertzian contact) force model (for particle radius of 1.0 mm, particles' Young's modulus of 1 GPa) with different sliding friction ($\mu_s = 0.1, 0.3, 0.5$) and rolling friction ($\mu_s = 0.0, 0.03$). Results shown are: (a) for a close-packed monodispersed particles (for mass ratio of 7.54), (b) for a random-packed polydispersed particles (for mass ratio of 7.84).

frequency of the GLEB system. At this point, it can be concluded that the sliding friction influences in shift changes the resonant frequency if the rolling resistance is included in the contact force model. As a result, the rolling resistance is necessary in DEM simulation for both quasi-static and dynamic analysis and plays an important role in achieving in physically and numerically stable results (e.g., Zhou et al. [110]). At least, the quasi-static analysis in subsection 5.4.4 is confirmed by comparing to the analytical result.

6.4 Resonant Behavior of the GLEB System and Effective Bending Stiffness of the Granular Layer

In this section, the resonant behavior of the Granular-Layer/Elastic-Beam (GLEB) system under small vibration is studied and compared with 3D dynamic experiments by Kang [46] where a circular plate is loaded on top by a glass beads layer and induced by an acoustic wave. For comparison, we select the 3D experimental results for the glass bead sizes of 0.053-0.075 mm (GB1), 0.075-0.106 mm (GB2) and 1.0-1.5 mm (GB8) as shown in Fig. 4.4 in section 4.4. We test for both close-packed monodispersed and random-packed polydispersed particles with the particles' Young's modulus of 1 GPa for different mass ratios. Preparation of the random-packed polydispersed particles is described in section 5.2 where the mean (or average) and standard

Table 6.1: The first resonant frequency (or simply "frequency") of the GLEB system for some selected mass ratios obtained from the 2D dynamic DEM-FEM simulation. Results shown are based on the nonlinear (Hertzian contact) force model with rolling resistance ($\mu_r = 0.03$) for particles' Young's modulus of 1 GPa. Here, "monodispersed particles" and "polydispersed particles" are the short notations for the close-packed monodispersed and random-packed polydispersed particles, respectively. Note that the 1^{st} resonant frequency of the elastic beam is from our FEM analysis 89.22 Hz.

Particle radius, R	Monodispersed particles		Polydispersed particles	
	Mass ratio	Frequency (Hz)	Mass ratio	Frequency (Hz)
R = 1.250 mm	2.38	48.62	2.46	49.12
	4.70	63.66	4.79	37.09
	7.08	82.21	7.36	32.08
	9.41	94.24	9.84	69.17
	11.79	95.74	12.24	72.68
R = 1.000 mm	1.90	52.63	1.98	52.13
	3.77	55.64	3.90	40.60
	5.68	75.19	5.91	34.09
	7.54	77.69	7.84	33.58
	9.45	81.20	9.80	60.65
	11.32	89.22	11.69	70.18
R = 0.625 mm	2.37	50.63	2.47	48.12
	4.73	61.65	4.89	38.10
	7.10	64.66	7.31	32.58
	9.47	76.19	9.76	61.15
	11.83	78.70	12.16	66.17

deviation for each particle size are given in Table 6.2. Here, the nonlinear (Hertzian contact) force model including the rolling resistance ($\mu_r = 0.03$) is considered because this contact force model is capable to capture the stiffening effect especially for the close-packed monodispersed particles system. From the 2D dynamic resonance simulation, the bending resonant frequencies of the GLEB system for some selected mass ratios for each particle size are given in Table 6.1.

Table 6.2: Statistical values of mean and standard deviation (std) from a uniform distribution in particle size (radius, R) in the range [0.8R, 1.2R] for a random-packed polydispersed particles corresponding to each particle size to be used in the 2D DEM-FEM analysis. Here, R_{mean} and R_{std} are the mean (average) and standard deviation of the particle radius, R.

Particle radius, R (mm)	Random-packed polydispersed particles		
	Mass ratio, M	R_{mean} (mm)	R_{std} (mm)
R = 1.250	2.46	1.258	0.176
	4.79	1.252	0.156
	7.36	1.266	0.147
	9.84	1.270	0.147
	12.24	1.265	0.147
R = 1.000	1.98	1.011	0.136
	3.90	1.009	0.120
	5.91	1.013	0.117
	7.84	1.012	0.118
	9.80	1.012	0.115
	11.69	1.010	0.115
R = 0.625	2.47	0.634	0.073
	4.89	0.631	0.072
	7.31	0.630	0.073
	9.76	0.631	0.072
	12.16	0.630	0.072

6.4.1 Resonant Behavior of the GLEB System

The bending resonant frequencies of the Granular-Layer/Elastic-Beam (GLEB) system for intermediate mass ratios beside those given in Table 6.1 can be obtained by fitting the parameters A, B and C of the curve-fit equation proposed by Korman and Sabatier [51] (see Eq. (4.47) in section 4.4). This equation is also used in the 3D dynamic experiments by Kang [46] and Kang et al. [47]. For clarity, the equation is given again as

$$\tilde{\omega} = \sqrt{\frac{A}{M+1} + BM + CM^2}, \tag{6.1}$$

where M denotes the mass ratio and $\tilde{\omega}$ is the normalized resonant frequency (frequency of the GLEB system normalized by the elastic beam). Note that the first term in the equation dominates in the mass-loaded beam (mass dominant regime) whereas the third term dominates in the bending stiffness regime as discussed in section 4.4. As a result, this equation is capable of fitting the bending resonant frequencies over the entire $\tilde{\omega} - M$ curves. The procedure of fitting the first resonant frequencies of the GLEB system from the 2D dynamic DEM-FEM analysis are as follows:

- Apply the "lsqcurvefit" function in MATLAB on the data in Table 6.1 along with the resonant frequency of the elastic beam alone (89.22 Hz) for mass ratio of 0.0 to obtain the parameters A, B and C of the curve-fit equation in Eq.

Table 6.3: The values of fitting parameters A, B, C of the curve-fit equation by Korman and Sabatier [51] for the close-packed monodispersed and random-packed polydispersed particles with three different particle radius of 1.25, 1.0, and 0.625 mm.

Particle radius, R	Monodispersed particles			Polydispersed particles		
	A	B	C	A	B	C
R = 1.250 mm	0.9237	0.0572	0.0041	1.0529	-0.0431	0.0078
R = 1.000 mm	0.9238	0.0652	0.0018	1.0719	-0.0452	0.0076
R = 0.625 mm	0.9551	0.0506	0.0011	1.0344	-0.0330	0.0061

(6.1). The fitting parameters based on the normalized frequencies for each particle size are given in Table 6.3.

- Based on the curve-fit equation with the obtained parameters, the normalized resonant frequencies of the GLEB system from the 2D dynamic DEM-FEM analysis corresponding to the intermediate mass ratios are calculated and shown in Fig. 6.9.

The resonant frequencies for the close-packed monodispersed and random-packed polydispersed particles are shown in Fig. 6.10. For qualitative comparison, the 3D dynamic experiments of glass beads loaded plate system by Kang [46] and the data from Korman and Sabatier [51] are plotted along with the fitting curves from the coupled 2D DEM-FEM results. The fitting parameters obtained from Korman and Sabatier [51] are A = 1.0, B = 0.0078, and C = 0.0004 (see also Kang [46], page 39). In Fig. 6.10, even though it seems to match for the particle radius of 1.25 mm, we do not expect quantitative match between these results due to difference in 2D (disk)

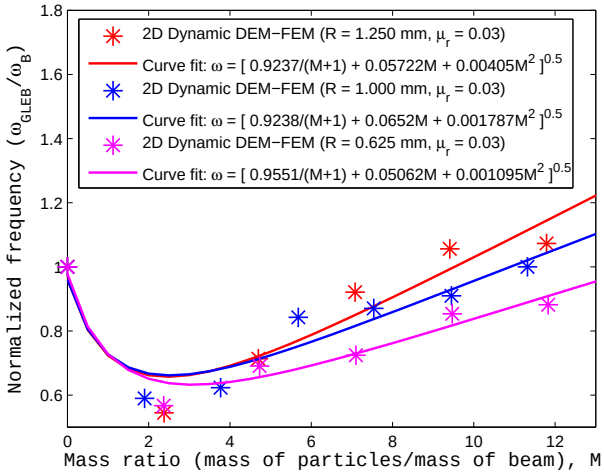

(a)

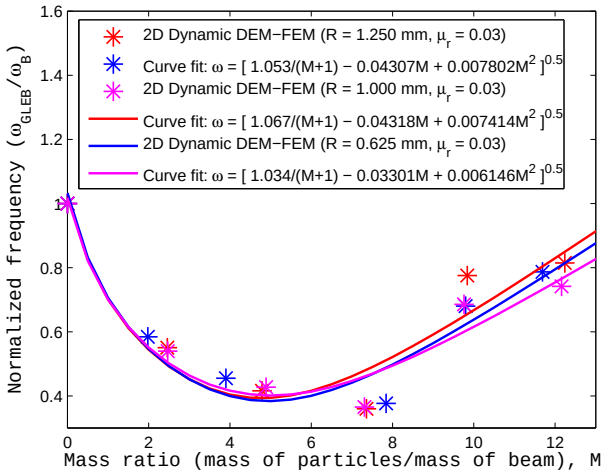

(b)

Figure 6.9: The first resonant frequency of the GLEB system from the 2D dynamic DEM-FEM analysis along with the curve fitting proposed by Korman and Sabatier [51], where the simulation results are given in Table 6.1. Results shown are based on nonlinear spring-dashpot (Hertzian contact) model (for E = 1 GPa, $\mu_s = 0.3$, and $\mu_r = 0.03$), (a) for close-packed monodispersed particles, and (b) for random-packed polydispersed particles.

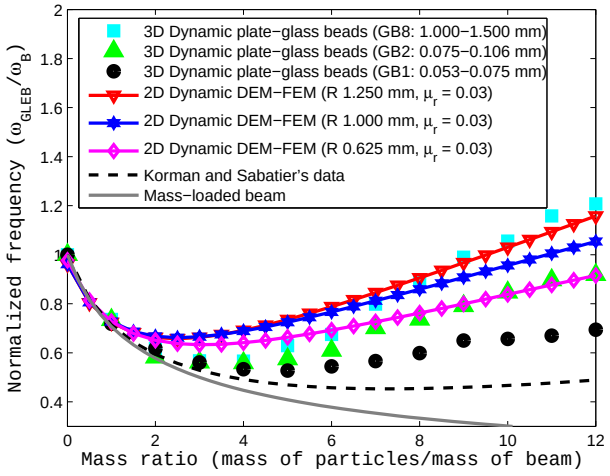

(a)

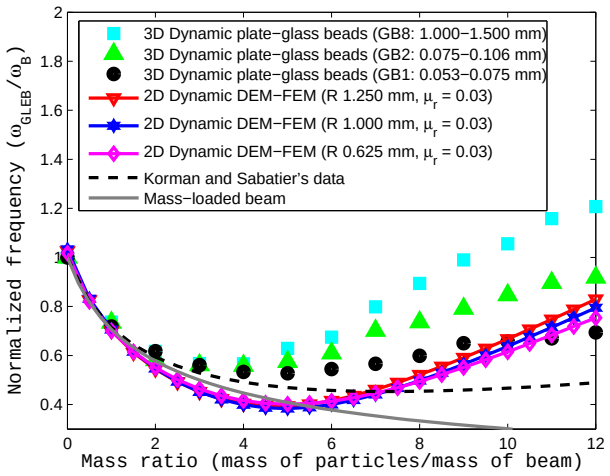

(b)

Figure 6.10: The first resonant frequency from the 2D dynamic DEM-FEM analysis and 3D dynamic plate-glass beads by Kang [46]. Results are obtained based on nonlinear spring-dashpot (Hertzian contact) model (for E = 1 GPa, $\mu_s = 0.3$, and $\mu_r = 0.03$): (a) for close-packed monodispersed particles, and (b) for random-packed polydispersed particles. Note that the dash line is based on Korman and Sabatier's data [51].

and 3D (sphere) Hertzian-type force. Qualitatively, however, the results look very similar particularly in presence of rolling resistance. We notice that, for the same particle size, the resonant frequencies from the 2D dynamic DEM-FEM simulations with the close-packed monodispersed particles show a stiffer layer than measured in the 3D dynamic experiments of the plate-glass beads system from Kang [46], while the random-packed polydispersed systems result in softer (or more compliant) granular layer than seen in the 3D dynamic experiments. Moreover, it should be emphasized that the resonant frequencies from our 2D dynamic DEM-FEM analysis for the close-packed monodispersed show stiffer layer than those of obtained from the 2D quasi-static analysis but softer layer for the random-packed polydispersed particles (see Fig. 5.9c, d and Fig. 6.10 for comparison). At this point, we conclude that our 2D coupled DEM-FEM model is able to capture the resonant behavior of the granular layer observed in the 3D dynamic experiments of the plate-glass beads system (Kang [46]). The effective bending stiffness of the granular layer under small dynamic vibration is investigated in the next section.

6.4.2 The Effective Bending Stiffness of the Granular Layer from Dynamic Resonance Analysis

From section 4.4, the effective bending stiffness of the granular layer $\bar{D}$ with clamped-clamped ends is given by (see Eq. 4.41)

$$\bar{D} = \bar{E}\bar{I} = \bar{\rho}\bar{A}\omega_B^2 \left(\frac{L_b}{\lambda_1}\right)^4, \qquad \lambda_1 = 4.730 \tag{6.2}$$

where $\bar{E}, \bar{I}$, and $\bar{A}$ denote the effective Young's modulus, moment of inertia and cross-sectional area of the beam-layer (GLEB) system, L_b is the length of the beam (same as that of the GLEB system), $\lambda_1 = 4.730$ is the eigenvalue associated with the first bending mode of a clamped beam (see e.g., Kelly [48]), ω_B is the bending resonance of the beam-layer system in region B. The effective bending stiffness of the granular layer computed from the first bending resonance of the GLEB system using Eq. (6.2) is shown in Fig. 6.11. Here, we plot the results obtained from the 2D dynamic DEM-FEM analysis and 3D dynamic experiments of the plate-glass beads system for comparison.

In Fig. 6.11, the dependence of the bending stiffness of the 2D dynamic granular layer on the particle size for both close-packed monodispersed and random-packed polydispersed particles is observed. However, the granular layer for the close-packed monodispersed case is considerably stiffer than an equivalent one computed from the 3D experimental results in the 3D dynamic plate tests (see Kang [46]). In contrast, the granular layer for the case of random-packed polydispersed 2D particles is more

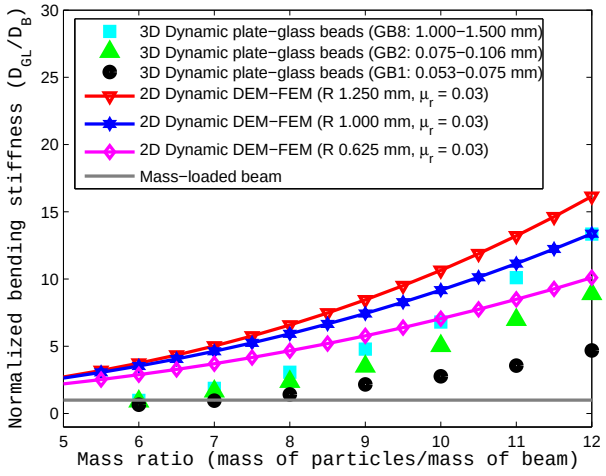

(a)

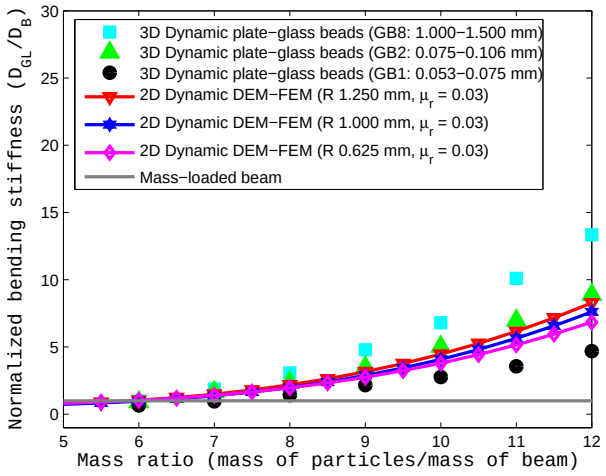

(b)

Figure 6.11: The effective bending stiffness values from the 2D dynamic DEM-FEM analysis and from the 3D dynamic experiments of Kang [46] for vibration of plate loaded with glass beads. The computed effective bending stiffness of the granular layer (or the top beam in the ECB system) is normalized by the bending stiffness of the bottom elastic beam; the experimental results are normalized by the bending stiffness of the supporting plate. Results are obtained based on the nonlinear (Hertzian contact) model: (a) for close-packed monodispersed particles, (b) for random-packed polydispersed particles.

compliant than what is seen from the experiments, and the layer becomes stiffer than the elastic beam alone once the mass ratio becomes larger than about 6 (see Fig. 6.11b). The equivalent bending stiffness for the 2D dynamic granular layer, for the random-packed polydispersed particles, is in the range obtained via the 3D dynamic plate tests (Kang [46]).

6.4.3 Particle-Size Dependence (PSD) of Dynamic Resonance of the Granular Layer

The particle-size dependence (PSD) of the effective bending stiffness of the granular layer is analyzed. The equation giving the PSD is $\sigma = \alpha R^{\beta}$, where σ represents the slope of the resonant frequency versus mass ratio (or thickness) curve in the bending-dominated (or bending stiffness) regime (region B, see Fig. 4.4), obtained from the computational dynamic resonance simulations. It should be noted that the values of the slopes β, in the "bending stiffness" regime obtained from the 3D dynamic experiments is about 0.33 for glass beads layer (see Kang [46], page 46). Kang [46] also derived the dependence of the resonant frequency on particle radius of an random packing of identical elastic spheres under hydrostatic compression, based on Digby's approach (see Digby [22]), and came up with $\beta = 1/6 \simeq 0.17$ (see Kang [46], Kang et al. [47]). In addition, it should be pointed out that the result from our 2D quasi-static DEM-FEM analysis in subsection 5.4.4 ($\beta \simeq 0.78$ for close-packed monodispersed

Table 6.4: The slope of the frequency curves σ obtained from the 2D dynamic DEM-FEM analysis for the close-packed monodispersed and random-packed polydispersed particles with three different particle radii, R, of 1.25, 1.0, and 0.625 mm.

	Particle radius, R	$\sigma(= C^{0.5})$
Close-packed monodispersed particles	R = 1.250 mm	0.0636
	R = 1.000 mm	0.0423
	R = 0.625 mm	0.0331
Random-packed polydispersed particles	R = 1.250 mm	0.0883
	R = 1.000 mm	0.0872
	R = 0.625 mm	0.0784

particles in presence of rolling resistance) matches very well the analytical result in section 4.4 ($\beta = 3/4$ based on best-fit approach). We follow the same procedure as in subsection 5.4.4 except that the first resonant frequency ($\tilde{\omega} - M$) curves are given in subsection 6.4.1. The dependence of the first resonant frequency σ on the particle radius R from the 2D dynamic DEM-FEM analysis for the close-packed monodispersed and random-packed polydispersed particles is shown in Fig. 6.12. Here, the results obtained from the 3D dynamic plate-glass beads are included for comparison. Also, the slopes of frequency curves σ obtained from the 2D dynamic simulation for two particle systems with three different particle sizes are given in Table 6.4.

In Fig. 6.12, the value of the slope β in the bending stiffness regime obtained from the 2D dynamic DEM-FEM simulations with close-packed monodispersed particles is 0.88, and with random-packed polydispersed particles is 0.18. Notice that the β value for the monodispersed particles is larger than those obtained from the 2D quasi-static

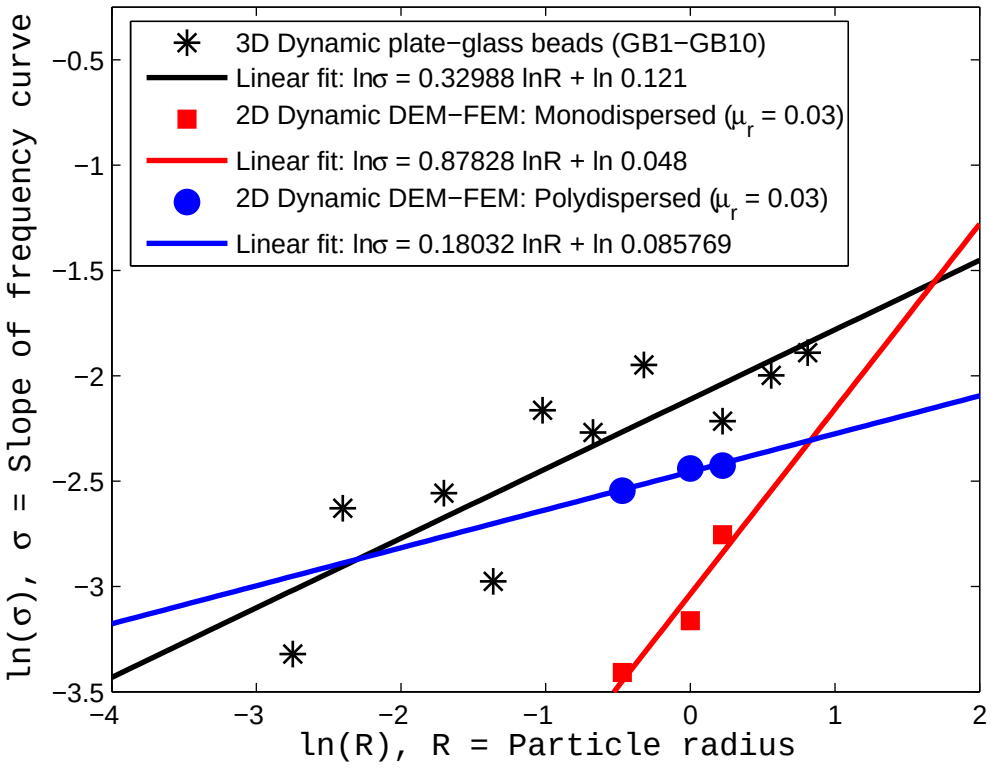

Figure 6.12: The dependence of the bending resonant frequency, σ, on the particle radius R in the "bending stiffness" regime: $\sigma(R) = \alpha R^{\beta}$ from the 2D dynamic DEM-FEM analysis and 3D dynamic plate-glass beads system by Kang [46] for (GB1-GB10). Note that in $\ln\sigma - \ln R$ plot the β value represents the slope of the straight line. The analytical result for 2D disks gives $\beta = 0.75$. Results shown are based on nonlinear spring-dashpot (Hertzian contact) model for the close-packed monodispersed and random-packed polydispersed particles.

DEM-FEM simulation ($\beta = 0.78$) and 2D analytical model ($\beta = 0.75$). This similar discrepancy, with the value from dynamic case being larger than the analytical one, is also observed as in the 3D dynamic plate-glass beads experiments ($\beta = 0.33$ for 3D dynamic experiments, and $\beta = 1/6 \simeq 0.17$ for analytical model). The opposite sense, however, is observed for the case of polydispersed particles. A possible explanation perhaps relates to loss of contact in the bending motion induced by the vibration regime. It is also interesting to notice that the β value of 0.18 for the 2D dynamic DEM-FEM with random-packed polydispersed particles is somewhat similar to the 3D analytical model.

6.5 Summary and Conclusions

In summary, the coupled 2D DEM-FEM simulation is used to analyze the resonant behavior of a granular-layer/elastic-beam GLEB system under small oscillating force. In dynamic analysis, the first resonant frequency of the GLEB system is explicitly obtained by transforming the averaged response amplitude (vertical displacement) of the supporting beam in time domain into the frequency domain using the Fast-Fourier-Transform (FFT). We first study the influence in the magnitude of the driving force to ensure the linear response of the bending resonant behavior. Other parameters such as particle's Young modulus and friction between contacting interfaces

influence in shift/changes in bending resonance are then investigated. The effect of linear (Hookean) and nonlinear (Hertzian) contact force models on the first resonance of the GLEB system is also examined.

For the test of input energy, the function for the driving force and frequency sweep is similar to that used in 3D dynamic experiments by Kang [46]. The nonlinear behavior is observed as increasing in magnitude of the driving force where the bending resonant behavior from the 2D dynamic DEM-FEM simulation is qualitatively similar to the 3D dynamic experiments of the plate-glass beads system. Both linear spring-dashpot (Hookean contact) and nonlinear spring-dashpot (Hertzian contact) force models are able to capture the resonant behavior of the GLEB system, but real material properties are required for the Hookean-type force. The Hertzian-type force gives more realistic contact behavior for a wide range of the particle's Young's modulus (or particle modulus). Increasing in stiffening effect of the 2D granular layer as an individual particle modulus increases, the layer of a close-packed monodispersed particles is stiffer than a random-packed polydispersed particles. Without rolling resistance, sliding friction between contacting interfaces seems not influence on shifting in the first resonant frequency of the GLEB system regardless as structure of the particle packing. In general, in presence of rolling resistance, a granular layer with

high friction is stiffer than those of the low friction value due to well-bonded condition. For the resonant behavior of the GLEB system, an importance is noticed between close-packed monodispersed and random-packed polydispersed particles. The monodispersed particles gives stiffer layer than those obtained from the 3D dynamic experiments by Kang [46] of plate-glass beads system, but softer layer for the polydispersed particles. Similar discrepancy between the measured (dynamic) resonant frequency particle-size dependence of the granular layer and the one predicted by the well-bonded analytical (static) model for 2D and 3D particles are observed. Here, the An explanation of the discrepancy relates to changing in coordinate number due to loss of contact during bending motion of the GLEB system induced by the vibration regime.

Chapter 7

Conclusions and Future Work

A coupled 2D Discrete Element Method-Finite Element Method (DEM-FEM) code called "BobKit" is developed and implemented algorithms and methods for analyzing the behavior of a granular layer interacting with a deforming (quasi-static) and vibrating (dynamic) elastic beam. The code is used to analyze the interaction between 2D granular layers for close-packed monodispersed and random-packed polydispersed particles on top of an elastic support beam. Two different contact force models: linear spring-dashpot (Hookean contact) and nonlinear spring-dashpot (Hertzian contact) models are used and compared. In addition, the effect of rolling resistance due to rolling friction is also investigated. It is crucial that the parameters for both linear and nonlinear models need to be first determined for simulation satisfaction. A new approach to evaluate the damping parameter for the nonlinear force model is proposed and calibrated via a simple test of a dropped particle on to the rigid floor. From this test, the collision time to be used in the linear force model is

obtained as well. The value of the contact time obtained from the test is in the range of typical value to be used in most DEM simulations.

Under quasi-static deformation, the structural changes of the force chains and the resonant behavior of granular layers in a 2D container with an elastic bottom beam are studied. Qualitatively similar results observed from the changing in the structure of the force chains for both contact force models. The system of granular layer on top of an elastic beam is first let to relax by its own weight. A "pyramidal" arch formation is observed from the granular layer for monodispersed packing while for the polydispersed case a dense "brush branches" form. As a uniformly distributed load is applied to the bottom elastic beam in upward direction, destruction and re-formation of reversed arches take place in the contact force chain for both particle packing. At this instant, the contact force intensity against the wall sides is observed and named as the "reversal" of the force chains. This reversal of the force chain leads to the "bending resistance" of the granular layer that was observed in the 3D dynamic experiments under acoustic excitation of the granular on top of an elastic plate, but never explained. The evolution of the force chains during bending deformation forms a region that can lead to enhance convection cells for more effective mixing and segregation in combined shaking/bending-vibrated granular matter. The BobKit code is validated by comparing the particle-size dependence of the bending stiffness of the granular layer with the analytical model from a quasi-static well-bonded particle

system. The comparison shows a vary good match for both contact force models (linear/nonlinear) particularly when the rolling resistance is included. Moreover, similar trends of the bending resonance of the system obtained from 2D quasi-static analysis to the 3D experiments are observed for different particle sizes. As a result, the dynamic analysis is required for further understanding.

In dynamic analysis, a uniformly distributed load is vibrated the bottom elastic beam with varying frequency in time. In explicit dynamic analysis where the resonant frequency of the GLEB system is directly obtained by performing the Fast-Fourier-Transform (FFT) of the time domain signal of the system motion. Even, the 2D coupled DEM-FEM model capture the shift changes in resonant frequencies as in 3D experiments, but they do not match with all the same particle sizes. This due to that fact that the elastic modulus of 2D particle (disk) assembly is higher than the spherical particle case. To obtain the linear response, an enough input energy in term of the driving force and frequency needs to be examined first. Material properties and contact interfaces play important roles in bending stiffness of the granular assembly. Higher Young's modulus of a particle results in stiffer granular layer, particularly for the close-packed monodispersed particles. To be able to capture the bending stiffness of granular layer, the real value of Young's modulus of a particle (E = 20-70 GPa) is required for the linear spring-dashpot model. The shift changes in resonant frequency is observed for the nonlinear (Hertzian contact) force model for

various particle modulus because the Hertzian-type force is able to capture the non-linear contact behavior. Simulation shows significant in rolling resistance to the shift changes in resonant frequency and confirm how it play a significant role in attaining in physically and numerically stable simulations. In presence of rolling resistance, higher friction between contact interfaces results in stiffer granular layer, particularly for the close-packed monodispersed particles. The influences of these parameters in the shift changes in resonant frequencies never explained in the experiments. The particle-size dependence for both particle packing from the 2D dynamic DEM-FEM simulation is obtained but do not match to the 3D dynamic experiments. However, the discrepancy between the dynamic and static results in 2D and in 3D is observed in the similar manner. Note that the particle-size dependence value for the random-packed polydispersed particles is close to the 3D analytical model.

The frequency response for real material properties for a granular particle such Young's modulus (E = 20-70 GPa) is studied in the future work along with effect of various values of friction. The simulation for 3D model will be done in the future work for verification to the existing 3D experiments for both quasi-static and dynamic analysis.

Bibliography

[1] I. Agnolin and N. P. Kruyt. On the elastic moduli of two-dimensional assemblies of disks: Relevance and modeling of fluctuations in particle displacements and rotations. *Computers and Mathematics with Applications*, 55:245–256, 2008.

[2] M. P. Allen and D. J. Tildesley. *Computer Simulation of Liquids*. Oxford, 1987.

[3] S. J. Antony. Link between single-particle properties and macroscopic properties in particulate assemblies: role of structures within structures. *Philosophical Transactions of The Royal Society of London A*, 365:2879–2891, 2007.

[4] J. S. Archer. Consistent mass matrix formulations for structural analysis using finite-element techniques. *Journal of American Institute of Aeronautics and Astronautics*, 3:1910–1918, 1965.

[5] R. J. Bathurst and L. Rothenburg. Micromechanical aspects of isotropic granular assemblies with linear contact interactions. *ASME Journal of Applied Mechanics*, 55:17–23, 1988.

[6] J. Baxter, U. Tuzun, J. Burnell, and D. M. Heyes. Granular dynamics simulations of two-dimensional heap formation. *Physical Review E*, 55:3546–3554, 1997.

[7] F. P. Beer and E. R. Johnston. *Mechanics for Engineers-Statics and Dynamics*. MacGraw-Hill, 1976.

[8] N. Bell, Y. Yu, and P. J. Mucha. Particle-based simulation of granular materials. In Anjyo K. and Faloutsos P., editors, *Symposium on Computer Animation*, pages 77–86. ACM, 2005.

[9] F. Bobaru, K. Promratana, K. Rattanadit, and J. A. Turner. Enhancing mixing in granular matter via combined vertical shaking and bending vibrations. *in preparation*, 2009.

[10] N. V. Brilliantov and T. Pöschel. Rolling friction of a viscous sphere on a hard plane. *Europhysics Letters*, 42:511–516, 1998.

[11] N. V. Brilliantov, F. Spahn, J. M. Hertzsch, and T. Pöschel. Model for collisions in granular gases. *Physical Review E*, 53:5382–5392, 1996.

[12] V. Buchholtz and T. Pöschel. A vectorized algorithm for molecular-dynamics of short-range interacting particles. *International Journal of Modern Physics C-Physics and Computers*, 4:1049–1057, 1993.

[13] C. S. Campbell. Computer simulation of powder flows. In Gotoh K., Masuda H., and Higashitani K., editors, *Powder Technology Handbook*, pages 777–793. Dekker, 2 edition, 1997.

[14] C. S. Campbell. Granular material flows-an overview. *Powder Technology*, 162:208–229, 2006.

[15] C. S. Chang and C. L. Liao. Estimates of elastic modulus for media of randomly packed granules. *Applied Mechanics Reviews*, 47:S197–S206, 1994.

[16] C. S. Chang, S. S. Sundaram, and A. Misra. Initial moduli of particulated mass with frictional contacts. *International Journal for Numerical and Analytical Methods in Geomechanics*, 13:626–641, 1989.

[17] P. W. Cleary. Predicting charge motion, power draw, segregation and wear in ball mills using discrete element methods. *Minerals Engineering*, 11:1061–1080, 1998.

[18] P. W. Cleary and M. L. Sawley. DEM modelling of industrial granular flows: 3D case studies and the effect of particle shape on hopper discharge. *Applied Mathematical Modelling*, 26:89–111, 2002.

[19] P. A. Cundall and O. D. L. Strack. A discrete numerical model for granular assemblies. *Geotechnique*, 29:47–65, 1979.

[20] P.A Cundall and R. D. Hart. Numerical modeling of discontinua. *Engineering Computations*, 9:101–113, 1992.

[21] H. Deresiewicz. Stress-strain relations for a simple model of a granular medium. *Journal of Applied Mechanics*, 25:402–406, 1958.

[22] P. J. Digby. The effective elastic moduli of porous granular rocks. *Journal of Applied Mechanics*, 48:803–808, 1981.

[23] S. N. Domenico. Elastic properties of unconsolidated porous sand reservoirs. *Geophysics*, 42:13391368, 1977.

[24] D. Donskoy. Nonlinear vibro-acoustic technique for land mine detection. *SPIE's Proceedings on Detection and Remediation Technologies for Mines and Minelike Targets III*, 3392:211–217, 1998.

[25] D. Donskoy and A. Ekimov. Nonlinear vibrations of buried landmines. *Journal of the Acoustical Society of America*, 117:690–700, 2005.

[26] D. Donskoy, A. Ekimov, N. Sedunov, and M. Tsionskiy. Nonlinear seismo-acoustic land mine detection and discrimination. *Journal of the Acoustical Society of America*, 111:2705–2714, 2002.

[27] J. Duffy and R. D. Mindlin. Stress-strain relations and vibrations of granular medium. *Journal of Applied Mechanics*, 24:1957, 585-593.

[28] F. Emeriault, B. Cambou, and A. Mahboubi. Homogenization for granular materials: non reversible behaviour. *Mechanics of Cohesive-Frictional Materials*, 1:199–218, 1996.

[29] E. Falcon, C. Laroche, S. Fauve, and C. Coste. Behavior of one inelastic ball bouncing repeatedly off the ground. *European Physical Journal B*, 3:45–57, 1998.

[30] E. Frangin, P. Marin, and L. Daudeville. On the use of combined finite/discrete element method for impacted concrete structures. *Journal de Physique IV*, 134:461–466, 2006.

[31] C. W. Gear. *Numerical Initial Value Problems in Ordinary Differential Equations*. Prentice-Hall, 1971.

[32] F. Gerl and A. Zippelius. Coefficient of restitution for elastic disks. *Physical Review E*, 59:2361–2372, 1999.

[33] D. T. Gethin, X. S. Yang, and R. W. Lewis. A two dimensional combined discrete and finite element scheme for simulating the flow and compaction of systems comprising irregular particulates. *Computer Methods in Applied Mechanics and Engineering*, 195:5552–5565, 2006.

[34] D. T. Greenwood. *Advanced Dynamics*. Cambridge University Press, 2006.

[35] P. K. Haff and B. T. Werner. Computer simulation of the mechanical sorting of grains. *Powder Technology*, 48:1986, 239-245.

[36] K. Han, D. Peric, A. J. L. Crook, and D. R. J. Owen. A combined finite-discrete element simulation of shot peening processes, Part I: studies on 2D interaction laws. *Engineering Computations*, 17:593–619, 2000a.

[37] K. Han, D. Peric, D. R. J. Owen, and J. Yu. A combined finite-discrete element simulation of shot peening processes, Part II: 3D interaction laws. *Engineering Computations*, 17:680–702, 2000b.

[38] M. S. Han, H. Benaroya, and T. Wei. Dynamics of transversely vibrating beams using four engineering theories. *Journal of Sound and Vibration*, 225:935–988, 1999.

[39] H. Hertz. Über die Berührung fester elastische Körper (on the contact of rigid elastic solids). *J. reine und angewandte Mathematik*, 92:1882a, 156-171.

[40] E. Hinton, T. Rock, and O. Zienkiewicz. A note on mass lumping and related processes in the finite element method. *International Journal of Earthquake Engineering and Structural Engineering*, 4:245–249, 1976.

[41] T. Iwai, C. W. Hong, and P. Greil. Fast particle pair detection algorithms for particle simulations. *International Journal of Modern Physics C*, 10:823–837, 1999.

[42] K. Iwashita and M. Oda. Micro-deformation mechanism of shear banding process based on modified distinct element method. *Powder Technology*, 109:192–205, 2000.

[43] J. Jenkins, D. Johnson, L. LaRagione, and H. Makse. Fluctuations and the effective moduli of an isotropic, random aggregates of identical, frictionless spheres. *Journal of the Mechanics and Physics of Solids*, 53:197225, 2005.

[44] S. Ji and H. H. Shen. Effect of contact force models on granular flow dynamics. *Journal of Engineering Mechanics*, 132:1252–1259, 2006.

[45] K. L. Johnson. *Contact Mechanics*. Cambridge University Press, 1985.

[46] W. Kang. Vibration of plates loaded with granular materials. Master's thesis, University of Nebraska-Lincoln, 2006.

[47] W. Kang, J. A. Turner, F. Bobaru, L. Yang, and K. Rattanadit. Granular layers on vibrating plates: Effective bending stiffness and particle-size effects. *Journal of the Acoustical Society of America*, 121:888–896, 2007.

[48] S. G. Kelly. *Fundamentals of Mechanical Vibrations*. McGraw-Hill, 2^{nd} edition, 2000.

[49] P. Komodromos. A simplified updated lagrangian approach for combining discrete and finite element methods. *Computational Mechanics*, 35:305–313, 2005.

[50] P. Komodromos and R. Williams. Dynamic simulation of multiple deformable bodies using combined discrete and finite element methods. *Engineering Computations*, 21:431–448, 2004.

[51] S. Korman and J. M. Sabatier. Nonlinear acoustic techniques for landmine detection. *Journal of the Acoustical Society of America*, 116:33543369, 2004.

[52] H. Kruggel, E. Simsek, S. Rickelt, S. Wirtz, and V. Scherer. Review and extension of normal force models for the discrete element method. *Powder Technology*, 171:157–173, 2007.

[53] N. P. Kruyt and L. Rothenburg. Kinematic and static assumptions for homogenization in micromechanics of granular materials. *Mechanics of Materials*, 36:1157–1173, 2004.

[54] A. Kudrolli. Size separation in vibrated granular matter. *Reports on Progress in Physics*, 67:209–247, 2004.

[55] H. P. Kuo, P. C. Knight, D. J. Parker, Y. Tsuji, M. J. Adams, and J. P. K. Seville. The influence of DEM simulation parameters on the particle behaviour in a V-mixer. *Chemical Engineering Science*, 57:3621–3638, 2002.

[56] G. Kuwabara and K. Kono. Restitution coefficient in a collision between two spheres. *Japanese Journal of Applied Physics*, 26:12301233, 1987.

[57] Y. Kwon and H. Bang. *The Finite Element Method Using Matlab*. CRC Press, 1997.

[58] L. Labous, A. D. Rosato, and R. N. Dave. Measurements of collisional properties of spheres using high-speed video analysis. *Physical Review E*, 56:5717–5725, 1997.

[59] P. A. Langston and U. Tuzun. Continuous potential discrete particle simulations of stress and velocity fields in hoppers: transition from fluid to granular flow. *Chemical Engineering Science*, 49:1259–1275, 1994.

[60] P. A. Langston, U. Tuzun, and D. M. Heyes. Discrete element simulation of granular flow in 2D and 3D hoppers: Dependence of discharge rate and wall stress on particle interactions. *Chemical Engineering Science*, 50:967–987, 1995.

[61] S. Lee, W. Scott, J. Martin, G. Larson, and G. McCall. Technical issues associated with the detection of buried land mines with high-frequency seismic waves.

SPIE's Proceedings on Detection and Remediation Technologies for Mines and Minelike Targets VII, 4742:617–628, 2002.

[62] R. W. Lewis, D. T. Gethin, X. S. Yang, and R. C. Rowe. A combined finite-discrete element method for simulating pharmaceutical powder tableting. *International Journal for Numerical Methods in Engineering*, 62:853–869, 2005.

[63] C. L. Liao, T. C. Chan, A. S. J. Suiker, and C. S. Chang. Pressure-dependent elastic moduli of granular assemblies. *International Journal for Numerical and Analytical Methods in Geomechanics*, 24:265–279, 2000.

[64] C. L. Liao, T. P. Chan, D. H. Young, and C. S. Chang. Stress-strain relationships for granular materials based on the hypothesis of best fit. *International Journal of Solids and Structures*, 34:4087–4100, 1997.

[65] S. Luding. Stress distribution in static two-dimensional granular model media in the absence of friction. *Physical Review E*, 55:4720–4729, 1997.

[66] M. Madadi, O. Tsoungui, M. Lätzel, and S. Luding. On the fabric tensor of polydisperse granular materials in 2d. *International Journal of Solids and Structures*, 41:25632580, 2004.

[67] H. A. Makse, N. Gland, D. L. Johnson, and L. M. Schwartz. Why effective medium theory fails in granular materials. *Physical Review Letters*, 83:5070–5073, 1999.

[68] L. E. Malvern. *Introduction to the Mechanics of a Continuous Medium*. Prentice-Hall, 1969.

[69] L. Meirovitch. *Elements of Vibration Analysis*. McGraw-Hill, 1986.

[70] J. H. Michell. Some elementary distributions of stress in three dimensions. *Proceedings of the London Mathematical Society*, 32:23–61, 1900.

[71] R. D. Mindlin. Compliance of elastic bodies in contact. *ASME Journal of Applied Mechanics*, 16:259–268, 1949.

[72] R. D. Mindlin and H. Deresiewicz. Elastic spheres in contact under varying oblique forces. *ASME Journal of Applied Mechanics*, 20:327–344, 1953.

[73] B. K. Mishra. A review of computer simulation of tumbling mills by the discrete element method: Part 1-contact mechanics. *International Journal of Mineral Processing*, 71:73–93, 2003.

[74] W. A. Morgado and I. Oppenheim. Energy dissipation for quasielastic granular particle collisions. *Physical Review E*, 55:1940–1945, 1997.

[75] A. Munjiza. *The Combined Finite-Discrete Element Method*. Wiley, 2004.

[76] N. M. Newmark. A method of computation for structural dynamics. *Journal of Engineering Mechanics Division, Proceeding of ASCE*, 85:67–94, 1959.

[77] M. L. Oelze, W. D. O'Brien, and R. G. Darmody. Measurement of attenuation and speed of sound in soils. *Soil Science Society of America Journal*, 66:788–796, 2002.

[78] E. Onate and J. Rojek. Combination of discrete element and finite element methods for dynamic analysis of geomechanics problems. *Computer Methods in Applied Mechanics and Engineering*, 193:3087–3128, 2004.

[79] N. Petrinic. *Aspects of discrete element modeling involving facet-to-facet contact detection and interaction*. PhD thesis, University of Wales, Swansea, 1996.

[80] H. Poritsky. Stresses and deflections of cylindrical bodies in contact with application to contact of gears and locomotive wheels. *Journal of Applied Mechanics*, 17:191–201, 1950.

[81] T. Pöschel and T. Schwager. *Computational Granular Dynamics: Models and Algorithms*. Springer-Verlag, 2005.

[82] A. L. Quiniou and F. Rioual. Flow of a particle along a rotating wall. *Europhysics Letters*, 82:34001–p1–p6, 2008.

[83] R. Ramírez, T. Pöschel, N. V. Brilliantov, and T. Schwager. Coefficient of restitution of colliding viscoelastic spheres. *Physical Review E*, 60:4465–4472, 1999.

[84] S. S. Rao. *Mechanical Vibrations*. Addison-Wesley, 1995.

[85] K Rattanadit, F Bobaru, K Promratana, and J. A. Turner. Force chains and resonant behavior in bending of a granular layer on an elastic support. *Mechanics of Materials*, 41:691–706, 2009.

[86] J. N. Reddy. *An Introduction to the Finite Element Method*. Tata McGraw-Hill, 2003.

[87] A. D. Renzo and F. P. Maio. Comparison of contact force models for the simulation of collisions in DEM based granular flow codes. *Chemical Engineering Science*, 59:525–541, 2004.

[88] J. Sabatier and N. Xiang. Laser-doppler based acoustic-to-seismic detection of buried mines. *SPIE's Proceedings on Detection and Remediation Technologies for Mines and Minelike Targets IV*, 3710:215–222, 2003.

[89] J. Schafer, S. Dippel, and D. E. Wolf. Force schemes in simulations of granular materials. *Journal de Physique I*, 6:5–20, 1996.

[90] T. Schwager. Coefficient of restitution for viscoelastic disks. *Physical Review E*, 75.

[91] T. Schwager and T. Pöschel. Coefficient of normal restitution of viscous particles and cooling rate of granular gases. *Physical Review E*, 57:650–654, 1998.

[92] W. Scott, S. Lee, G. Larson, J. Martin, and G. McCall. Use of high-frequency seismic waves for the detection of buried land mines. *SPIE's Proceedings on Detection and Remediation Technologies for Mines and Minelike Targets VI*, 4394:543–552, 2001.

[93] L. G. Sebastian and V. Luis. Discrete element method evaluation of granular crushing under direct shear test conditions. *Journal of Geotechnical and Geoenvironmental Engineering*, 131:1295–1300, 2005.

[94] R. Sondergaard, K. Chaney, and C. E. Brennen. Measurements of solid spheres bouncing off flat plates. *Journal of Applied Mechanics*, 57:694–699, 1990.

[95] Y. Taguchi. New origin of convective motion: elastically induced convection in granular materials. *Physical Review Letters*, 69:1367–1370, 1992.

[96] P. A. Thompson and G. S. Grest. Granular flow: friction and the dilatancy transition. *Physical Review E*, 67:1751–1754, 1991.

[97] W. Thomson. *Theory of Vibration with Applications*. Prentice Hall, 1993.

[98] C. Thornton and C. W. Randall. Applications of theoretical contact mechanics to solid particle system simulation. In Satake M. and Jenkins J. T., editors, *Micromechanics of granular materials*, volume 20, pages 133–142. Elsevier Science, 1988.

[99] C. Thornton and K. K. Yin. Impact of elastic spheres with and without adhesion. *Powder Technology*, 65:153–166, 1991.

[100] E. Tijskens, H. Ramon, and J. Baerdemaeker. Discrete element modeling for process simulation in agriculture. *Journal of Sound and Vibration*, 266:493–514, 2003.

[101] S. Timoshenko. On the transverse vibrations of bars of uniform cross-section. *Philosophical Magazine*, 125, 1922.

[102] K. Walton. The effective elastic moduli of a random packing of spheres. *Journal of the Mechanics and Physics of Solids*, 35:213–226, 1987.

[103] N. Xiang and J. M. Sabatier. An experimental study on antipersonnel landmine detection using acoustic-to-seismic coupling. *Journal of the Acoustical Society of America*, 113:1333–1341, 2003.

[104] R. Xu and Y. Wu. Static, dynamic, and buckling analysis of partial interaction composite members using timoshenko's beam theory. *International Journal of Mechanical Sciences*, 49:1139–1155, 2007.

[105] K. Yamane. Discrete-element method application to mixing and segregation model in industrial blending system. *Journal of Materials Research*, 19:623–627, 2004.

[106] T. Yanagida, A. J. Matchett, B. N. Asmar, P. A. Langston, J. K. Walters, and J. M. Coulthard. Dynamic response of well-mixed binary particulate systems subjected to low magnitude vibration. *Advanced Powder Technology*, 14:589–604, 2003.

[107] R. Y. Yang, R. P. Zou, and A. B. Yu. Computer simulation of the packing of fine particles. *Physical Review E*, 62:3900–3908, 2000.

[108] A. Zagrai, D. Donskoy, and A. Ekimov. Resonance vibrations of buried landmines. *SPIE's Proceedings on Detection and Remediation Technologies for Mines and Minelike Targets IX*, 5415:21–29, 2004.

[109] D. Zhang and W. J. Whiten. The calculation of contact forces between particles using spring and damping models. *Powder Technology*, 88:59–64, 1996.

[110] Y. C. Zhou, B. D. Wright, R. Y. Yang, B. H. Xu, and A. B. Yu. Rolling friction in the dynamic simulation of sandpile formation. *Physica A*, 269:536–553, 1999.

[111] Y. C. Zhou, B. H. Xu, R. P. Zou, A. B. Yu, and P. Zulli. Stress distribution in a sandpile formed on a deflected base. *Advanced Powder Technology*, 14:401–410, 2003.

[112] H. P. Zhu and A. B. Yu. A theoretical analysis of the force models in discrete element method. *Powder Technology*, 161:122–129, 2006.

[113] S. C. Zuo, Y. Xu, Q. W. Yang, and Y. T. Feng. Discrete element simulation of the behavior of bulk granular material during truck braking. *Engineering Computations: International Journal for Computer-Aided Engineering and Softwar*, 23:4–15, 2006.

Appendix A

Normal Deformation of Two Similar Elastic Disks

Normal deformation of two similar elastic disks in contact as shown in Fig. A.1 is given by

$$\xi = 2R - 2\sqrt{R^2 - a^2} = 2R - 2R\sqrt{1 - \left(\frac{a}{R}\right)^2}, \tag{A.1}$$

where ξ is the normal deformation (particle overlap), R is the particle radius, a is the contact radius (contact width). Rearranging the Eq. (A.1) leads to

$$4R^2\left[1 - \left(\frac{a}{R}\right)^2\right] = 4R^2 - 4R\xi + \xi^2. \tag{A.2}$$

For small deformation ($\xi << R$) where the last term on the right-hand side is dropped out, the normal deformation can be approximated as

$$\xi = \frac{a^2}{R}. \tag{A.3}$$

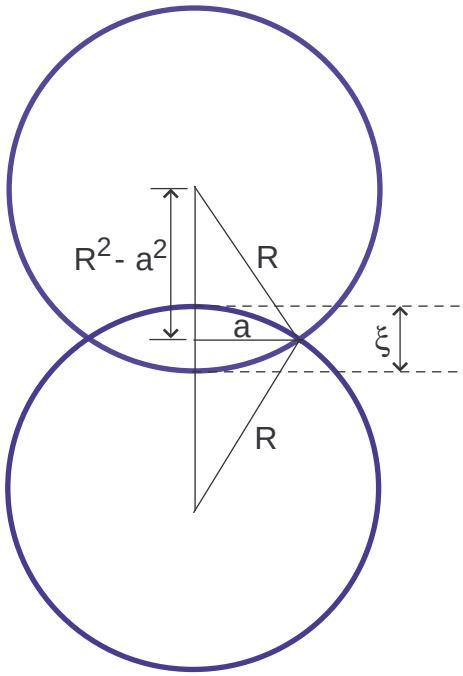

Figure A.1: Normal deformation of two similar elastic disks in contact.

Appendix B

FEM Formulation of Euler-Bernoulli Beam Bending

The finite element (FE) in space x for a fixed time $t > 0$ can be formulated from the partial differential equation of the beam in Eq.(3.36) by using the method of weighted residual (Galerkin's method). This formulation results in a system of algebraic ordinary differential equations. The averaged weighted residual of Eq.(3.36) leads to

$$I = \int_0^L \left(\rho A \frac{\partial^2 u}{\partial t^2} + EI \frac{\partial^4 u}{\partial x^4} - f \right) w dx = 0, \tag{B.1}$$

where w is the weight (test) function and L is the length of the beam. The weak formulation of Eq.(B.1) is obtained by integrating the second term twice to distribute the spatial derivatives equally between the weight function w and the dependent variable v together with discretization of the beam into a number of finite beam

elements. Thus,

$$I = \sum_{e=1}^{n} \left[\int_{\Omega_e} \rho A \frac{\partial^2 u}{\partial t^2} w dx + \int_{\Omega_e} EI \frac{\partial^2 u}{\partial x^2} \frac{\partial^2 w}{\partial x^2} dx - \int_{\Omega_e} f w dx \right] + \left[Vw - M \frac{\partial w}{\partial x} \right]_0^L = 0, \tag{B.2}$$

where $V(x) = V_x = EI\frac{\partial^3 u}{\partial x^3}$ denotes the shear force, $M(x) = M_x = EI\frac{\partial^2 u}{\partial x^2}$ is the bending moment, Ω_e is the beam element domain, and n is the number of discretized elements of the beam. Here, the independent variables x and t are left out for simplicity. It can be seen that there are two boundary expressions from the integration by parts as in the second bracket in Eq.(B.2). Then, the weak form of the differential equation can be written as

$$B(w, u, t) - l(w, t) = 0, \tag{B.3}$$

where

$$\begin{aligned} B(w, u, t) &= \sum_{e=1}^{n} \left[\int_{\Omega_e} \left(\rho A w \frac{\partial^2 u}{\partial t^2} + EI \frac{\partial^2 w}{\partial x^2} \frac{\partial^2 u}{\partial x^2} \right) dx \right], \\ l(w, t) &= \sum_{e=1}^{n} \left(\int_{\Omega_e} w f dx \right) + V_0 w_0 + V_L w_L + M_0 \left(-\frac{\partial w_0}{\partial x} \right) + M_L \left(-\frac{\partial w_L}{\partial x} \right), \end{aligned} \tag{B.4}$$

with the boundary conditions:

$$\begin{aligned} V_0 &= EI \frac{\partial^3 u_0}{\partial x^3}, \\ M_0 &= EI \frac{\partial^2 u_0}{\partial x^2}, \\ V_L &= -EI \frac{\partial^3 u_L}{\partial x^3}, \\ M_L &= -EI \frac{\partial^2 u_L}{\partial x^2}. \end{aligned} \tag{B.5}$$

For small time step size, the solution $u(x,t)$ can be approximated by

$$u(x,t) = \sum_{j=1}^{N} u_j^e(t)\psi_j^e(x), \tag{B.6}$$

where N is the number of degree-of-freedom per beam element. The Eq.(B.6) implies that the function $u(x,t)$ can be approximated by a linear combination of u_j^e and ψ_j^e with $u_j^e(t)$ being the value of $u(x,t)$ at time t and node j of the element Ω^e at arbitrary fixed time $t > 0$. Substituting $w = \psi_i(x)$ and Eq.(B.6) into Eq.(B.3) and (B.4) leads to

$$\sum_{e=1}^{n}\left[\left(K_{ij}^e u_j^e + M_{ij}^e \frac{d^2 u_j^e}{dt^2}\right) - F_i^e\right] - \left[V_0 w_0 + V_L w_L + M_0\left(-\frac{\partial w_0}{\partial x}\right) + M_L\left(-\frac{\partial w_L}{\partial x}\right)\right] = 0, \tag{B.7}$$

where

$$\begin{aligned} K_{ij}^e &= EI\int_{x_e}^{x_{e+1}} \frac{d^2\psi_i^e}{dx^2}\frac{d^2\psi_j^e}{dx^2}dx, \\ M_{ij}^e &= \rho A\int_{x_e}^{x_{e+1}} \psi_i^e\psi_j^e dx, \\ F_i^e &= \int_{x_e}^{x_{e+1}} \psi_i^e f dx, \end{aligned} \tag{B.8}$$

with K_{ij}^e, M_{ij}^e, F_i^e being the element stiffness matrix, mass matrix, and force vector. After assembling process, the Eq.(B.7) can be written in the matrix form as

$$\mathbf{M}\ddot{\mathbf{U}} + \mathbf{K}\mathbf{U} = \mathbf{F}, \tag{B.9}$$

where $\mathbf{K}$ and $\mathbf{M}$ are the system stiffness and mass matrices, $\mathbf{U}$ denotes nodal displacements vector, and the *dot* symbol $(\cdot)$ represents the time derivatives. It should be noted that the boundary conditions in Eq.(B.7) contributes to the right hand side

of the system of ordinary differential equations in Eq.(B.9). To apply the boundary conditions, the weight (test) function w needs to vanish at the boundary points where the essential boundary conditions (deflection and slope) are specified; i.e., w is required to satisfy the homogeneous form of the specified essential boundary conditions of the beam problem.

Since the linear beam element is used in this dissertation, the Hermitian shape function $H_i(x)$ represents the weight function $\psi_i(x)$ so that the deflection and slope are continuous between two neighboring elements. The four components of the shape function of an element e is given by

$$\begin{aligned} H_1^e(\bar{x}) &= 1 - \frac{3\bar{x}^2}{L_e^2} + \frac{2\bar{x}^3}{L_e^3}, \\ H_2^e(\bar{x}) &= \bar{x} - \frac{2\bar{x}^2}{L_e} + \frac{\bar{x}^3}{L_e^2}, \\ H_3^e(\bar{x}) &= \frac{3\bar{x}^2}{L_e^2} - \frac{2\bar{x}^3}{L_e^3}, \\ H_4^e(\bar{x}) &= -\frac{\bar{x}^2}{L_e} + \frac{\bar{x}^3}{L_e^2}, \end{aligned} \tag{B.10}$$

where L_e is the length of a beam element, $\bar{x}$ denotes the spatial local coordinates such that $\bar{x}_1 = 0$ and $\bar{x}_2 = L_e$ defined as the local coordinates of nodes 1 and 2 of the beam element Ω_e. For the uniform discretization, the element stiffness matrix becomes

$$\mathbf{K}^e = \frac{EI}{L_e^3} \begin{bmatrix} 12 & 6L_e & -12 & 6L_e \\ 6L_e & 4L_e^2 & -6L_e & 2L_e^2 \\ -12 & -6L_e & 12 & -6L_e \\ 6L_e & 2L_e^2 & -6L_e & 4L_e^2 \end{bmatrix}. \tag{B.11}$$

The element mass matrix, which is required for dynamic analysis, is given by

$$\mathbf{M}^e = \frac{\rho A L_e}{420}\begin{bmatrix} 156 & 22L_e & 54 & -13L_e \\ 22L_e & 4L_e^2 & 13L_e & -3L_e^2 \\ 54 & 13L_e & 156 & -22L_e \\ -13L_e & -3L_e^2 & -22L_e & 4L_e^2 \end{bmatrix}. \tag{B.12}$$

Moreover, the element force vector implemented in this dissertation are the uniform pressure and concentrated force, which are given below.

$$\begin{aligned} \mathbf{F}^e_{\text{uniform}} &= \frac{q_0}{12}\begin{bmatrix} 6L_e & L_e^2 & 6L_e & -L_e^2 \end{bmatrix}^T, \\ \mathbf{F}^e_{\text{point}} &= P_0\begin{bmatrix} H_1(\bar{x}) & H_2(\bar{x}) & H_3(\bar{x}) & H_4(\bar{x}) \end{bmatrix}^T, \end{aligned} \tag{B.13}$$

where q_0 is the uniform pressure load within the element, P_0 is the concentrated force applied at the local coordinate $x = \bar{x}$, and the symbol T represents the transpose of the vector. Other types of applied force vector can be found from Kwon and Bang [57]. It should be noted that the element mass matrix in Eq.(B.12) is called the consistent mass matrix developed by Archer [4]. This matrix conserves the mass in terms of translational degree of freedom when, for example, the components in the matrix associated with nodal translational variables is added the total mass of the element equals to $\rho A L_e$. In dynamic analysis, however, the system mass matrix needs to be inverted, so the lumped (diagonal) mass matrix that the components of the matrix are all zero except the diagonal components may be used. The lumped mass matrix also conserves the mass for translational degree of freedom. Hinton et al. [40] (see also Kwon and Bang [57]) suggested the way to create the diagonal mass matrix from the consistent mass matrix. The procedure are summarized below:

- Add the diagonal components associated the translation degree of freedom where the sum is assigned as α_d.
- Divide all diagonal components by α_d and then multiply by the total mass element.
- Set all off-diagonal components to zeros.

Thus, the diagonal (lumped) element mass matrix obtained from the consistent mass matrix in Eq.(B.12) becomes

$$\mathbf{M}_L^e = \frac{\rho A L_e}{78} \begin{bmatrix} 39 & 0 & 0 & 0 \\ 0 & L_e^2 & 0 & 0 \\ 0 & 0 & 39 & 0 \\ 0 & 0 & 0 & L_e^2 \end{bmatrix}. \tag{B.14}$$